MEMS Devices for the Control of Trapped Atomic Particles

PhD Thesis

Paul Janin

Experimental Quantum Optics
Department of Physics
University of Strathclyde, Glasgow

March 8, 2022

This thesis is the result of the author's original research. It has been composed by the author and has not been previously submitted for examination which has led to the award of a degree.

Signed: Paul JANIN

Date: 15/12/2021

Abstract

This thesis presents the design and characterisation of novel MEMS scanners, for use in systems involving trapped atomic particles. The scanners are manufactured using multi-user silicon-on-insulator MEMS fabrication processes and use resonant piezoelectric actuation based on aluminium nitride thin films to produce one dimensional scanning at high frequencies, with resonance tuning capabilities of up to 5 kHz. Frequencies of ∼100kHz and higher are required to enable for example resonant addressing of trapped atomic particles.

This work demonstrates how the 200 µm and 400 µm diameter scanners can produce optical deflection angles upwards of 2° at frequencies from 80 kHz to 400 kHz. It proposes an addressing scheme based on Lissajous scanning to steer laser pulses onto 2D grids at a scale compatible with experiments involving single trapped atoms. It also examines frequency tuning capabilities of the scanners using localized on-chip Joule heating and active cooling ; frequency tuning and synchronization are shown to be critical to the implementation of 2-dimensional scanning with multiple scanners. These features are then demonstrated in a prototype implementation using fluorescing samples as a mock target to evaluate the optical performance of the scanning system. Finally, the thesis describes a proof-of-concept for integration of the scanners in a trapped atoms experiment, in which rubidium atoms trapped inside a magneto-optical trap are selectively pumped into a fluorescing state using a beam steered by the MEMS scanners.

Contents

Acknowledgements

This work was made possible by the support and involvement of many people beyond myself. I would like to thank, first and foremost, my supervisors : Ralf, who always made time to listen to my questions and give me the pushes I needed to move forward, with unfaltering consideration ; and Griff, whose insight and seemingly bottomless expertise helped me greatly in looking further ahead, be it at the beginning or the end of my PhD. I could not have asked for better guides through the sometimes foggy roads of research, and this acknowledgment seems way too modest compared to the trouble I caused them, and the faith they placed in me.

I would also like to thank the students and staff I had the chance to meet in the Experimental Quantum Optics Group and the Center for Microsystems and Photonics. They made sure that my time in Glasgow was a very pleasant one, and helped me at many junctures of my degree. I would like to thank in particular Alan Bregazzi and Sean Dyer, whose contributions were essential to the realisation of the atom trapping experiment discussed below ; Lucas Herdly from the Photophysics group, who offered me a precious opportunity to expand the horizons of this project ; and Peter Tinning, who kindly provided his aid in preparing optical test targets but also had to share a lab with me for the better part of two years. There are many more people at the University of Strathclyde who helped me in various ways, and unfortunately I do not have enough space here to thank them all.

There are also many others which I do not know personally, but whose past works form the scientific foundation of this thesis. I do not think that science is the fact of isolated individuals, and a look at the reference list at the end of this document will give a good idea of the number of researchers that inspired me throughout this project.

My gratitude also goes to my friends back home. Though it sometimes seemed like a rift separated us, they helped me find my lane through the jungle of tribulations that I sometimes stumbled on. Finally, I would like to thank my parents, who supported me when I first moved to Glasgow, and my family who never ceased to believe in me during these 4 years. Their affection was a most precious asset for my own motivation and day-to-day work.

My PhD was funded by an NPL scolarship, a grant that was made possible by the efforts of Professors Erling Riis and Deepak Uttamchandani. I am very grateful to them and to the National Physical Laboratory for granting me this opportunity to complete my education at Strathclyde.

Yesterday I was clever, so I wanted to change the world

today I am wise, so I am changing myself.

– Rumi

Chapter 0. Acknowledgements

Chapter 1

Introduction : of MEMS and small-scale atom traps

This work studies novel piezoelectric MEMS designs, their characteristics as optical control elements, and their potential for use in larger systems involving trapped ions and neutral atoms. Both MEMS and trapped atom physics are vast subjects, of which the present thesis covers a small fraction. This first chapter presents an overview of these research domains, through their historical development.

1.1 Brief history of MEMS technologies and optical MEMS

Microelectromechanical systems, or MEMS, is a term that encompasses devices smaller than a millimeter in total size, with parts typically in the sub-millimeter range. They are commonly integrated into larger systems as an interface between electronic signals and thermal or mechanical effects [1]. The reduced size of MEMS can be used in various fashions, and requires specific methods of fabrication and design, justifying their classification as a specific type of machine, and their study as a specific branch of both electronics and mechanical engineering [2].

The interest for devices miniaturized at micrometer and nanometer scale started long before the technology to do so existed. Richard Feynman, in his 1959 talk "There's plenty of room at the bottom" [3], envisioned technological developments that would

bring fabrication down to the atomic scale. The advances he described then, and in particular the idea of building machines that could operate with atomic precision, still motivate research today in the various branches of nanotechnologies [4] – with MEMS finding an equivalent at submicron scales in nanoelectromachanical systems (NEMS). MEMS are a result of the new techniques that enabled access to smaller spatial scales, developed through the second part of the 20th century.

Born from the evolution of integrated circuit technologies, MEMS aim to satisfy the need for more compact devices relying not only on electronics, but also on mechanically active parts enabling sensing and control through motion. Since they emerged from the advances that made integrated circuit manufacturing possible, it is only natural that their evolution followed that of silicon-based electronics. MEMS techniques based on other materials, such as polymers [5] and ceramics [6] were later developed.Successive developments in manufacturing technologies often brought improvements in precision and spatial complexity – finer parts with a greater aspect ratio – as well as layer complexity – giving access to a variety of electromechanical effects. Although the first micromachined devices were developed as early as the 1960s [7], the real beginnings of MEMS are usually placed in the 1980s, when the progress in integrated circuits made the fabrication of sub-millimeter scale sensors and actuators possible [8]. In the following years, the first demonstrations of anisotropic silicon etching [9, 10] opened new opportunities for more complex fabrication processes, by offering not only high precision in layer thickness, but also some selectivity in the regions to be etched ; this was months before the first microprocessor chips were commercially introduced by Intel [11].

The applications that followed in the next decades emerged similarly, notably the LIGA process for lithography [12] and deep reactive ion etching [13], from results of academic research being converted into commercial products and brought to industrial customers. Nowadays, MEMS are commonly being used in mobile phones, biomedical engineering, various sensing applications from pressure sensors to gyroscopes [14], aerospace [15] and robotics [16].

In recent years, MEMS fabrication processes have expanded beyond silicon-based technologies towards a wider range of materials, namely polymers, which offer many

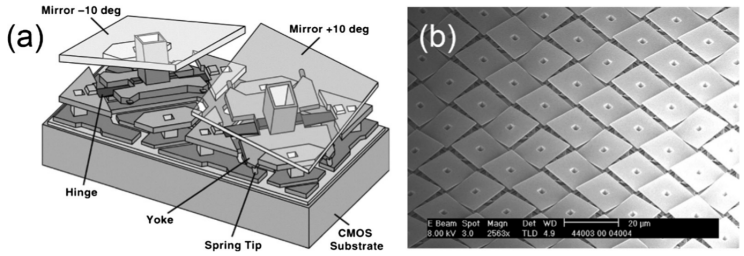

Figure 1.1: Left : Schematic layout of DMD mirrors. Right : SEM view of a DMD array. Reproduced with permission from [20] and [21]. Left is ©1998 IEEE.

cheap and flexible manufacturing options as well as unique chemical properties [17] ; and ceramics, for devices operating at high temperatures or making use of their specific mechanical properties such as piezoelectricity [6, 18, 19].

As the MEMS technologies and markets matured, they were used as optical devices, a field with strong interests in miniaturization. Optical MEMS were developed mainly after 1980 for a variety of applications, in particular for optical communications and with research efforts towards optical computing [22, 23]. The commercialization of the digital micromirror device (DMD) constituted a major advance in projection and display technologies [20, 24]. A DMD consists in a 2D array of micromirrors, which can be individually switched between two positions through electrostatic actuation (see Fig. 1.1). Using the device to project light towards or away from projection optics allows for the projection of a full image. This whole projection process is known as Digital Light Processing, a technology still used today in cinemas and commercial light projection equipment. The DMD was also used as a form of spatial light modulator (SLM) [25–28] ; the capability of tailoring illumination patterns led to DMD applications in structured illumination and super-resolution microscopy experiments [29–31]. One of the landmarks of optical MEMS for use in communications was the introduction of the optical network switch. Introduced in 2000, it included an array of MEMS mirrors designed to form an optical crossconnect between incoming and outgoing signals (see Fig. 1.2). The first demonstrated mirrors used electrostatic actuation with a 500 µm diameter and response times of a few milliseconds [32]. Several MEMS designs for MEMS optical switches were produced in the following years, as successful implementations of various

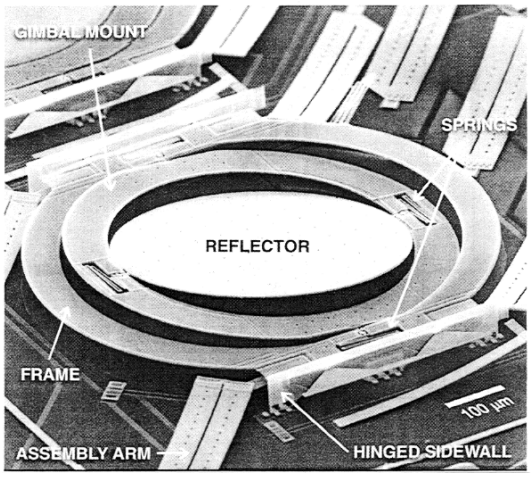

Figure 1.2: Micromirror used for optical crossconnects. Reproduced with authorization from [32]

microfabrication techniques [33].

The fast response time of those devices, along with the possibility to use mechanical resonance to achieve higher displacements, was a motivation for the development of scanning mirrors, for use in displays and imaging devices (Fig. 1.3). Unlike a DMD which only addresses light on a screen in an on-off fashion, a single scanning mirror can be used to scan a focused spot of light – usually a laser – along the projection surface to achieve higher resolution. Research in this type of mirrors for use in laser displays started before the 21^{st} century [34] and has made some advances towards catching up with commercial display technologies [35]. While it might seem surprising that research steps were taken towards single-mirror devices when long-standing applications such as the DMD achieved commercial fame by using arrays of thousands of MEMS, the appeal of single mirror structures comes from the potential for finer control and performance they present, with progresses in surface micromachining allowing for wider, smoother surfaces, and the high displacement given by resonant designs [36–40].

Like other types of microsystems, optical MEMS have also been used for biomedical applications, imaging and microscopy in particular. The ease of integration of MEMS in medical equipment makes them attractive for *in vivo* imaging and endoscopy [41, 42].

In general, the popularity and growth of MEMS can be explained by the particular advantages they offer over macroscale devices. Their small size makes them ideal for

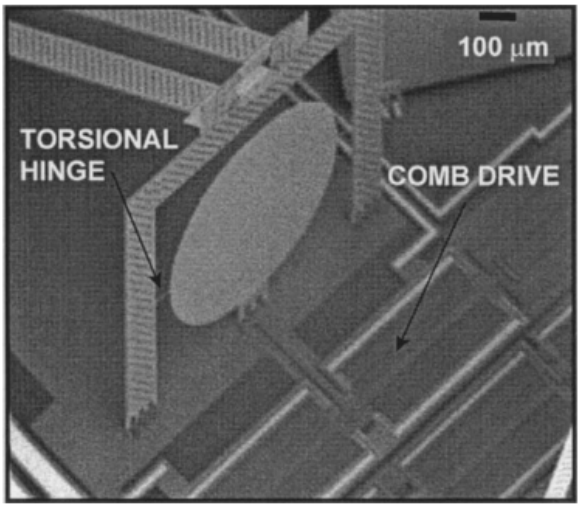

Figure 1.3: SEM picture of an early MEMS mirror. Adapted with permission from [36], ©1999 IEEE.

integration in mobile systems, such as aerospace applications. Batch fabrication techniques in an era dominated by silicon electronics allows for cheap and fast fabrication of high volumes, with a constant growth in market size and units sold overall. The ability to operate at smaller scales also entails lower power consumption and fast response times at broad frequency ranges, and birthed new applications that could not be implemented before the emergence of MEMS, such as microfluidics and energy harvesting [43–45].

1.2 Atom and ion traps : background for small-scale quantum optics

Controlled confinement of atomic particles has become a critical tool for atomic physics since the 1980s. While the initial motivation for the development of cooling and trapping techniques were spectroscopy applications, the emergence of single-particle quantum optics and quantum information processing participated in the advance of trapping experiments. The following briefly reviews the history of ion and atom trapping along with the current applications for individual particle traps.

Ion traps. Before the first experimental developments of quantum optics came with the invention of the laser in the 1960s, methods for trapping ions for use in mass spectrometry were already studied prior to 1955 [46]. The first demonstration of a quadrupole ion trap was realised by Paul and Steinwedel at the University of Bonn and patented in 1956 [47], leading to critical developments in the domain of mass spectrometry, and constitutes one of the first instances of using electromagnetic fields to trap individual atomic particles ; the quadrupole ion trap using a specific configuration of electrodes to generate a variable potential leading to stable trajectories for the ions placed inside.

In the decades that follow, the quadrupole ion trap was the source of new techniques for use in mass spectrometry, specifically regarding the selection and storage of ions [48–50]. The spatial organization of the electrodes, however, requiring four conducting elements to surround the trapped particles, constituted a challenge for its integration in other systems and proved impractical for individual manipulation of ions. This point led to new developments in the beginning of the 21st century, as ions were considered for use in novel quantum computing experiments as qubit candidates [51,52]. At the same time, efforts towards neutral atom trapping led to the first demonstrations of miniaturised surface traps for clouds of atoms [53,54], as an evolution of simple atom traps that were originally demonstrated in the 1980s [55]. The progress in microfabrication techniques originally used in silicon electronics opened new pathways for the realisation of small scale traps, including fabrication of monolithic three dimensional traps [56–58]. Further simplifications were also demonstrated, allowing all the electrodes to be placed on a single plane, suspending the ions above the surface of the trap [59, 60] (see Fig. 1.4). While it allowed for easier access to the trapped ions, it also greatly eased the fabrication process, and prompted demonstrations of more complex trap geometries for ion shuttling [61–63]. This development came with improvements in atomic state preparation, trap loading [64] and individual qubit control without the need for continuous laser cooling [65, 66].

Recent years have also seen demonstration of ion trap fabrication aiming at scalability, by using existing industrial processes [67], and integration with miniaturized optical

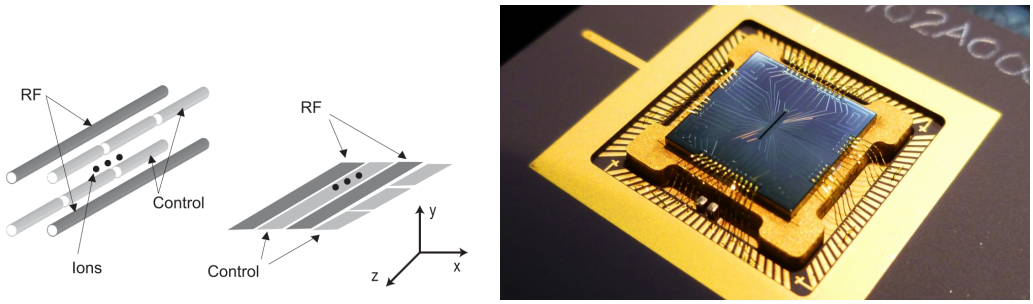

Figure 1.4: Left: schematic comparison of a linear RF ion trap and a surface ion trap. Reproduced from [59] with permission, ©2006 American Physical Society. Right: picture of a linear ion trap used in [65]. Reproduced with permission from the Joint Quantum Institute

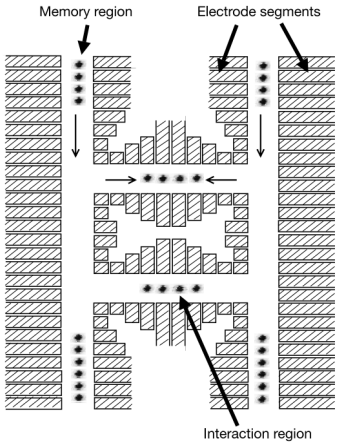

Figure 1.5: Schematic layout for a quantum charge-coupled device (QCCD) for storage and quantum operation on trapped ions. Reproduced from [52] with permission.

systems [68].

Current research endeavors involving ion trapping mainly revolve around quantum computing applications, either by developing transport and storing applications, such as the ones shown on Fig. 1.5 and 1.6, for use in a large-scale quantum computing system [69–72], or improving the reliability of quantum operations on trapped particles and coherence times [73, 74]. The promises of quantum computing already outlined at the beginning of the century [51, 52] still drive the research in particle trapping today, and were recognized in the 2012 Nobel Prize for Physics [75].

The technological developments in trap fabrication, optical control, and quantum-state engineering – in particular trapped particle entanglement [76] have allowed quan-

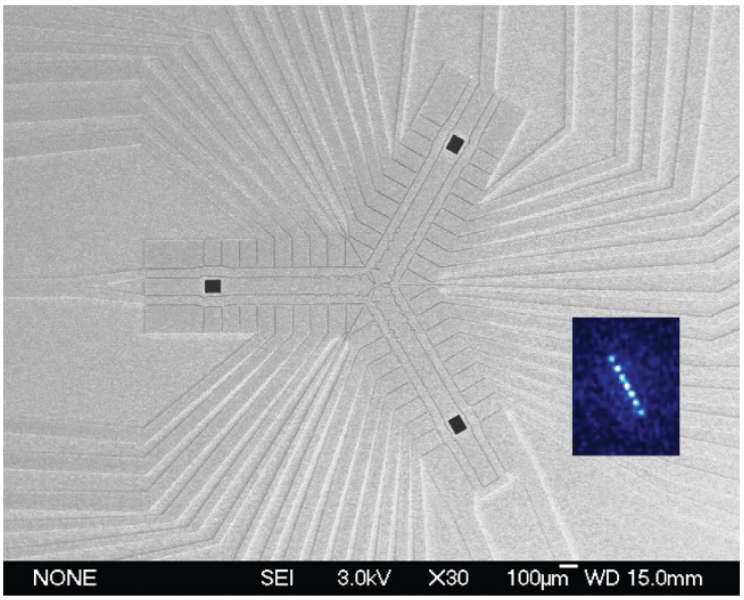

Figure 1.6: SEM image of a Y-junction ion trap for shuttling and storing. Inset shows a chain of ions above the trap electrodes. Reproduced from [61] with permission.

tum computing applications to evolve towards more complete systems and achieve demonstration of complex operations : programmable quantum gates to apply quantum algorithms [77, 78], global radiation logic for use in large-scale systems [79], qubit encoding through mechanical modes for error correction and detection [80]. A promising domain of application for current quantum computing systems is quantum physics simulations, using the behaviour of controlled qubits to model more advanced particle systems ; such simulations have also been demonstrated using trapped ions [81–84].

Ion trapping is currently understood to be a mature technology for integration in hybrid miniaturised systems and large-scale fabrication and deployment, for a variety of applications such as atomic clocks and magnetometry [85], and in parallel to recent advances towards integrated quantum technologies [86]. Thus, it is of no surprise that numerous experiments have been demonstrated using MEMS in conjunction with ion traps and other small-scale atom manipulation schemes. The use of optical MEMS in particular has proven useful to implement photonic control of atoms and ions [87], enabling beam steering for addressing individually trapped particles [88], or to assemble an optical cavity around the trap [89]. Of course, experiments involving optical

MEMS have also be used in quantum information processing (QIP) demonstrations, advancing the efforts towards the miniaturisation of complete quantum computing systems [73, 86, 90, 91]. Moreover, the previously mentioned developments in microfabrication techniques mean that MEMS and ion traps can be manufactured through similar processes [92], and those systems could be mass produced industrially at a reduced cost compared to large scale optical systems tailored for a specific trapping experiment. In the light of these recent works, progresses towards even more complex QIP systems on the one hand, and greater availability of small-scale trapping systems on the other hand, can be expected in the years to come, with such systems being released as commercial products.

Neutral atom trapping While ions are considered to be strong candidates for use as qubits [51, 93, 94], trapping technologies for individual neutral atoms have also received much interest for QIP applications, due to their long coherence lifetimes and the absence of Coulomb interactions between neighboring particles. Magneto-optical traps (MOTs) allow trapping of large number of atoms in a macroscale magnetic field, while the development of optical lattices in the 1990s [95] enabled addressing of individual atoms occupying trapping sites in a 2D or 3D electromagnetic potential. Magneto-optical traps use laser beams to create an electromagnetic trapping potential constraining atoms whose transition levels have been adequately shifted by an external magnetic field. Optical lattices implement a similar effect, with a lattice potential created by the interference of pairs of laser beams, producing trapping sites that can be occupied by single atoms. An illustration of this principle is shown in Fig. 1.7. This trapping method has been used to study various quantum phenomena [96, 97] and as a basis for atomic clocks [98, 99]. Compared to ion traps, which typically use positively charged atoms, MOTs and lattices allow trapping of a variety of Rydberg atoms for quantum gate and entanglement experiments [100, 101], although the use of neutral atoms in lattices for quantum information processing mainly gained interest in the last 15 years [102–104]. The fact that lattices with a large number of sites are relatively easy to engineer and load translate into a larger number of qubits compared to trapped ion systems. On the other hand,

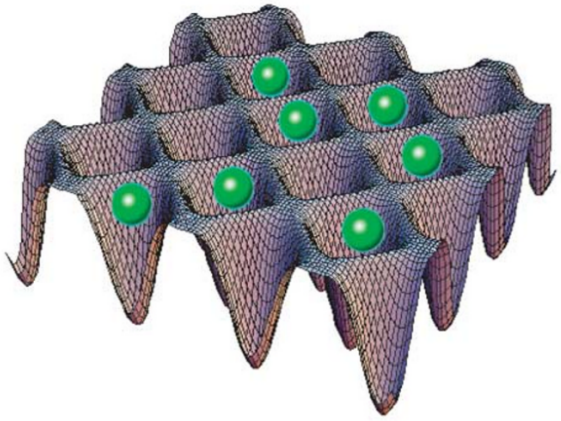

Figure 1.7: Schematic representation of an optical lattice trap. Reproduced from [98] with permission.

shuttling and addressing require careful implementation to ensure good coherence times and fidelity.

Similar to ion traps, there has been efforts to miniaturise neutral atom traps for integration, notably MOTs. The development of microfabricated reflective or diffractive surfaces allows the use of beam reflections to achieve 3D confinement with a single laser source, dramatically simplifying alignment and trap assembly, and reducing the overall spatial footprint of the traps [105–108]. Some current works also aim to fit bias field sources for MOTs in smaller packages, advancing the integration of full trapping systems as small size components. Miniaturisation and integration of *individual* neutral atom traps seems to have received less interest however. Optical lattices remain complex systems due to the high stability and extensive shielding required to control atomic transitions within the lattice, with methods for single-atom addressing adding further complexity. Even transportable trapping systems remain somewhat impractical for use beyond tailored experiments [109], and their scale currently remains in the metric range whereas other neutral atom applications have been successfully miniaturised [110], reflecting advances in atom cell [111,112] and vacuum chamber [113] fabrication. Beyond the problems of particle loading, cooling and trapping, imaging systems also require careful design to obtain compact, high-resolution measurement methods for atoms and ions.

1.3 General framework and research objectives

In light of what was presented above, opportunities for novel research and works can be outlined. The development of widespread quantum optics applications requires performance improvement of existing technologies, in reducing their overall scale, and increasing their portability, simplicity of fabrication, and ease of use. A critical threshold in such improvements is making their production possible using already existing, reliable industrial processes. Silicon-based manufacturing, notably, would greatly facilitate the integration of quantum optics in digital control systems.

While the particular technologies enabling atom trapping and quantum state manipulation are simple and well optimized in their principle of operation – magneto optical traps, ion traps, cooling techniques (see chapter 2) – the practical operation of a quantum optics experiment requires additional elements, some complex in their design and construction : control electronics, thermodynamic controllers, detectors, necessary electronics, beam shaping and steering optics ; these contribute to the footprint of a design, usually in a significant amount for custom research applications where space is often not a constraint. Therefore, it can be expected that significant improvements can be made in making those external elements more compact, as they are usually intended for simpler functions than the core elements of typical experiments. This follows a conventional "bottom-up" miniaturization approach: as individual components become smaller and more efficient, so do applications built from those elements.

Putting together efficient, scalable systems requires significant research and design work, and it was shown that such efforts have gathered notable interest in quantum optics and particularly quantum information processing [114–116]. The present work aims to demonstrate the design and operation of a proof-of-concept application, as a progression towards further possible improvements that may be revealed by the results obtained.

More precisely, this work focuses on the demonstration of optical MEMS devices used for quantum optics applications, with the initial intent of building a functional atomic particle trapping and addressing experiment. It describes the processes involved

in design, characterisation, and operation of the devices used and assesses the results obtained against other similar applications in terms of relevant factors already mentioned: overall scale, reliability, ease of fabrication and use, and operating performance. This research aims primarily at advancing the state of the art by proposing improved implementations of existing quantum optics experiments rather than developing original applications; and while the project is interdisciplinary in nature, the work presented here approaches the objectives from the MEMS design side. The MEMS devices were designed firsthand, assuming the existence or at least feasibility of an experiment for which they could be used, rather than designing devices for a specific application. This is in line with the progress of the author's work, the availability of resources, and the desire to explore a wide-range of applications. While this approach came with no guarantee of specific experimental applications for quantum optics, it pushed for the development of multi-purpose MEMS devices, with the intent of avoiding bespoke designs that would be constrained to a single application. The presented results should therefore be considered as a proof of concept for the integration of optical MEMS in a wide range of applications, rather than a progression towards a specific experiment.

This approach also presents some advantages over application-driven design, in a research context. Fast design ensuring early fabrication and characterization of the mirrors would ensure that performance of the devices as well as the fabrication process could be assessed, producing valuable data on the performance achievable with the type of design fabricated and revealing potential unforeseen constraints that might affect the range of functions available. While device performance can be modeled and simulated to some extent, practical experience is necessary to optimize it towards experimental implementation. Furthermore, a first iteration produced with looser constraints, as general estimates of performance requirements, ultimately offers more possibilities in terms of operation and thus, application, such that even without precisely knowing what results will be obtained experimentally, the possibility to build a suitable application demonstrating the performance of the design remains highly likely.

Another consequence of the chosen "MEMS first" approach is the way device performance was evaluated during characterisation. While the final objective is indeed to offer

optimised performance for a tested application, the latter was not available until late in the project. Therefore, device performance had to be measured temporarily either against devices used in similar applications, and in specific contexts – i.e. specific quantum optics experiments – or against MEMS devices with similar designs but different application purposes, e.g. display scanners. More details about design and performance characterisation are given in the following chapters, but it should be mentioned that the characterised MEMS devices were evaluated over three main metrics:

- displacement range; in the case of scanners, out-of-plane angular range;
- speed; for resonant devices, operating speed is tied to resonant frequency
- maximum optical power, that is the maximum optical radiation power the device can operate on without negatively affecting its overall performance. This was shown to be essential for enabling certain applications.

Chapter 2

Project-relevant atom trapping theory

The following chapter briefly describes parts of ion and atom trapping theory that are relevant to designing adequate control systems for trapped atom experiments. Since the subject of this thesis is not primarily concerned with developing trapping theory or techniques, this theoretical framework is only intended as context for the experimental results presented later. Therefore, this section does not aim to construct the full derivation of these theoretical results. This can be found in detail in the references provided here, many of which offer overviews of the topic extending significantly beyond the scope of the present work. From a MEMS standpoint, the characteristics of interest are particle separation for individually trapped atoms or cloud size and temperature for atoms in magneto-optical trap, as well as optical power and speed requirements in typical experiment timescales.

The objective of using MEMS for quantum optics is to develop more compact and power-efficient systems for integration into optical applications. MEMS devices can replace optical components that are commonly used in experimental environments but impractical for streamlined designs, such as acousto-optic modulators. We identified three quantum applications where this paradigm could be used in an effective manner : individually trapped ions, cold atoms in magneto-optical traps, and two- or three-dimensional grids of single trapped atoms formed by optical lattices. The sections

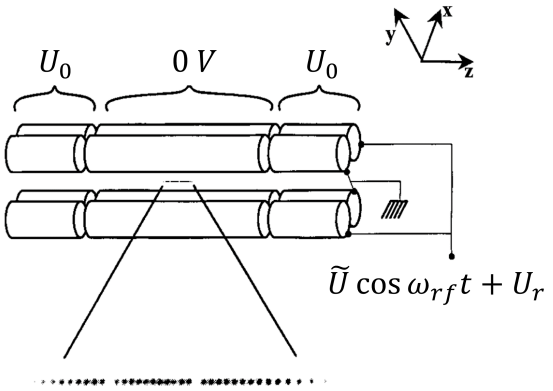

Figure 2.1: Illustration of an early realisation of a linear Paul trap with the corresponding electrode voltages, with an image of a string of ions trapped in the resulting potential. Quantum computing operations would require a beam steering system for individual addressing of the ions. Adapted from [117].

of this chapter focus on the defining theoretical elements of these atom trapping and cooling techniques.

Generally speaking, atomic particle trapping techniques aim to construct potentials coupled with the internal state or the motion of the atoms to suppress or constrain their displacement to a small volume, in high-vacuum conditions where collisions between particles are unlikely and the atoms can be easily cooled. The following considers atoms as individual, localized particles in a perfect vacuum.

2.1 Ion traps

As mentioned in section 1.2, ion traps offer a relatively easy method to trap single charged particles within a quadrupole electromagnetic potential formed by well-arranged conducting elements generating voltages varying at RF frequencies. Fig. 2.1 shows an illustration of a linear ion trap.

Following the approach shown in [118] and [119], the resulting trapping potential is usually given under the form

$$\Phi(x,y,z,t) = \frac{U}{2}(\alpha x^2 + \beta y^2 + \gamma z^2) + \frac{\tilde{U}}{2}\cos(\omega_{\mathrm{rf}} t) \times (\alpha' x^2 + \beta' y^2 + \gamma' z^2) \qquad (2.1)$$

where U is the DC electrode voltage, $\tilde{U}$ the RF electrode voltage, ω_{rf} the RF frequency and $\alpha, \beta, \gamma, \alpha', \beta', \gamma'$ the axial coefficients. The RF potential is necessary to ensure confinement of the ions while satisfying the Laplace equation $\Delta\Phi = 0$. This condition imposes $\alpha + \beta + \gamma = 0$ and $\alpha' + \beta' + \gamma' = 0$. A linear Paul trap satisfies this condition with $-(\alpha + \beta) = \gamma > 0$ and $\alpha' = -\beta'$, $\gamma' = 0$, leading to static confinement in the z (axial) direction and oscillating confinement in the x-y plane for positively charged particles – as most ion traps use single positively charged ions. In the case of a single, classical trapped particle, the equations of motion can then be obtained independently for x and y :

$$\ddot{x} = -\frac{Z|e|}{m}\frac{\partial\Phi}{\partial x} = -\frac{Z|e|}{m}\left(U\alpha + \tilde{U}\cos(\omega_{\mathrm{rf}}t)\alpha'\right)x \tag{2.2}$$

for a particle of mass m and charge $Z|e|$. This equation can be rewritten in a form known as the Mathieu equation :

$$\frac{d^2x}{d\xi^2} + [a_x - 2q_x\cos(2\xi)]x = 0 \tag{2.3}$$

with

$$\xi = \frac{\omega_{\mathrm{rf}}t}{2}, \quad a_x = \frac{4Z|e|U\alpha}{m\omega_{\mathrm{rf}}^2}, \quad q_x = \frac{2Z|e|\tilde{U}\alpha'}{m\omega_{\mathrm{rf}}^2} \tag{2.4}$$

from the analytic solutions of this equation, an approximate expression for $x(t)$ can be found as

$$x(t) \propto 2\cos\left(\sqrt{a_x^2 + q_x^2/2}\frac{\omega_{\mathrm{rf}}}{2}t\right)\left[1 - \frac{q_x}{2}\cos(\omega_{rf}t)\right] \tag{2.5}$$

along the x axis, this corresponds to large harmonic oscillations at frequency $\omega_{\mathrm{r}} = \sqrt{a_x^2 + q_x^2/2}\frac{\omega_{\mathrm{rf}}}{2} \ll \omega_{\mathrm{rf}}$, the *secular motion*, superimposed with driven oscillations at frequency ω_{rf}, the *micromotion*. If the fast, low-amplitude oscillations of the micromotion are neglected, the trapped particle behaves as if confined by the harmonic pseudopotential in the x-y plane. For example, in a linear trap where $a_x = a_y$ and $q_x = -q_y$:

$$\tilde{\Phi} = \frac{m}{2Z|e|}\omega_{\mathrm{rf}}^2(x^2 + y^2) \tag{2.6}$$

So far, only single ions where considered. In practice, trapping multiple ions is of much more interest for quantum optics, as the ion states can be entangled and use

for multi-qubit quantum gate operations. When multiple ions are loaded into the trap, they will be confined along the z axis provided that the radial confinement is sufficiently stronger than the axial confinement i.e. $\omega_{\mathrm{r}} > \omega_z = \sqrt{U\gamma Z|e|/m}$ (writing the axial harmonic potential as $\Phi(z) = \frac{m}{2Z|e|}\omega_z^2 z^2$) [117]. This condition becomes stricter as the number of ions within the trap increases, and thus the repulsive force on each particle grows larger ; when the number of trapped ions become too large, the ions at the edge of the ion crystal will break into a zigzag formation.

An approximate expression for the separation between adjacent ions is given by $s = ((Z|e|)^2/4\pi\epsilon_0 m\omega_z^2)^{1/3}$ [119, 120], typically in the order of a few µm. For example, if we consider Ca^+ ions trapped with a radial confinement $\omega_z = 2$ MHz, we get $s = 9.5$ µm, similar to values reported in [62]. However, ions trapped in strings by such potentials will not be spaced evenly, the ones near the center of the trap being closer together than the ones at the edges. Exact spacing values can be numerically estimated by calculating the wavefunction for the quantum system formed by the trapped ions, or by simulating the ions as classical charged particles. Consequently, the trap parameters can be used to obtain a scale for the trapped ion spacing, which can be useful for planning experiments requiring individual addressing.

2.2 State manipulation through interactions with radiation fields

When considering atomic state transitions driven by external electromagnetic radiation, e.g. addressing laser beams, the quantum treatment of the interaction is based on the Hamiltonian describing the coupling of the transition dipole operator with the field [117]:

$$H = -\mu_d \cdot \mathbf{E}(z,t) \tag{2.7}$$

where μ_d is the electric dipole moment for the transition and E the applied electric field. Expanding this Hamiltonian using the spin-1/2 framework, and solving Schrödinger's equation for the state defined by the ion's motional and internal eigenstates, reveals that coupling with the radiation field induces Rabi oscillations in the ion's state. More

precisely, if we consider a transition between the states $|+, n'\rangle$ and $|-, n\rangle$ where $|+\rangle$ and $|-\rangle$ denote the internal states of the ion and $|n\rangle$ the motional states[1], the wavefunction Ψ for perfectly resonant radiation in the basis formed by these states will follow

$$\Psi(t) = \begin{bmatrix} \cos\Omega_{n',n}t & -ie^{i(\phi+\frac{\pi}{2}|n'-n|)}\sin\Omega_{n',n}t \\ -ie^{-i(\phi+\frac{\pi}{2}|n'-n|)}\sin\Omega_{n',n}t & \cos\Omega_{n',n}t \end{bmatrix} \Psi(0) \tag{2.8}$$

where ϕ is the initial phase of the atomic state and $\Omega_{n',n}$ the Rabi frequency for the transition. The Rabi frequency of the oscillations results from the properties of the field and the trapped atom. For a wave field propagating in the z direction, in the *Lamb-Dicke regime* where the ion's motion amplitude is much smaller than the wavelength, $\Omega_{n',n'}$ finds an approximate expression :

$$\Omega_{n',n} = \Omega_{n,n'} = \Omega\eta^{|n'-n|}\sqrt{\frac{n_>!}{n_<!}}(|n'-n|!)^{-1} \tag{2.9}$$

where $n_>$ (respectively $n_<$) is the greatest (smallest) of n and n'. For the first sideband transitions to and from the ground state, where n and n' are zero or one, this simplifies further to $\Omega_{n',n} = \eta\Omega$. Here $\Omega = -\mu_d E/\hbar$ and $\eta = kz_0 = k\sqrt{\frac{\hbar}{2m\omega_z}}$. The value η is the Lamb-Dicke parameter, depending on the wavenumber k and the amplitude of the ion's wavefunction in the motional ground state z_0. The conditions of the Lamb-Dicke regime imply $\eta \ll 1$.

The Rabi frequency is central to the state manipulation of ions and single trapped atoms in general, as it governs the evolution of the atomic state when an external radiation field is applied. Therefore, arbitrary state rotations on the trapped particles can be achieved with pulses whose durations are suitable fractions of the Rabi period. For example, in the two-state basis described above and within the spin-1/2 model, flipping the state of the ion can be achieved by a pulse of duration $\tau = \pi/2\Omega_{n,n'}$, a so-called π-pulse (as it corresponds to a rotation of angle π in the Bloch sphere).

As can be seen from Eq. 2.9, the exact value of the Rabi frequency and thus ion

[1]For simplicity, this section omits the description of the quantum eigenstates of the ion and the derivation of the corresponding transitions. In general, the internal and motional states of trapped ions are entangled, in a way that forms the basis of trapped ion quantum computing. More details can be found in [117] and [118].

switching times depend on the trapping frequency and the amplitude of the applied wave field, in addition to the atomic species and state transition being used. While these parameters can be accurately predicted, it may be more practical to measure the frequency of a given transition experimentally and adjust the duration of state-switching pulses accordingly. Although the duration of π-pulses varies from experiment to experiment, measurements found in the literature give Rabi frequencies in the 10 to 100 kHz range for trapped ions, corresponding to pulse durations in the order of 10 µs [65, 91, 118, 121–123].

2.3 Magneto-optical traps for trapping and cooling of neutral atoms

Magneto-optical traps (MOTs) are a relatively simple way to generate a trapping potential for neutral atoms. MOTs can be considered an evolution of optical molasses where pairs of counter-propagating laser beams slow down groups of atoms by applying radiation force on Doppler-shifted transitions of the moving atoms. An MOT turns the optical molasses into an effective potential trap by the addition of a magnetic quadrupole gradient, resolving the hyperfine Zeeman structure of the atomic structure through the Zeeman effect. The description that follows is based on [124] unless specified otherwise.

An atom placed inside a pair of counterpropagating beams will experience scattering forces affecting its movement, with a scattering rate depending on the frequency of the light relative to a given transition of the atom. If the beams are suitably red-detuned from the transition, the scattering force will apply more strongly to the Doppler-shifted atoms moving against the propagation direction of the beam, effectively resulting in a damping force in that direction. The damping force has the form

$$F_m = -\alpha v, \quad \alpha = -4\hbar k^2 \frac{I}{I_{\text{sat}}} \frac{2\delta/\Gamma}{[1 + (2\delta/\Gamma)^2]^2} \tag{2.10}$$

where v is the atom velocity along the beam axis, k the beam wavenumber, δ the beam detuning, Γ the transition linewidth, and I_{sat} the saturation intensity specific to the transition. Typical optical molasses use three pairs of counter-propagating beams

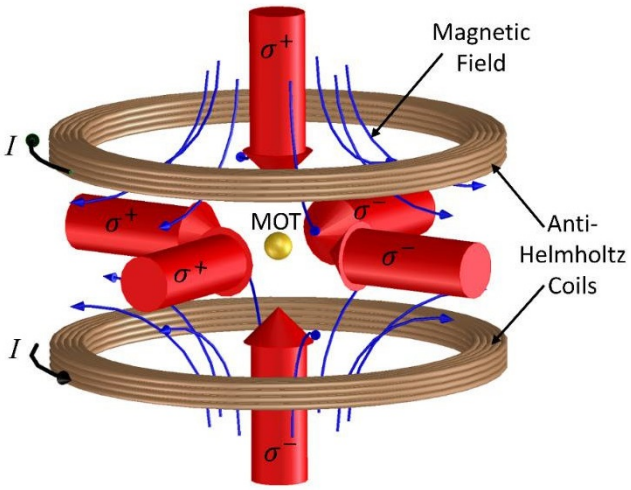

Figure 2.2: Schematic representation of a magneto-optical trap with three pairs of counter-propagating beams. The red arrows indicate the direction of the beams with the matching polarisation. Reproduced from [125] under creative commons license CC BY 3.0.

to obtain damping in three dimensions, allowing for efficient cooling of the atoms in the region where the beams intersect (see Fig. 2.2). However, the cooling beams do not need to be orthogonal, and it is enough that the sum of the wavevectors weighted by beam intensities are zero, since the damping force is proportional to beam intensity [107, 124], i.e.

$$\sum_i I_i \mathbf{k_i} = \mathbf{0} \tag{2.11}$$

Experimental realisation in magneto-optical traps was simplified by the use of reflective surfaces [105, 106] or diffraction gratings [108, 126] to produce confinement in all three directions using a single laser beam. This greatly facilitates integration of trapping systems with microfabricated optics and mobile experiments.

Optical molasses offer a convenient method for cooling atoms by absorbing their spatial momentum, but do not produce actual trapping ; atoms may drift away from the center of the molasses and eventually escape the slowing radiation. MOTs generate such trapping force by the addition of a spatially dependent magnetic field. The field is generated using a pair of coils, producing a quadrupole field between the coils that can be approximated to a linear gradient near its center. Consequently, atoms moving away

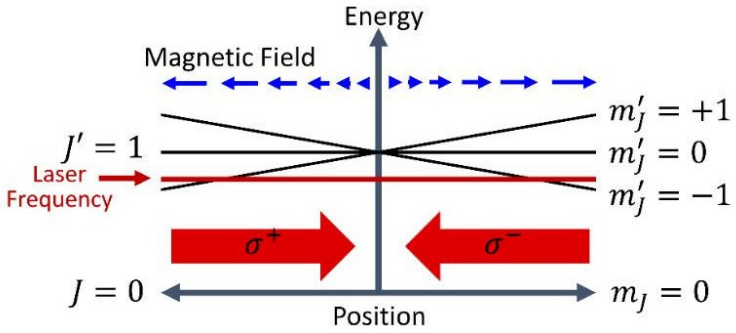

Figure 2.3: Illustration of the energy levels and the effect of the polarized trapping beams near the center of the MOT for a transition with $J = 0 \rightarrow J' = 1$. Reproduced from [125] under creative commons license CC BY 3.0.

from the center of the field will experience a shift in their fine structure levels – the $|Jm_J\rangle$ states. Consider again the case of three pairs of beam parallel to the field axes. If the light from each beam is circularly polarized, so that it drives transitions with $\Delta J = \pm 1$ and $\Delta m_J = \pm 1$ based on state selection rules and depending on the position relative to the center of the trap, the shift will induce resonance with the beam whose scattering force pushes towards the center of the trap. This scattering force increases with the Zeeman shift as the distance from the center of the field increases. This effect is illustrated on Fig. 2.3. By choosing the correct beam handedness, it is therefore possible to obtain a trapping force in addition to the molasses damping, giving the total force applied to the trapped atoms :

$$F_{\text{MOT}} = -\alpha v - \frac{\alpha\beta}{k} z, \quad \beta = \frac{g\mu_B}{\hbar}\frac{dB}{dz} \tag{2.12}$$

for a displacement in the z direction. The value g is the difference in hyperfine Landé g-factors g_F for the transition and μ_B is the Bohr magneton. For MOTs using gratings or reflective surface to produce a pyramidal trapping potential, a similar effect is observed through the decomposition of the polarization of reflected beams along the magnetic field axes. More details about the theory of such traps can be found in the references given above.

MOTs can commonly trap atom numbers in the order of $10^5 - 10^9$, with the volume and density of the trapped atom cloud depending on beam size and intensity as well as

the strength of the field gradient. Typical embodiments of this concept use beams with diameter of approximately 1 cm, with intensities of the order of the saturation intensity, i.e. a few mW/cm^2. The gradient magnetic fields are of the order of 10 G/cm. The resulting atom clouds have a Gaussian density profile with a characteristic size of $\sim$1 mm, centered on the beam overlap volume. While an ideal trap could confine atoms indefinitely, trap loading and experiment times are usually in the 10-100 ms range, as longer timescales make heating effects and atom loss more prominent. Again, many of these parameters depend on the experimental configuration and other constraints, such as vacuum chamber geometry, the atom species and type of atom source, and the available laser wavelengths. Chapter 6 describes in more detail the operation of an MOT and the implementation of a MEMS scanning system for atom addressing within an atom cloud.

2.4 Optical lattices for trapped atoms

The standing wave formed by counterpropagating beams of light can be used to form trapping potentials for individual neutral atoms, based on the electric dipole force applied to an atom in an electric field gradient. Again following [124], the force applied to an atom by a single electromagnetic wave propagating in the z direction is

$$F_{\text{dipole}} = -\frac{\hbar\delta}{2}\frac{\Omega}{\delta^2 + \Omega^2/2 + \Gamma^2/4}\frac{\partial\Omega}{\partial z} \tag{2.13}$$

for light detuned by δ from a transition with linewidth Γ and Rabi frequency $\Omega = eX_{12}E_0/\hbar$ where X_{12} is the atomic dipole matrix element corresponding to the transition. By comparison, the previously mentioned scattering force is proportional to $1/\delta^2$, and for large values of detuning δ, i.e. $\delta \gg \Gamma, \Omega$, we can approximate the dipole force as

$$F_{\text{dipole}} \approx -\frac{\partial}{\partial z}\Big(\frac{\hbar\Omega^2}{4\delta}\Big) \tag{2.14}$$

showing the dependence of the force on the electric field intensity gradient.

In a standing electromagnetic wave, the intensity varies quickly between the nodes

and antinodes of the wave with a period of $\lambda/2$. Again for large detunings, the dipole force leads to a trapping potential of the form

$$U_{\text{dipole}} = U_0 \cos^2(kz) \tag{2.15}$$

with U_0 being the dipole potential at the antinodes of the wave. The dipole force will lead to atom trapping for red-detuned beams ; three-dimensional arrays of potential wells can be created by using perpendicular pairs of beams, with a spacing of $\lambda/2$ between wells. For near-infrared beams, this corresponds to a three-dimensional trapping site density in the order of 10^{13} cm^{-3} ; when compared to common trapped atom cloud densities of 10^{10} cm^{-3}, it is not surprising that such lattices will have at most one atom per potential well.

The optical intensity required to achieve potential wells deep enough to trap cooled atoms is around 10-100 kW/cm^2 [98,102,103,124], a value that is reasonable for focused beams with waists of the order of 50 µm (which would require around 3 W of total power). The main difficulties in creating large lattices lie in ensuring uniform intensity profiles to obtain consistent trap depth, and bringing atoms into the lattice while keeping their energy low enough that they cannot escape the trap once loaded. Previously mentioned experiments report lattice atom numbers of 10^2-10^3, and [127] demonstrated trapping and individual addressing of up to 48 cesium atoms in a 3D optical lattice. This last experiment used an optical lattice with a spacing of 5 µm using pairs of beams at 845 nm propagating at a relative angle of 10°, to obtain a separation between atoms large enough for practical addressing.

2.5 Summary

This chapter offered a brief overview of the theoretical bases for atomic particle trapping experiments, and of the formalism describing the phenomena leading to trapping. It also gives expressions for trapping parameters related to the power and timescales required to achieve practical embodiments of such experiments. The exact value of these parameters may however vary significantly depending on the specific methods and objectives of the

experiment, such that it is difficult to evaluate them ahead of time. Indeed, many experimental references given here report optimization of these parameters through direct measurements after the experiment is built. Nevertheless, the calculations shown above provide useful insight on the scale of practical incarnations in terms of size and power, which in turn may be used to anticipate the requirements of an application ahead of time, especially regarding optical design. They will provide a useful context for the MEMS characterisation results that follow.

Chapter 3

MEMS scanning mirrors for high-frequency applications

3.1 Design perspective for MEMS scanning mirrors

Scanning micromirrors make up a wide group of devices designed towards the same application: reflecting a beam of light in a desired direction, steering it in a continuous manner. The motion of the mirror is obtained through linear or angular displacement produced by actuators, whose size, time response, and mode of operation can vary depending on the system requirements. The actuation of the mirror can be done quasistatically, or through mechanical resonance, where the device geometry is used to amplify the actuator displacement; in the latter case, resonance frequencies and overall dimensions of the devices are also characteristics to consider. MEMS scanners are typically distinguished by their actuation method and fabrication technologies [35].

From a practical standpoint, the principle of operation of a scanning mirror remains the same: making a reflective surface rotate along one or two of its axes in order to change the deflection angle of an incoming beam. This is achieved by generating a mechanical force applying torque to the mirror plate, either directly, or through mechanical coupling with a larger structure. The placement of the actuators relative to the mirror can vary depending on the chosen geometry; the actuators and mirror are suspended by a hinge and/or a frame to allow freedom of movement. An example of a

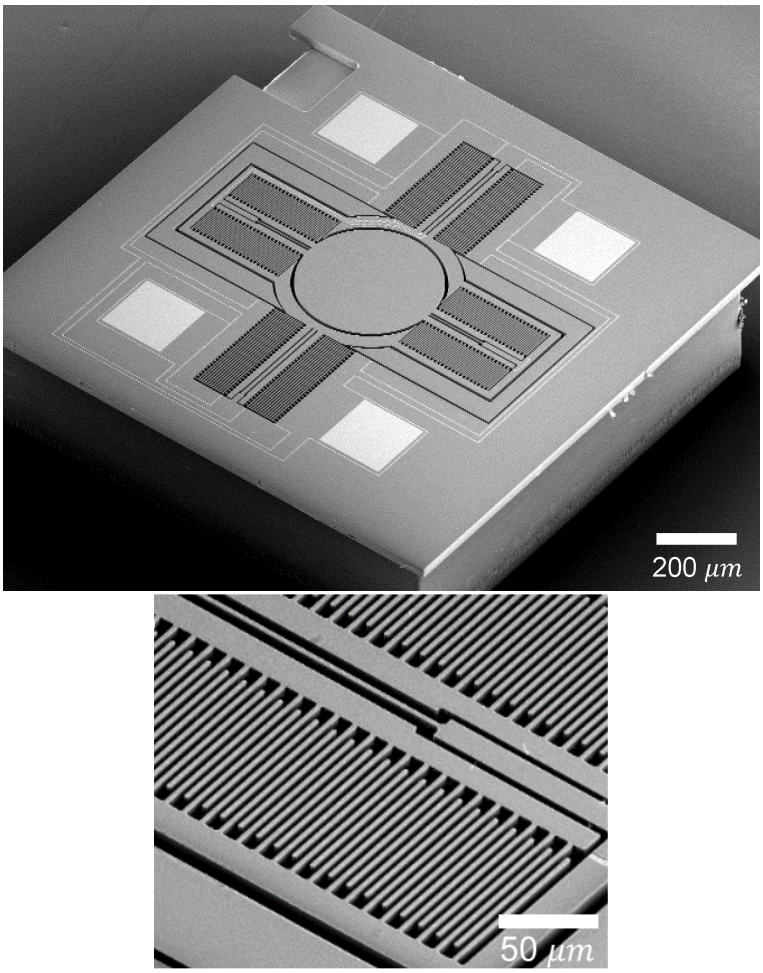

Figure 3.1: SEM image of a scanning MEMS mirror for Lissajous scanning and close up view of the electrostatic comb-drive actuators. Reproduced with permission from [128]

MEMS scanner is shown on Fig. 3.1.

Actuation methods used for scanners are the same as those for any kind of MEMS devices: electrostatic, electrothermal, piezoelectric, or electromagnetic actuation [35]. Each of these actuation methods offers its own advantages and disadvantages, along with specific design and fabrication requirements. These are described in the following.

Electrostatic actuation Electrostatic actuation remains the most widespread actuation method due to its ease of integration and fabrication, using materials compatible with common silicon fabrication methods [130]. Electrostatic actuation is based on the forces existing between electrically charged surfaces, with the force being dependent

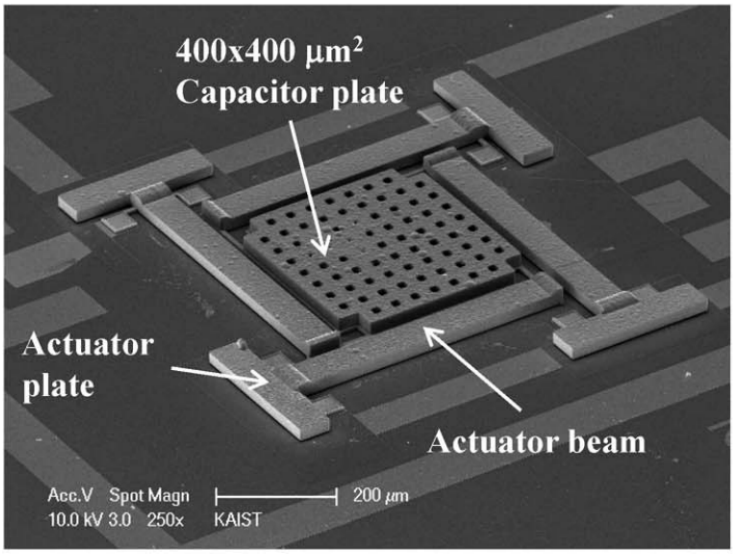

Figure 3.2: A variable capacitor using electrostatic parallel plate actuators. Reproduced from [129] with permission.

on the overlap area of the surfaces, their difference in electric potential, and the distance between them. Actuators then involve separate elements close together with high surface and low separation distance, typically with a stationary part (stator) whose voltage can be controlled externally and a moving part (rotor) whose movement depends on the voltage applied to the stator. Common actuator geometries involve parallel plates [130, 131] or comb-drive actuators [132, 133]; Fig 3.2 show an example of electrostatic MEMS actuators. While power consumption of electrostatic actuators remains low (typically 1 μW or less [134]), they require high voltages, in the order of 100 V, to produce large stroke amplitudes when compared to other actuation methods.

Electrothermal actuation Electrothermal actuation uses thermal effects to change the shape of deformable elements through heating. It typically makes use of unimorph or bimorph configurations, in which two or three layers, respectively, of different materials are stacked. The layer structure is heated through Joule dissipation by running a current through the conducting layer(s) and expands as its temperature rises. The difference in thermal expansion coefficient leads to bending in specific directions, and the structure will gain curvature, creating displacement at the end of a cantilever for example [135,

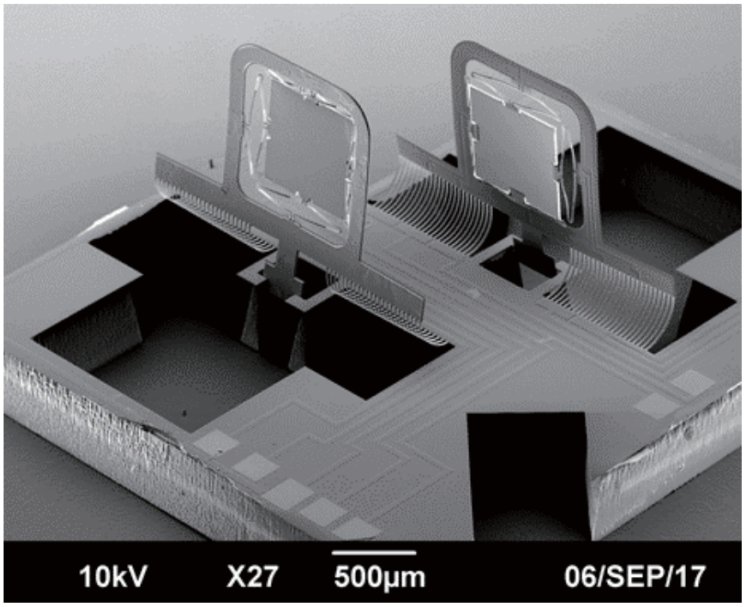

Figure 3.3: An example of thermally actuated scanners. Reproduced from [137] with permission.

136]. Thermal actuation requires specific geometries to leverage the thermal expansion displacement, and designs must take in account the properties of the materials used in the structure, although Joule heating can be exploited in many commonly available semiconductor materials.

Unlike electrostatic and piezoelectric actuation, which do not rely on current intensity, Joule heating rests on running current directly through the actuator. While the small size of the device keeps energy consumption low compared to macroscale devices, in the order of 10 mW [138–140], heat dissipation and thermal capacity scaling make electrothermal actuation less efficient for larger MEMS and lead to continuous power consumption. Furthermore, electrothermal actuators typically have relatively long response times – in the order of 1 ms or longer – making them unsuitable for fast operation of scanners. Thermal MEMS mirrors that have been demonstrated [139, 141, 142] usually operate either in static, non-resonant deformation, or for slow axis actuation of systems with multiple axes and actuation types [140, 143]. For these reasons, thermal scanning mirrors remain rare, for examples see [137] and [144] (Fig. 3.3).

Piezoelectric actuation Piezoelectric actuation has been successfully used for high frequency transducers [145, 146] and oscillators, with quartz oscillators widely used for time measurement in everyday devices. It has only recently gained interest in research and design of scanning mirrors, due to the fabrication difficulties it presents [147]. The actuators make use of the deformation induced by voltage differences applied to piezoelectric materials, typically lead-zirconate-titanate (PZT) compounds [147–149], aluminium nitride (AlN) [150, 151] and zinc oxide (ZnO) [39, 152–154]. While harder to deposit, PZT is a popular choice because of the large forces it provides. Unlike electrothermal actuation, the low displacements produced by the actuators must be leveraged through specific mode shapes or mechanical coupling between actuators and the mirror plate. The development of multiuser piezoelectric deposition processes by industrial manufacturers such as MEMSCAP has made the fabrication of piezoelectric MEMS relatively inexpensive.

Piezoelectric effects offer shorter response times (i.e. a faster response) than electrothermal actuators for material deformation, at the cost of much smaller displacements in static operation: while piezoelectric materials develop high forces, their deformation is limited to very short strokes, typically a few nanometers. While this makes them less suited to slow axis mirrors requiring static tilts, this drawback is acceptable for resonant designs where displacement comes from kinetic energy stored in the mechanical structure; it is enough that the forces generated from the piezoactuators feed the resonance so that high displacements and scanning angles can be reached. Mechanical coupling also can be leveraged to increase scan angles for specific geometries: resonance in large elements can couple with smaller elements, and a small displacement in the former will induce a proportionally larger displacement in the latter. Commonly used geometries for scanning mirrors involve a large frame being directly actuated, coupled with a small frame for specific mode shapes, for example in [147, 155, 156]. This type of structure offers mechanical amplification for the short motions of the piezoactuators, while offering more surface for actuator deposition and in turn generating more force. The mechanical properties of piezoactuators are examined in more details in section 3.2.

Since piezoelectricity involves mostly static charge effects, power consumption in

piezoactuators is negligible as electrical currents through the actuator are theoretically nonexistent. Voltages involved through actuation are also typically lower than electrothermal and electrostatic actuation, usually going up to 50 V where electrostatic actuators can require voltages of 100 V or more. Additionally, piezoactuators offer the advantage of monolithic structures where comb-finger actuators are subject to pull-in effects and more sensitive to structure deformation. Thus piezoelectric actuation is well-suited to high frequency scanners with lower displacement requirements, with compact designs and low energy consumption. However, one drawback of piezoactuators is their innate hysteresis properties leading to nonlinear responses in some conditions [157, 158].

Electromagnetic actuation Electromagnetic actuation generates movement from the Lorentz forces created by surrounding magnetic fields on a conducting element supplied with a current. Electromagnetic actuators usually rely on permanent magnets for field generation and coils to generate long current elements as the produced force scales with the overall conductor length; either the magnet or the coil can be placed on the moving part, be it the mirror itself or a coupled mechanical structure. Depositing a layer of magnetic material on the mirror allows for actuation without electrical contacts, the current being supplied to an external coil, while forming a coil element on the moving part requires current to be fed to the MEMS for actuation, eliminating the need for a large coil surrounding it (see Fig 3.4). In the latter case, permanent magnets are usually placed on each side in plane with the moving part, as the Lorentz force is produced orthogonally to the magnetic field-current plane [155, 159]. In both cases, actuation intensity and frequency is controlled through the current supplied to the coil.

As the forces produced scale linearly with coil length and magnetic field strength, electromagnetic actuation is better suited for larger devices with long elements. The linear dependence of the Lorentz force on both magnetic field intensity and supplied current allows for easy actuation and control of movement amplitude. Mechanical coupling can also be used to increase available surface and total force. No matter the design, the need for external elements makes electromagnetic actuators more voluminous, and harder to integrate with other devices than electrostatic or piezoelectric MEMS. Fur-

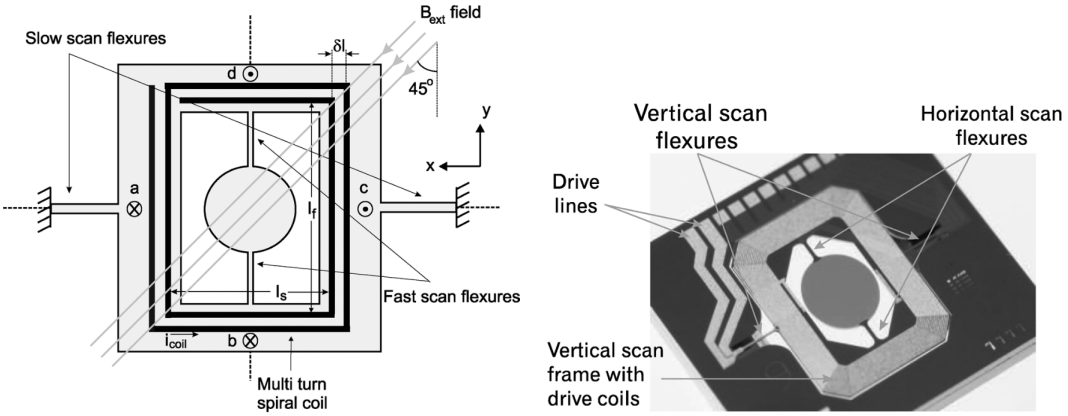

Figure 3.4: Schematic and photograph of a 2-axis electromagnetic MEMS scanner. Reproduced from [155] with permission.

Table 3.1: Qualitative comparison of different actuation types.

Actuation type	Electrostatic	Electrothermal	Piezoelectric	Electromagnetic
Response time	Fast	Slow	Fast	Fast
Power consumption	Moderate	High	Low	High
Maximum voltage	10-100 V	10V	10-100V	$<$ 10 V
Produced displacement	Moderate	Large	Very low	Large

thermore, high currents are required to obtain large strokes, leading to heat dissipation effects and increased power consumption; strong magnetic fields require proportionally larger magnets in volume. Table 3.1 summarizes the characteristic of the different actuation methods mentioned in this section.

Scanner geometry Beyond actuation methods, other factors must be considered in the design of scanning mirrors. Operation frequency was already mentioned; device geometry may vary depending on the speed requirements of the scanner. Another major element to consider is size: for resonant scanners, resonance frequency will scale proportionally to the inverse of the characteristic length of the device, and lead to a trade-off between mirror size – which can affect the numerical aperture of an optical system – and operation frequency, which determines the speed at which reflected light can be scanned across the mirror's range. These two values are essential in display applications [38, 160]. Different layer thicknesses and the resulting change in mass may also affect resonance frequencies. Furthermore, mirror size and structure thickness

will affect the force required to actuate the device and the corresponding movement amplitude. While larger geometries usually mean more space available for actuators, this also leads to increased power consumption and larger footprint for integration.

Movement amplitude, which for scanners is the angular range of motion and optical scanning, is heavily affected by actuation type and size. Electromagnetic actuators typically produce the highest displacements due to their overall large size and force available, while the properties of piezoelectric actuators heavily limit their displacement range and quickly lead to saturation effects as actuation voltages increase (see Table 3.1). Stress distribution and material stiffness will vary greatly with geometry as well. While small-scale silicon devices built with thin (∼10 µm) layers are resilient to high stresses and allow for large dynamic deformation, suspension beams and frames with large cross-section will remain stiff and push resonance frequencies higher, with lower deformation range. Fluid damping and ambient pressure will also greatly affect mechanical performance and frequency response in particular. Vacuum packed MEMS are free from air damping and will reach higher frequencies and displacements with the same geometry.

These desired MEMS characteristics – size, actuation methods, frequency requirements, power consumption – are dictated by the application for which the device is designed, as well as the available materials and fabrication processes.

3.2 Piezoelectric actuation background

The MEMS designed, tested and integrated in the following use piezoelectric actuation as their main method of operation. This section describes in more quantitative details the characteristics of piezoelectric actuators and the specifics of their implementation. In particular, the properties of thin-film aluminium nitride (AlN) actuators will be reviewed.

Piezoelectric actuation process Piezoelectric actuators make use of the inverse piezoelectric effect, through which an applied electric field produces strain in the piezoelectric crystal; this is opposite to the *direct* piezoelectric effect, by which mechanical

stress produces charge displacements inside the crystal which can be read out electrically. The inverse piezoelectric effect is expressed with the piezoelectric coefficients of the material d_{ijk} :

$$x_{jk} = d_{ijk} E_i \tag{3.1}$$

where x_{jk} is the induced strain and E_i a component of the electric field, $i, j, k \in \{1, 2, 3\}$ being the corresponding axis indices. Piezoelectric coefficients are commonly indexed with the last two coordinates replaced by the Voigt tensor indices $d_{ijk} = d_{ip}$, reflecting the symmetry of the piezoelectric stress/strain tensors. When taking into account mechanical stress within the material, we obtain the constitutive linear equation of piezoelectricity [161] :

$$x_p = s^E_{pk} T_k + d_{kp} E_k \tag{3.2}$$

where $\mathbf{s}^E$ is the material's elastic compliance at constant electric field, and $\mathbf{T}$ is the mechanical stress tensor. For non-piezoelectric materials ($d_{kp} = 0$), this is the generalized Hooke's law.

Another useful value is the piezoelectric stress coefficient $e_{iq} = c^E_{pq} d_{ip}$, with c^E_{pq} being the linear elasticity coefficient, as it gives a direct relation to the equivalent stress produced by the piezoelectric effect.

It must be noted that the electromechanical coupling constituted by the piezoelectric effect leads to a dependence of the material electrical permittivity and mechanical compliance on both mechanical and electrical boundary conditions, and these thus vary depending on the configuration studied. This dependence for a specific geometry is represented by the mechanical coupling factor k, which is the square root of the ratio between stored energy and converted input energy [161] :

$$k^2_{ij} = \frac{d^2_{ij}}{\epsilon_0 \epsilon_i s^E_{ij}} \tag{3.3}$$

which expresses the relationship between piezoelectric coefficients, the electrical permittivity ϵ_i which intervenes in the direct piezoelectric effect, and mechanical compliance. ϵ_0 is the vacuum permittivity. Again, the relevant coefficients for this general

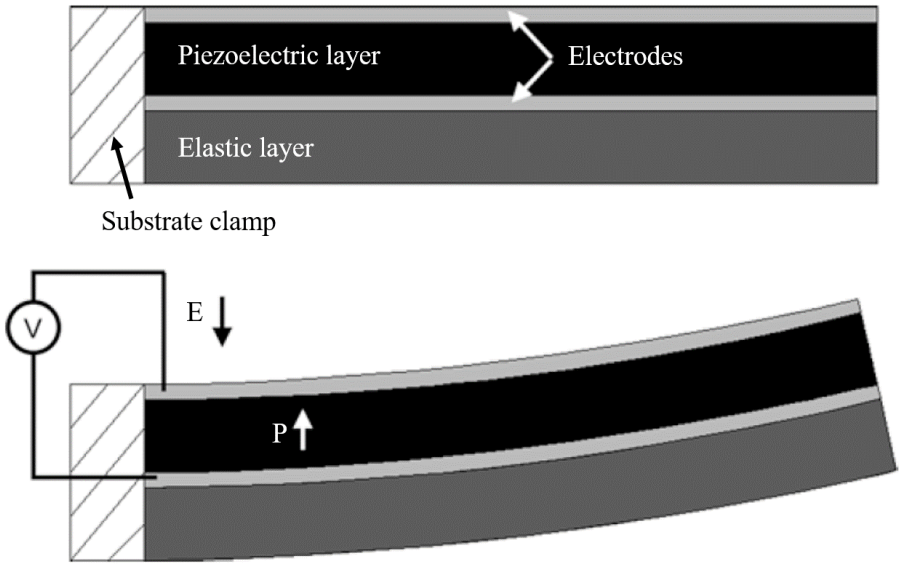

Figure 3.5: Illustration of the inverse piezoelectric effect in a unimorph cantilever geometry. The applied electric field E induces a change in polarization P in the piezoelectric layer, leading to in-plane stress, and out-of-plane deformation for the clamped cantilever. Reproduced from [161] with permission.

equation vary depending on the geometry and boundary conditions.

Principles of piezoactuator design Common actuator geometries involve unimorph structures, where a thin-film piezoelectric material is deposited on another elastic layer, and bimorph structures, with the piezoelectric material on both sides of the elastic layer, with electrodes placed between the layers and on the opposite faces of the piezoelectric layers. This electrode configuration generally aims to use in-plane strain, based on the d_{31} coefficient, which can generate out-of-plane displacement in the structure, for example in a unimorph cantilever (Fig. 3.5). Furthermore, the elastic layer will affect the elasticity and strain of the piezoelectric material. It is then useful to define effective thin-film piezoelectric coefficients, taking in account the clamping to the supporting layer, as well as the material symmetry of the thin-film. For the direct piezoelectric effect, where the applied field is fixed to zero, we have [162] :

$$e_{31,\text{eff}} = e_{31} - \frac{c_{31}^E e_{33}}{c_{33}^E} = \frac{d_{31}}{s_{11}^E + s_{12}^E} \tag{3.4}$$

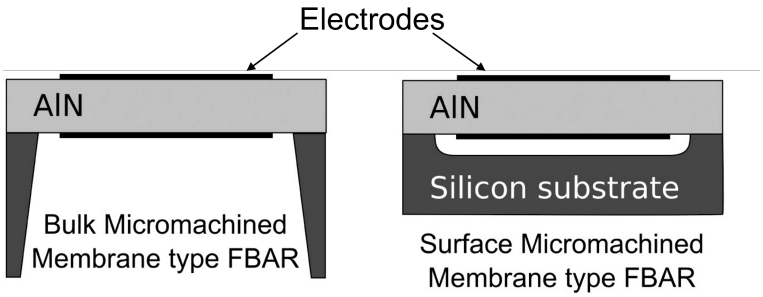

Figure 3.6: Schematic representation of film bulk acoustic resonator (FBAR) structures. Reproduced from [170] with permission. The device can either be used as an active resonator, with voltage applied to the electrodes generating RF acoustic waves in the piezoelectric membrane ; or as a sensor, where waves in the membrane or in fluids in contact with the membrane are converted to electrode voltage.

whereas for the inverse effect, where an applied electric field perpendicular to the film plane produces a measured strain, [163] gives :

$$d_{31,\text{eff}} = d_{33} - 2d_{31}\frac{s_{13}^E}{s_{11}^E + s_{12}^E} \tag{3.5}$$

Therefore, experimental measurements of piezoelectric actuator performance will often relate to these effective structural coefficients rather than the actual piezoelectric coefficients intrinsic to the piezoelectric material.

Piezoelectric resonators The low displacement (a few microns for the largest PZT actuators [164]) and fast response time – in the nanosecond range, since the stress is applied instantly once the polarization in the material is established – characteristic of piezoelectric materials makes them ideal for use as acoustic resonators at RF frequencies [165–167]. The configuration known as film bulk acoustic resonator (FBAR) [168–170] (Fig. 3.6) has been successfully used in many applications for RF electronics including switching and filtering; the high sensitivity offered by direct piezoelectricity also motivated the production of resonating sensors, i.e. high frequency energy harvesters [171].

As actuators for large displacements of resonant structures at lower frequencies – in the 1 to 100 kHz range, typical of MEMS scanners – piezoelectric thin films are somewhat less prevalent due to competition with other previously mentioned actuation

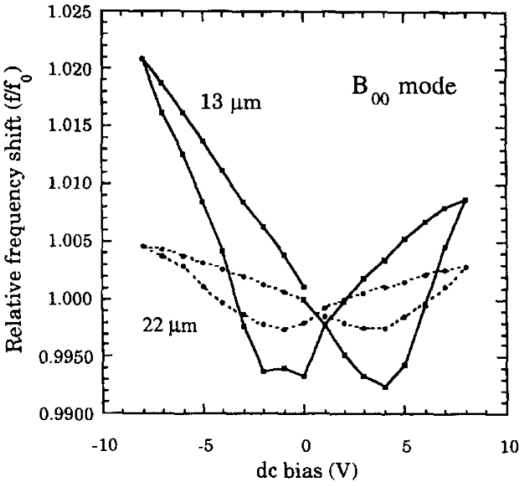

Figure 3.7: Resonant frequency shift of a PZT thin-film diaphragm as a function of applied DC bias, with different film thicknesses. Reproduced from [168] with permission.

technologies. However, resonant piezoelectric actuators exhibit fast response times, low power consumption, and relatively large force when compared to other actuation types which make them attractive for certain scanning applications.

A notable property specific to ferroelectric thin films, which include PZT, but not AlN and ZnO, is their nonlinear behavior in presence of an external electric field bias; this effect becomes significant in thin-films where moderate voltages can translate into large electric fields. For piezoelectric MEMS resonators, this effect may result in a frequency hysteresis as a voltage bias is applied to the film (see Fig. 3.7).

Aluminium nitride properties The following briefly describes aluminium nitride as a piezoelectric material, since it is used for the actuators used for this thesis. AlN crystals were already studied early in the 20th century [172], and research at the time denoted its particular physical properties, in particular its hardness, high thermal conductivity, resistance to chemical etching, and piezoelectric properties. Table 3.2 shows a summary of the corresponding physical values.

This table shows how AlN has typically lower piezoelectric coefficients than PZT compounds ($d_{31} \approx -15$ pm/V [178], $d_{33} \approx 20$ pm/V [163]), leading to lower displacements as mentioned in section 3.1. Mechanical coupling was already mentioned as

Table 3.2: Physical properties of AlN.

Thermal conductivity (W/cmK) [173]	3.19 at 300 K 1.00 at 600 K 0.49 at 1000 K
Bulk indentation hardness (GPa) [174]	17.7 at 300 K
Piezoelectric coefficients (pm/V) [175–177]	$d_{33} = 4.17 - 7.07$ $d_{31} = 1.9 - 3.53$

a method to produce large displacements for resonant structures; similarly, custom structures have been demonstrated to amplify static displacement with piezoactuators, reaching stroke lengths of several hundred micrometers for an actuator deformation of a few nanometers [164].

AlN thin films are usually deposited using reactive sputtering. Crystal growth quality is an important factor both for piezoelectric performance and layer patterning: a poor layer texture will result in larger lateral etch rates when submitted to wet etching [179]. Higher etching precision can be achieved with chemical plasma etching, allowing the formation of smooth, high resolution structures [180]. An advantage of aluminium nitride is that it can be readily deposited on silicon, along with a variety of metallic layers with good epitaxial compatibility, easily forming parallel electrode configurations. Aluminium, platinum and titanium layers feature hexagonal symmetry similar to AlN and are therefore good candidates for metallic layers [181]. Conversely, PZT films usually require a buffer layer for proper deposition onto silicon [182, 183].

3.3 Design and characterisation of tilting MEMS scanners

For an experiment looking at atomic particle addressing, scanning mirrors naturally appear as fitting devices for beam steering, for reasons previously explained. The devices described in the following were made with this application in mind. They were made with the intent of proposing novel designs as well as improving on the performance of earlier applications, such as [90]. However, these devices were fabricated as prototypes, for initial characterisation and proof-of-concept demonstrators, so that the experience

gained could serve the design of further iterations as well as other devices using the same fabrication method.

3.3.1 Mirror geometry and design

To produce out-of-plane tilting displacements, a scanning mirror geometry requires a moving plate (the mirror) and some hinge structure suspending the plate, connecting it to the die and allowing it to rotate around an in-plane axis. Several configurations are possible to achieve this type of geometry, with many variations for hinge shape, size, and actuator placement. Since scanners are a widespread type of optical MEMS, many geometries have been studied and can be found in the literature (see section 3.1). For piezoelectric actuation, actuator surface and shape are especially important, since they define how and how much force can be transferred to the mechanical structure. Piezoactuators are usually suspended to allow for the supporting surface to bend and are directly connected or placed close to the mirror hinge to convert actuator deformation into torque or flexural force applied on the hinge, which in turn drives the rotation of the mirror plate.

The devices fabricated in this research are inspired from other geometries found in the literature. The scale of the devices, however, was reduced so that the mirrors are at most 400 µm in diameter; this reduction in scale pushes the resonance frequencies higher – proportionally to the inverse square root of the scanner's mass –, following the requirement of fast operation. The objective was to reach tilting frequencies above 100 kHz in order to easily match the time scale of quantum rotation pulses (see chapter 2.1), while typical scanners operate at less than 50 kHz. Higher frequencies may also be obtained by reducing the thickness of the scanner, and consequently the mass of the resonant structure; the effect of layer thickness is discussed in section 3.4. However, the MEMS fabrication process used imposed a fixed thickness for the suspended scanners. The scanning micromirrors were designed for manufacturing using the MEMSCAP PiezoMUMPS (Piezoelectric Multi User MEMS Process), an industrial fabrication process using aluminium nitride (AlN) to form thin piezoelectric films. The base for fabrication is a 10 µm thick silicon-on-insulator (SOI) layer, formed on a 400

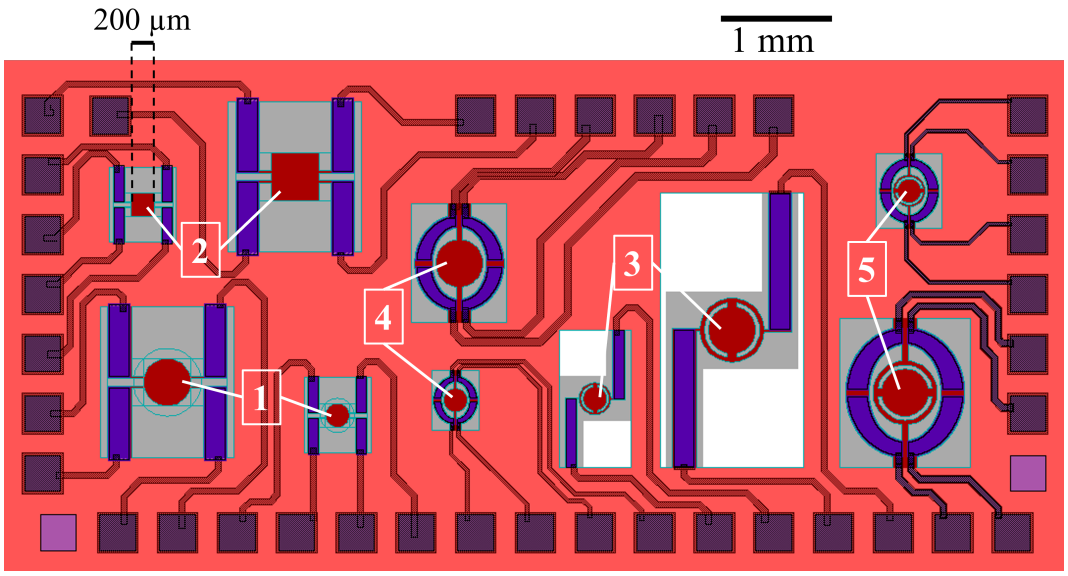

Figure 3.8: Layout of the complete fabricated half die.

µm thick substrate wafer. This silicon layer is n-doped and can be used as a common ground electrode for the actuators. The substrate can be etched from the back to form suspended structures and through holes. Piezoelectric actuators are formed by a 500 nm film of AlN on top of which a 1 µm layer of aluminium is deposited (see below). The aluminium layer serves as the top electrode of the actuator, allowing driving of the piezoelectric film. A silicon oxide (SiO_2) layer is used to insulate the aluminium layer from silicon where there is no piezo material layer in the design.

Here, the hinges, actuators, and mirror plate of each design are fully suspended. The total die area available for fabrication – half a full die, 9×4.45 mm – was much larger than a single MEMS, so 10 devices in total could be fabricated per die. The devices are scaled versions of five different geometries, each built for 200 µm and 400 µm mirror plates. The geometries are shown on Fig. 3.8 and described as follows :

1. a suspended circular mirror with two hinges, connected on each side to actuator arms attaching the hinges to the substrate. Four actuators in total can be independently controlled;

2. the same geometry, but with a square mirror plate. This design was chosen to evaluate the influence of mirror plate shape on residual stress and surface

curvature;

3. a circular mirror with a single hinge, connected on each side to two long actuators arms attached to the substrate. This device was used to examine the influence of actuator size on frequency and displacement, and to study the possibility of static actuation;

4. a circular mirror with a single hinge connected on each side to a suspended elliptical gimbal, on which four actuators are fixed, one per quadrant relative to the hinge. The gimbal is attached to the substrate by a wide hinge allowing space for electrical connection to the actuators. This design, making use of mechanical coupling between the mirror plate and the gimbal, is a scaled down version of the geometry in [147];

5. the same design, but with a circular frame fixed around the mirror plate and connecting it to the main hinge. This additional structure is meant to reduce mirror deformation by spreading mechanical stress around the perimeter of the mirror.

Of the designs mentioned above, only the results obtained with the last one are presented here, as it exhibited the most adequate behavior for our requirements. That device is shown in detail on Fig. 3.9.

3.3.2 Device simulation

In order to estimate scanner properties and validate device design before fabrication, the selected geometries were simulated using the finite-element simulation software COMSOL 5.2. While the software allows for complex simulations involving several physical effects, a simple model of the mechanical structure was sufficient for our purposes. In particular, piezoelectric effects, thermal effects, and fluid damping were neglected. The simulated structure includes the full suspended structure, comprised of the back-etched single-crystal silicon layer, the thin-film aluminium nitride layer, and the aluminium electrode layer. Regarding mechanical properties, silicon and aluminium nitride were simulated as anisotropic materials and the simulated structure was rotated to match

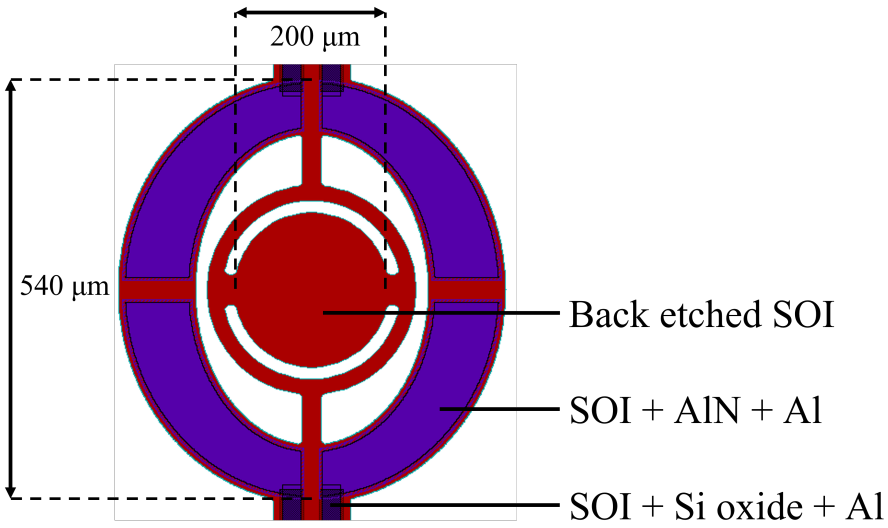

Figure 3.9: Schematic layout of a gimbal resonant scanner with a 200 µm mirror plate diameter. The 400 µm diameter mirror has the same layout, scaled by a factor of 2.

the crystalline orientation of the wafer during manufacturing. Some of the properties of aluminium nitride were mentioned above; the elastic coefficients of wurtzite AlN crystals can be found in [184]. The validity of the assumption that an AlN thin-film has the same mechanical properties as a bulk crystal was not investigated, but its impact is expected to be low considering that it constitutes only a small fraction ($< 5\%$ in thickness) of the mechanical structure. The elastic coefficients of monocrystalline silicon, a well-studied material, were taken from [185].

The software computes the mechanical resonance frequencies and corresponding mode shapes, based on stress distribution, material properties, and mechanical constraints. Following the finite element method, the geometry is broken down in a mesh of elements of variable size with fixed bounds, a smaller maximal size leading to a finer approximation of the real geometry. For this simulation, computer memory limitations imposed a maximal size of at least 8 µm to keep computation times within reasonable values; this was found to have a minor impact on the precision of results, as the corresponding variation in eigenfrequencies was less than 1% even for a maximal size of more than 20 µm. Examples of the simulated modes are shown on figure 3.10, and the list of all the simulated modes can be found in appendix A.

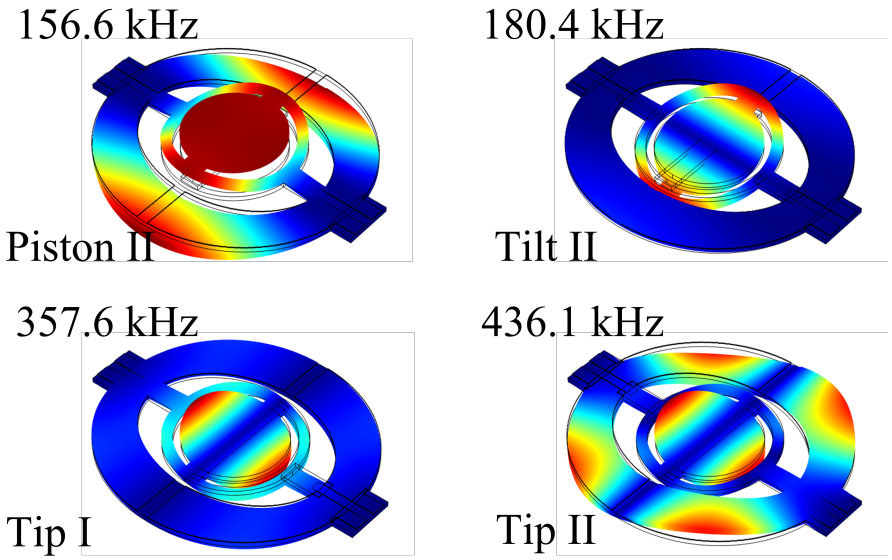

Figure 3.10: Selected simulated eigenmodes for the 200 µm diameter scanning mirror, with corresponding eigenfrequencies.Left to right, top to bottom: second piston mode; second tilting mode; first tipping mode; second tipping mode. Structure deformation is exaggerated by about 10x for clarity. Warmer colours indicate greater deformation.

It is also important to keep in mind certain points when interpreting simulation results :

- since actuation is not taken into account, simulations do not give information on the achievable amplitude for a given mode. While the relative displacement between two points is relevant for a given mode shape, it should be regarded only as qualitative information;
- neglecting fluid damping effects from ambient pressure operation leads to overestimation of the resonance frequencies. The actual resonance frequencies when operating at ambient pressure were found to be approximately 10% lower than simulated frequencies (see below);
- simulations do not take into account fabrication tolerances and imperfections. Additional deviation in resonance frequencies and residual stresses should be expected on the fabricated design. This is important when considering the optical properties of the mirror, as surface curvature and roughness may vary from one

device to another. For the purpose of the simulation, the scanners were assumed to be flat with no pre-existing stresses in the structure.

Consequently, the results of the simulations confirm that high frequency operation of the scanners is indeed possible, by using either of three out of plane rotational modes: the second tilting mode, where the axis of plate rotation is parallel to the mirror hinges, which are deformed in a torsional motion, and the first two tipping mode where the axis of rotation is perpendicular to the hinges, which are deformed in a flexural motion. The terms 'tipping' and 'tilting' are used to designate those motion shapes in the following. Higher frequency harmonics of the tipping and tilting modes can also be used, although frequency requirements should not require to go beyond the first harmonic of either mode. Mode harmonics will also provide reduced energy coupling from the driving signal, and consequently much lower scanning amplitude.

3.3.3 Device fabrication process

The mirror was fabricated externally using the PiezoMUMPS process. The process is detailed step-by-step in [186] and can be summarized as follows :

- the 10 µm top silicon layer of an SOI wafer is N-doped with phosphorus;
- a 1 µm layer of thermal oxide is grown and etched to form an insulation layer from the metal contacts;
- the 500 nm piezoelectric film of AlN is deposited and etched;
- a metal layer of 20 nm of chrome and 1000 nm of aluminium is deposited and etched to form electrical pads and contacts;
- the top layer of silicon and oxide is patterned to complete the formation of device structures, before back etching;
- the front face of the die is covered with a protective layer, and the handle wafer is etched from the back using deep reactive ion etching (DRIE), stopping at the doped silicon layer, to form suspended structures. the protective layer is then released to expose the finished devices.

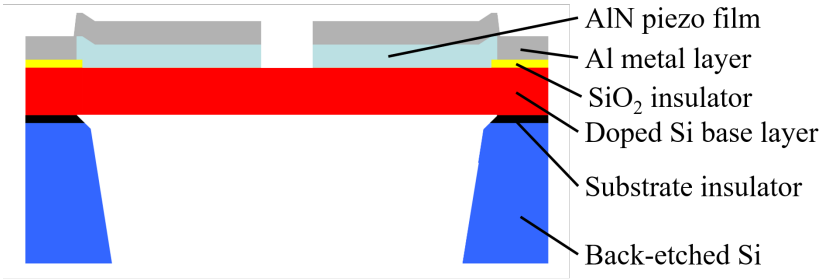

Figure 3.11: Side view of the MEMS layer structure. Not to scale.

Fig. 3.11 shows the completed layer structure. This process is well suited for fabricating moving parts with high deformation and movement amplitude, using piezoelectric or electrostatic actuation. The device geometry is however limited to essentially monolithic, low aspect ratio structures. This is not a problem for fabricating MEMS mirrors which mostly require flat, wide structures. Mirrors can only be fabricated this way in the plane of the die; normal or quasi-normal reflections off the mirror surface then requiring the incident beam to be perpendicular to the chip's plane.

Due to the PiezoMUMPS being a commercial multiuser process, the delay between design submission and receipt of manufactured chips is approximately 6 months, stressing the importance of careful planning of the design ahead of submission. The dies were received fully released and ready to be bonded to a carrier board.

Over 30 devices in total were fabricated in two runs, as the first produced batch of 17 chips was received with some dies severely damaged. The damage consisted mostly in missing or misshaped piezo and metal layers, and etching damage to the mirror plates. Example of post-manufacturing damage on the chips received can be shown on Fig. 3.12.

3.3.4 Mirror characterisation

The dies with no apparent defects were first characterised at rest using white-light interferometry, to the measure mirror plate curvatures. The results are summarized in Fig. 3.13.

While results vary for each design variation, the average mirror plate curvature was

Figure 3.12: Left: damaged scanner with the top metallic layer partially missing. Right: surface damage on a scanner plate.

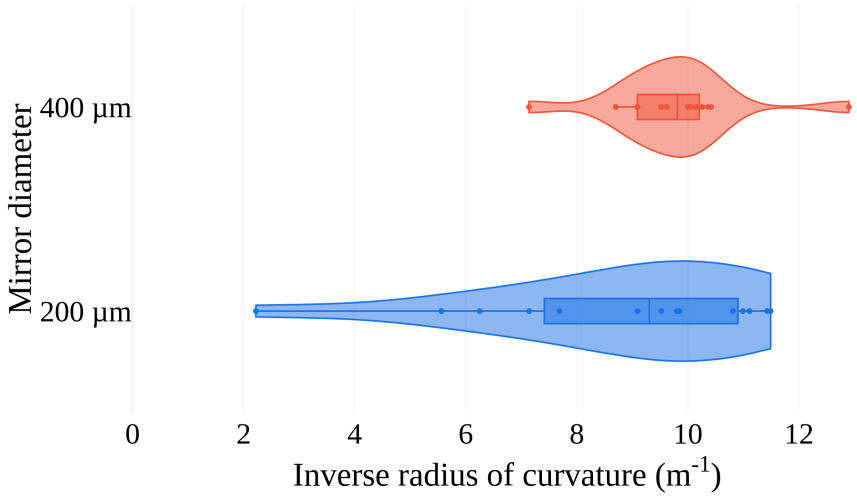

Figure 3.13: Violin plot of the average curvature of the mirror plates over the 15 fabricated chips, for the 400 µm and 200 µm diameter plates. The inverse surface curvature was calculated from the average of the curvatures along the longitudinal and transversal axes of the scanner.

measured at 11 cm ± 3 cm overall. The deviation from these values, however, varied significantly between designs. Outliers were not confined to a specific chip, damaged or not; they can be considered as extreme cases of fabrication imperfections. In general, larger (400 µm diameter) mirror plates show more consistent curvature than smaller (200 µm) diameter plates. This is not surprising, as a similar height difference across the whole surface affects the curvature of smaller plates more.

In total, seven undamaged chips were then bonded for dynamic characterisation. The characterisation process was as follows: Doppler vibrometry measurements [187] of the frequency response, followed by dynamic white-light interferometry measurements [188] of specific mode shapes. The variable parameters were the actuation voltages and number of actuators used, as each device consists of four independent actuators instead of one. For characterisation measurements, only one actuator was used most of the time, typically always on the same southwest[1] quadrant. This was done to limit wear on actuators and ensure the MEMS would still be usable should one actuator fail: since each actuator/electrical contact pad group forms its own electrical circuit, a short from burning through the piezo material would not affect the operation of other actuators.

The frequency response of each device was measured for actuation frequencies up to 410 kHz to determine typical resonance values. The vibrometer used is a Polytec OFV512, measuring vibration up to 1.5 MHZ. Measurements were repeated on adjacent mirror quadrants, to make a rough characterisation of the mode shapes as piston, tipping, or tilting based on the relative displacement for each quadrant. Corresponding optical angular ranges were calculated for non-piston modes with the assumed rotation axis. As the Doppler vibrometry only gives a vertical velocity reading at the examined point, this was done by integrating the sinusoidal velocity signal through the simple relation:

[1]Orientation of the chip is chosen from the arbitrary orientation of the layout: the long side of the half die defines the west/east axis, with the square mirrors situated at the northwest corner of the die. This orientation is used through all of the following

Table 3.3: Comparison of the variation among resonance frequencies and amplitudes for the studied sample of 7 chips.

Plate diameter	200 µm			400 µm		
Mode	Tilt II	Tip I	Tip II	Tilt II	Tip I	Tip II
Average frequency (kHz)	174.7	332.2	406.5	45.4	86.6	104.4
Standard deviation (kHz)	3.1	6.0	7.8	1.0	1.7	2.2
Standard deviation (% of mean)	2.8%	1.8%	1.9%	2.2%	2.0 %	2.1%
Average mechanical amplitude at 20 Vpp (degrees)	3.5	5.5	4.5	3.6	7	6

$$x(t) = A \sin \omega t \tag{3.6}$$

$$v(t) = \dot{x}(t) = A \times \omega \cos \omega t \tag{3.7}$$

with $\omega = 2\pi f$ being the movement pulsation in radians per second, and A the displacement amplitude. Thus, the displacement amplitude is the velocity amplitude divided by the actuation pulsation.

White-light interferometry measurements were done using a WYKO Vision NT1100, with a vertical resolution of 1 nm. Static measurements were done under continuous illumination, while dynamic measurements were done using stroboscopic illumination synchronized with the motion of the scanner.

A typical frequency response is shown in Fig. 3.14. Variations in the resonance frequencies for similar modes exist between devices, with discrepancies of several kHz for Q factors of 110-150 for the 400 µm diameter scanners and 220-250 for the 200 µm diameter ones (see Table 3.3), giving typical resonance linewidths of 1 kHz.

Hysteresis also appears in the frequency response of scanning mirrors at actuation voltages greater than 5 Vpp, due to nonlinear behavior of the structure; highest displacement amplitudes can be achieved when approaching the resonance from lower frequencies. This issue was observed on all the devices to a similar extent. Among out-of-plane rotation modes, tipping modes exhibit the largest hysteresis ranges, likely because of the highly non-linear flexion of the mirror suspension beam. This effect must be kept in mind when actuating the device. Typically, mirror displacement was

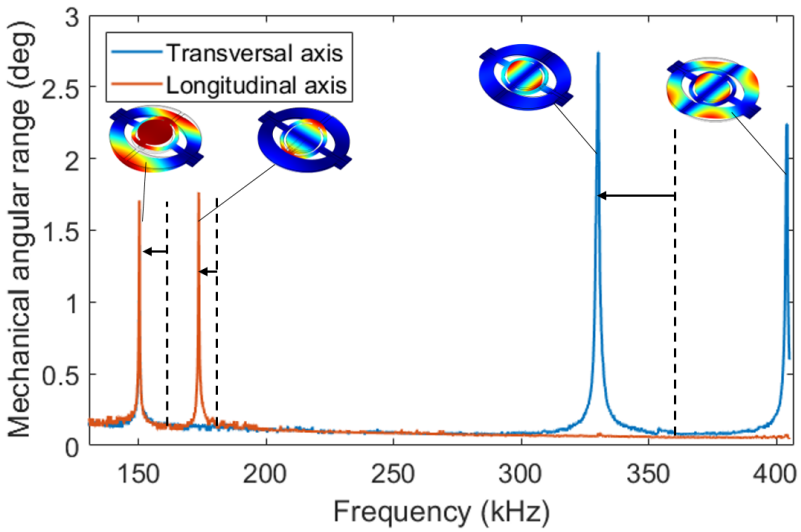

Figure 3.14: Typical frequency response for a scanner with a 200 μm diameter plate. The response was obtained using Doppler vibrometry at two different points near the edge of the mirror plate to measure the out-of-plane displacement along each rotation axis. Dotted lines indicate the simulated frequencies of the respective eigenmodes.

observed to quickly fall down to the lower amplitude when the actuation frequency gets close to resonance. Higher driving voltages push this fall down limit further, alleviating the problems of hysteretic behaviour, see Fig. 3.15.

This overview of device performance brings some useful observations. Table 3.3 illustrates the displacement/frequency dichotomy of the tested geometries: the larger devices with increased actuator size display high displacements at the cost of lower resonance frequencies, while devices with smaller actuators have faster, shorter resonant motions. The mechanical coupling obtained through the gimbal geometry enables significant displacement (nearly 8° of optical range) even at frequencies much higher than 100 kHz.

Voltage limits Voltage limits were also investigated, using the device with the 'long arm' geometry. Initial observations indicated that negative voltages under -15 V could lead to permanent depolarization of the piezo film, rendering the actuator unusable. Additionally, the device was tested for upper DC voltage limits. This was done by examining the device under white-light interferometry while gradually increasing the

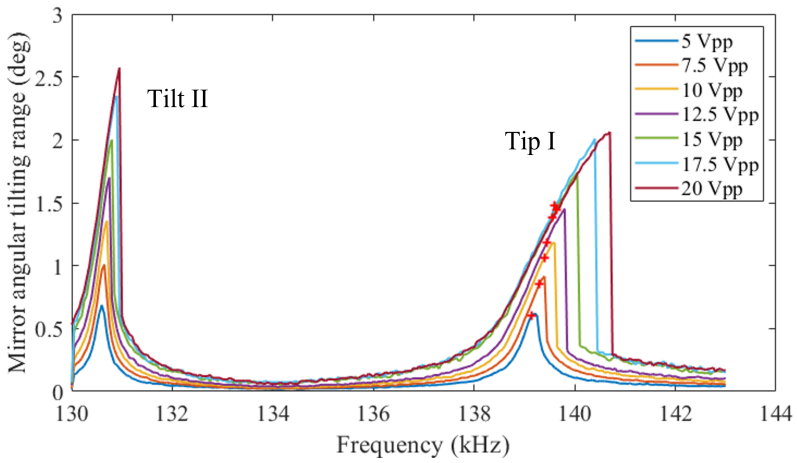

Figure 3.15: Frequency response of a tunable scanning mirror (see section 3.4) for various actuation voltages, measured in ascending frequencies. Note the onset of hysteresis as the actuation voltage increases. Red crosses indicate the resonance peak measured for descending frequencies, showing the extent of the hysteresis cycle.

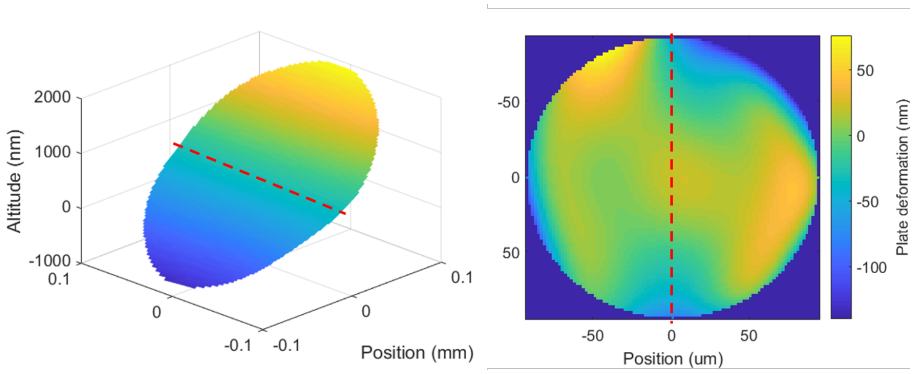

Figure 3.16: Dynamic deformation at the point of highest angular deflection for a 200 µm diameter scanner actuated at its first tipping mode at 329.4 kHz, with 20 Vpp on one actuator. The right picture shows the effective deformation after subtraction of the scanner's tilt and rest curvature. The red line indicates the rotation axis, perpendicular to the scanner suspension beam.

DC voltage applied to one actuator. Surface damage was observed from 60 Vdc, and was followed by permanent actuator breakdown at 80 Vdc. The actuator was rendered unusable after this measurement. Surface damage was visible near the extremity of the actuator, notably where the piezo material layer overlaps with the silicon oxide insulation layer; as this is also the point where the suspended structure is connected to the whole die, it is likely a point subject to high stress during actuator deformation, leading to the formation of a short circuit appearing through the piezoelectric film in this area.

This measurement gives a good estimate of the actuation voltage limits. Since it was made using DC actuation, we could expect AC actuation to have higher absolute voltage limits, but in the following the DC limit was used in all cases to reduce the risk of actuator damage.

Dynamic deformation Another important point in optical considerations is dynamic deformation of the mirror plate during operation. While the devices studied have a secondary frame surrounding the mirror to limit deformation, it can still be a source of optical aberrations, especially for larger displacements. Dynamic deformation was evaluated for a given time in mirror movement by correcting the surface profile for tilt (second and third Zernike coefficients) and subtracting the surface profile at rest. The results show dynamic deformation of around 100 nm, or a quarter of a wavelength for visible light. An example of dynamic deformation measurement is shown on Fig. 3.16. This is comparable to deformation values found in other works [147, 189].

In an effort to improve the mechanical range of the device, the effect of using multiple actuators for driving was investigated. When using two actuators, the ones on the south side were connected in parallel to be driven with the same voltage signal. This led to an increase in optical angle at resonance of about 90% depending on the actuation voltage – from 5°to 9.5°at 60 Vpp. The optical ranges at resonance for various driving voltages and number of actuators used are shown on Fig. 3.17. This figure shows the nonlinear influence of actuation voltage on resonant amplitude, and the voltage-independent increase in amplitude when a second actuator is used.

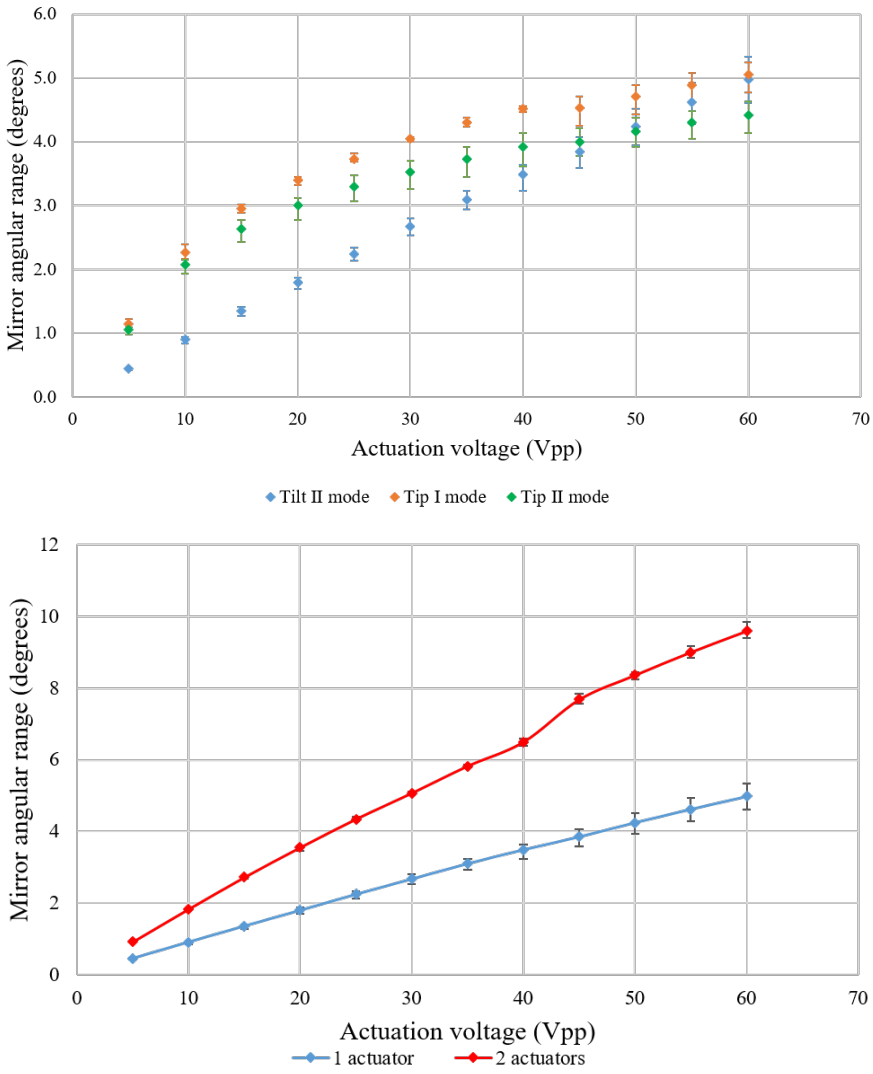

Figure 3.17: Top: evolution of the angular range of a 400 µm diameter mirror with actuator voltage for various modes, with one actuator used. Bottom: comparison of the angular range for the second tilting mode with one and two actuators used. The values are averaged over a sample of 4 devices. Error bars indicate the extreme values for the sample.

Table 3.4: Simulated changes in resonance frequencies for various thicknesses of added material onto the mirror plate. The values are calculated for a 175 µm disc deposited on top of the 200 µm mirror plate. It also gives the simulated change for a reduction of the mirror hinge with from 25 µm to 20 µm for comparison.

Geometry modification	Tilt II (kHz)	Tip I (kHz)	Tip II (kHz)
Default geometry	183.1	360.3	438.4
1 µm Al	181.3 (-0.98%)	356.3 (-1.11%)	437.9 (-0.11%)
2 µm Al	179.5 (-1.97%)	351.5 (-2.44%)	437.1 (-0.30%)
3 µm Al	177.7 (-2.95%)	346.7 (-3.77%)	436.4 (-0.46%)
20 µm wide mirror hinge	169.0 (-7.72%)	359.0 (-0.35%)	437.6 (-0.19%)

3.4 Frequency tuning for MEMS scanners

3.4.1 Device design for frequency tuning

Precise control of the scanner actuation frequencies is critical for addressing performance and synchronisation; Chapter 5 will show in more detail how addressing speed and point density are directly affected by the choice of the scanning frequencies, while addressing precision is affected both by pulse timing and scanning frequency precision. The latter is not an issue, as resonant designs exhibit great frequency stability when actuated, and actuation signals can be generated with high precision in the frequency range of interest, with commercially available signal generators reaching sampling rates of several megahertz for arbitrary waveforms. The available actuation frequencies are limited however, by the relatively narrow bandwidth of $\sim$1 kHz depending on the mode of the resonance peaks of the scanners. Furthermore, the discrepancies in resonance frequencies between scanners with identical designs stem purely from manufacturing tolerances, and as such cannot be predicted accurately for the given fabrication processes, further complicating the selection of actuation frequency. In order to correct these discrepancies and ensure a wide interval of possible actuation frequencies, methods of on-chip tuning of the resonant frequencies of the scanners after fabrication are highly desirable.

Tuning through mass change. As a first approach to frequency tuning, the possibility of correcting frequency discrepancies by adding or removing mass from the device

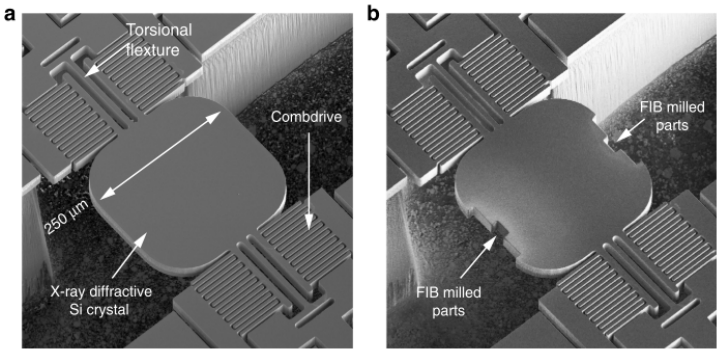

Figure 3.18: Example of scanner resonance frequency adjustment through mass removal by ion beam ablation. Reproduced from [190] under Creative Commons licence CC BY 4.0 .

was examined. In practice, this could be achieved by coating the scanner with an additional material layer, a process that may also be used to improve mirror reflectivity. The added mass was expected to change the mechanical response of the device, resulting in a diminution of resonance frequencies. However, simulations made with COMSOL suggested that the effective frequency change would not be significant for realistic coating thicknesses, as shown on table 3.4; this was later confirmed by frequency response measurements on devices coated for improved reflectivity.

Removing mass from the scanner could be a way to produce the opposite effect, pushing the resonance frequency upwards. Controlled ablation of MEMS scanners for frequency tuning was previously demonstrated in [190], as shown on Fig. 3.18. This process, however, requires precise ion milling in an iterative approach to avoid overshooting the target frequency. In either case, changing the mass of the device is an irreversible process involving the risk of an overshoot and increased post-processing time for the fabricated devices.

Tuning through variable stiffness. A reversible way to modify the mechanical response of the scanner can be achieved by applying an additional mechanical constraint to the suspended structure, thus changing the stiffness of the device. This kind of reversible tuning was already demonstrated for MEMS resonators in [191], where a scissor-shaped holder applies a controlled pressure to the torsional spring of the res-

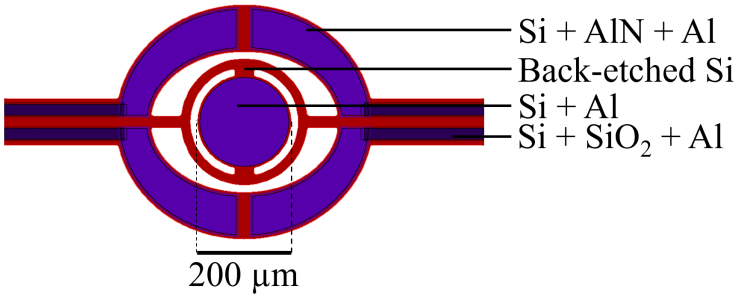

Figure 3.19: Schematic of the 200 µm diameter scanner with longer beams for frequency tuning.

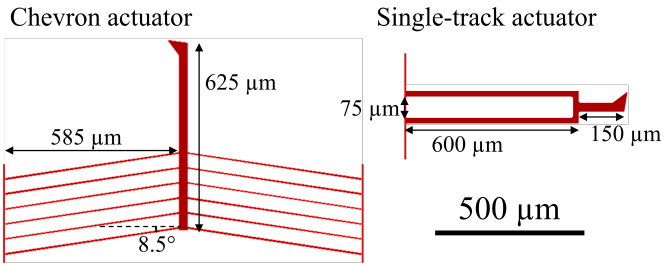

Figure 3.20: Schematic of the thermally actuated silicon tips used for frequency tuning.

onator and varies its mechanical stiffness. This method uses a flexure beam on the holder to allow for continuous tuning of the resonator, for a maximal frequency change of more than 10%. This method presents the advantage of not requiring any materials other than those already used for the fabrication of the scanner, as the tuning structure can be fabricated on the same chip, and only needs additional actuators for the displacement of the tuning elements. However, it cannot be adapted to already produced devices and requires fabrication of a new design.

The modified scanner design used in this thesis is shown on Fig. 3.19. It features longer suspension beams to allow the placement of silicon tips on either side, which can be actuated to make contact with the beam and change the effective spring stiffness of the structure. Simulation shows that the elongated suspensions translate into an expected reduction of the tipping mode resonance frequencies of up to 40% (for the tip I mode) relative to the original design, while the tilting modes see very little change (1.7% reduction for the tilt II mode).

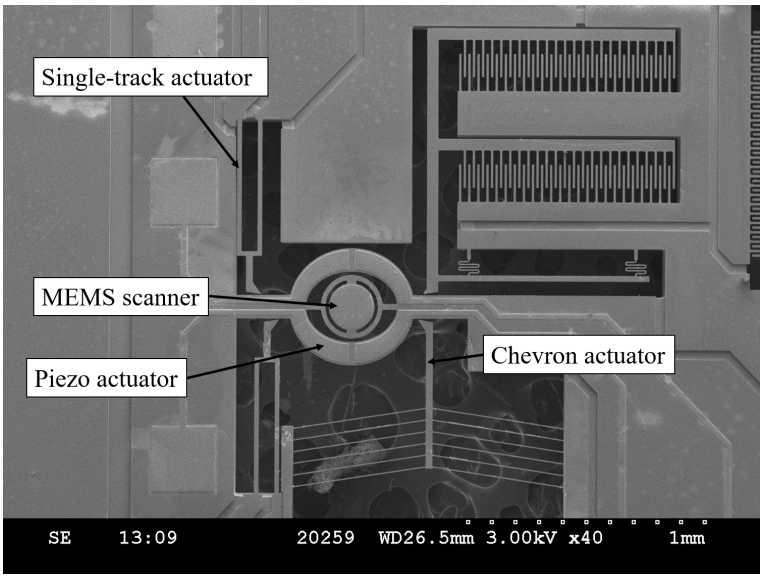

Figure 3.21: SEM image of a 200 µm diameter tunable MEMS scanner with the surrounding tuning tips. Top right is the ES actuator, unused in this work, and bottom left is another single-track actuator.

Three tuning tip shapes were included for stiffness tuning with varying actuation strategies. One of the shapes uses comb-fingers arrays for electrostatic actuation, while the other two use electrothermal actuation, pictured on Fig. 3.20. The electrostatically (ES) actuated tip uses spring shaped suspensions in order for the comb-drive array to displace the tip structure through ES forces when a voltage is applied to the fixed array. The thermal tips use heat expansion from Joule heating to generate displacement: a single-track actuator uses one pair of thick beams to push forward as the long side of the suspended structure expands, while a chevron actuator uses thin beam pairs producing displacements by in-plane buckling as the heat causes them to expand. This latter principle was previously demonstrated in [135] to produce up to 10 µm of in-plane displacements with less than 10 V of applied voltage. The design layout specified a gap of 5 µm between the tuning tips and mirror suspension beam structure, the smallest gap allowed by the fabrication tolerances. Furthermore, two tips with single-track actuators were placed with different contact points with the scanner suspension beam to evaluate the effect of tip position on the stiffness change.

The tunable device was fabricated using the PiezoMUMPs process. The manufac-

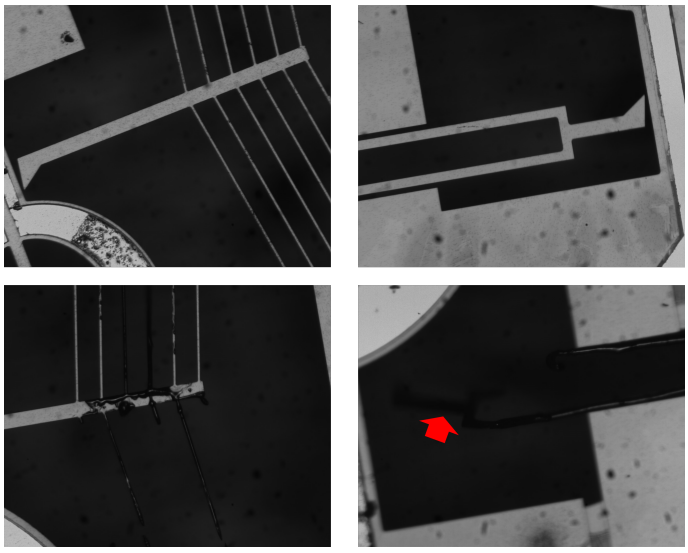

Figure 3.22: Left: Chevron actuators, at rest (top) and after being damaged from excessive heating (bottom). The damaged thin beams experienced partial melting and breakage. Right: same pictures for the single-track actuator. The actuator is heavily deformed and bent out of plane due to partial melting (red arrow).

tured chips integrated an aluminium coating for the 200 µm diameter scanners, with the 500 nm metal thick layer being directly deposited on the mirror plate for improved reflectivity; reflectivity was measured to be approximately 60% for incident light at 633 nm. An SEM image of a fabricated scanner is shown on Fig. 3.21. The chips fabricated showed no defects, and the tip gap was within tolerance.

The chips were mounted on carrier boards and wire-bonded for operation. Initial characterisation of the tuning tips, with no actuation of the scanner and voltage being applied to the tips only, showed the following :

- the breakage threshold for thermoelectric tips is approximately 12.5 V, where excessive heating leads to suspension beams partially melting and snapping under the resulting strain (see Fig. 3.22). In the following, actuation voltage was limited to 10 V to avoid damage to the actuators. No breakage or pull-in was observed for the electrostatic tips, for voltages up to 100 V;

- the chevron actuator can produce enough displacement to reach contact with the scanner suspension beam with approximately 8 V applied to it. The single-

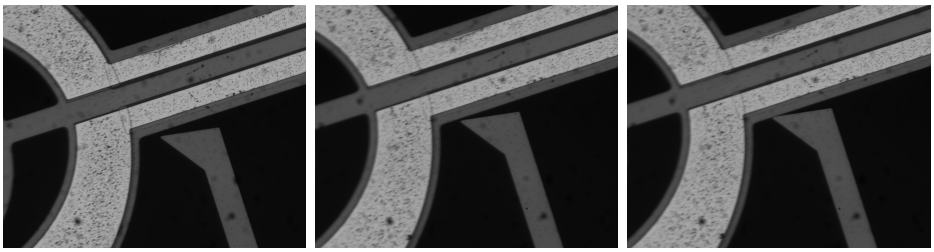

Figure 3.23: Microscope pictures of the chevron tip with 0 V, 7 V, and 9.7 V applied to the tip actuators respectively. The initial gap between tuning tip and suspension beam is approximately 6.5 µm.

track actuator cannot produce enough displacement to reach contact, but the gap between the tip and the scanner can be significantly reduced with 10 V applied to it (see Fig. 3.23);

- the electrostatic actuator cannot produce significant displacement of the tip for voltages up to 100 V. This is likely due to insufficient comb-finger count and overlapping surface, even with the comb-fingers properly aligned in-plane, resulting in a force too low to overcome the stiffness of the tip spring structure.

Further characterization efforts focused on the tips with thermoelectric actuation. The result of measuring scanner performance with the tuning tips being actuated are described below.

Tuning through localized heating While the original expectations for frequency tuning were to observe a sudden increase in frequency when the tips made contact with the scanner suspension beams, measuring the resonant frequency of the scanner as the tip voltage varies shows a variation of said frequency even without tip contact. Fig. 3.24 shows a graph of this variation. While a sudden change can clearly be seen when the chevron-actuator tip reaches contact with the scanner, it appears that a non-contact effect also affects the resonance frequency. From this graph, we can infer that this effect is in fact localized heating by the electrothermal actuators. Indeed, the proximity of the hot tuning tip – approximately 10 µm at rest – to the scanner structure can justify this heating effect; no other non-contact effect should otherwise exist between the tip actuator and the scanner, as they are electrically insulated from each other until

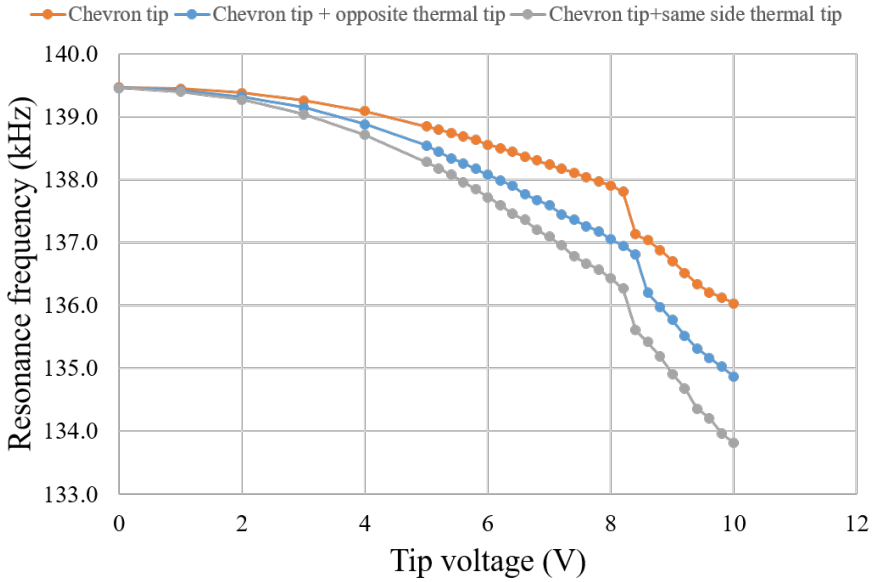

Figure 3.24: Graph showing the evolution of the first tipping mode frequency of a 200 µm diameter scanner with increasing tuning tip voltage. Note the sudden decrease indicating when the chevron tip makes contact with the scanner.

contact. Furthermore, the dependency of the resonance frequency on actuator voltage is quadratic. If we approximate the change of the resonance frequency with temperature as linear, motivated by a uniform, linear change of material elasticity [192], this is coherent with Joule effect heating where the equilibrium temperature of the tip is linearly affected by the electrical power dissipated, itself proportional to the square of actuator voltage.

Frequency tuning by non-contact heating presents many advantages over mechanical contact tuning: the frequency change can be finely controlled in a continuous manner, whereas tip contact only acts as an all-or-nothing method; and it can be achieved with lower displacement than what is required for mechanical contact. It thus succeeds in providing a controlled, reversible method of tuning the frequency of the mirror. A frequency shift of more than 4 kHz, corresponding to a relative change of 8%, was achieved with this method for the first tipping mode, with the tuning beams reaching temperatures of approximately 550 °C for the chevron tuning beam, and 700°C – corresponding to a red hot glow – for the single-track actuators at maximum tuning voltages. The

Table 3.5: Comparison between tuning effects and main suspension beam motion for various scanning modes of a 400 µm diameter mirror. Note the lower resonance frequencies compared to the non-tunable design due to the longer suspension beams.

Mode	Typical base resonance frequency (kHz)	Relative frequency reduction at 10 Vdc (%)	Main suspension beam motion
Tilt II	53.7	0.7	None
Tip I	56.5	8.3	Strong flexion
Tip II	102	1.7	Weak flexion

tuning effect was observed to be much weaker for tilting modes, resulting in a relative change in frequency of only 0.7% at most; this is likely a result of a weaker coupling of the suspension beam with the scanner plate for these modes. For the tilting mode, the mechanical spring function is mostly realised by the inner torsion beam and involves axial torsion rather than out-of-plane flexion, thus limiting the impact of a localized stiffness change in the main suspension beam. Table 3.5 summarizes the tuning effects for each studied mode and the relationships between suspension beam motion and scanner motion.

Regarding displacement amplitude, each mode is again affected differently by tuning. Tilting modes exhibit an initial increase in amplitude, followed by a sudden decrease (shown on Fig. 3.25) past a certain point which depends on the tuning configuration and may occur before or after contact with the chevron tip; this was observed to various degrees on each tested device. While the resonance frequency of this mode is only weakly affected by thermal tuning, it is possible that there exists a temperature for which the structure stiffness produces optimal displacement. For tipping modes, a slight decrease in amplitude is typically observed, corresponding to a reduction of at most 12% when going from no tuning to the maximal tuning value (10 Vdc on each of the three thermal tips) for the first tipping mode.

The addition of thermoelectric actuators has a significant impact in term of power consumption. The single-track actuators required approximately 300 mA for a 10 Vdc signal, while the chevron actuator required 270 mA, bringing the total power consumption to 9 W for maximum tuning. This is several orders of magnitude greater than the consumption of the piezo actuators alone and must be taken into account when

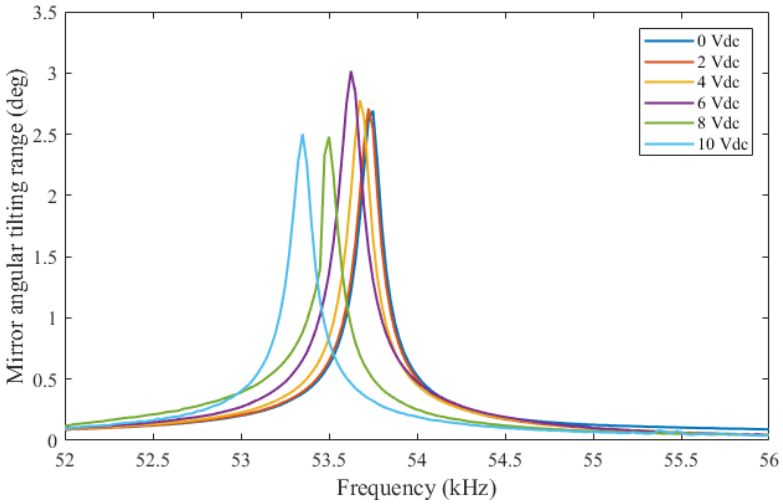

Figure 3.25: Evolution of the frequency response for the second tilting mode of a 400 µm mirror with the voltage applied to the three thermal tuning tips.

considering applications where electrical power and current are limited.

In general, the observed change in amplitude due to tuning, while significant, can be compensated by adjusting the actuation voltages so that the angular range remains similar to that obtained without tuning; special care should be taken when near the contact point in the chevron tip, as contact induces a sudden change in equilibrium temperature, and may consequently affect both resonance frequency and amplitude.

3.4.2 Frequency selection for Lissajous scanning with tuning

In the following, we examine how frequency tuning can be used for selecting Lissajous scan frequency. More details about Lissajous scanning are given in appendix B and chapter 5, but what follows pertains mainly to evaluating tuning performance.

Let us assume that we want to use a specific mode for each scan axis with initial resonance frequencies of $f_{1,r}$ and $f_{2,r}$ respectively, with a full-width at half maximum (FWHM) of w_r. Furthermore, let us assume that each mirror can be tuned so that the resonance can be increased or reduced by at most w_t. The acceptable range of axial frequencies for either axis is then $f_{i,r} \pm (w_r/2 + w_t)$. Consequently, the maximal

Lissajous scan frequency that can be achieved for these axial modes is

$$f_{\mathrm{Lmax}} = \max(\gcd(f_1, f_2) | f_i \in [f_{i,r} - (w_r/2 + w_t), f_{i,r} + (w_r/2 + w_t)], i = 1, 2) \quad (3.8)$$

where the values of f_1 and f_2 in hertz are assumed to be integers, and *gcd* is the greatest common divisor. While the value of f_{Lmax} depends on the initial resonances $f_{i,r}$, the effective tuned resonance width allows for a lower bound for the maximal scanning frequency :

$$f_{\mathrm{Lmax}} \geq w_L = w_r + 2w_t \quad (3.9)$$

since there always exists a value $f_{i,t}$ in the interval $f_{i,r} \pm (w_r/2 + w_t)$ such that $f_{i,t} \mod w_L = 0$ and thus $\gcd(f_{1,t}, f_{2,t}) \geq w_L$. If we assume values for w_r and w_t of 1 kHz and 3 kHz respectively, a conservative estimate given the previously obtained results, we have $f_{\mathrm{Lmax}} \geq 7$ kHz, a value comparable to the standard deviation of 7.75 kHz measured for the second tilting mode in the sampled 200 µm diameter scanners, the largest deviation for out-of-plane modes.

As will be discussed in chapter 5, the effective point addressing frequency will then be twice the Lissajous scan frequency. Furthermore, if the wrap-around condition is verified, that is if one of the axial frequencies is an even multiple of the Lissajous frequency, the point addressing frequency will be four times the Lissajous frequency instead. However, this latter property does not affect the frequency selection process, as satisfying this condition is equivalent to dividing the lower bound by 2: indeed, the greatest value w'_L for which there is always a value $f_{1,t} \in [f_{i,r} - (w_r/2 + w_t), f_{i,r} + (w_r/2 + w_t)]$ such that $(f_{1,t} \mod 2w'_L) = 0$ is $w'_L = w_L/2$. Thus the Lissajous scan frequency is halved to double the point addressing frequency relative to it, and the absolute point addressing frequency remains the same, for a similar scan density (illustrated on Fig. 3.26).

The above shows how frequency tuning allows for better optimization of frequency selection for high speed Lissajous scanning. In particular, it allows for frequency selection independent from initial resonance frequencies by broadening the frequency range at which the scanners can operate, without excessively compromising motion amplitude

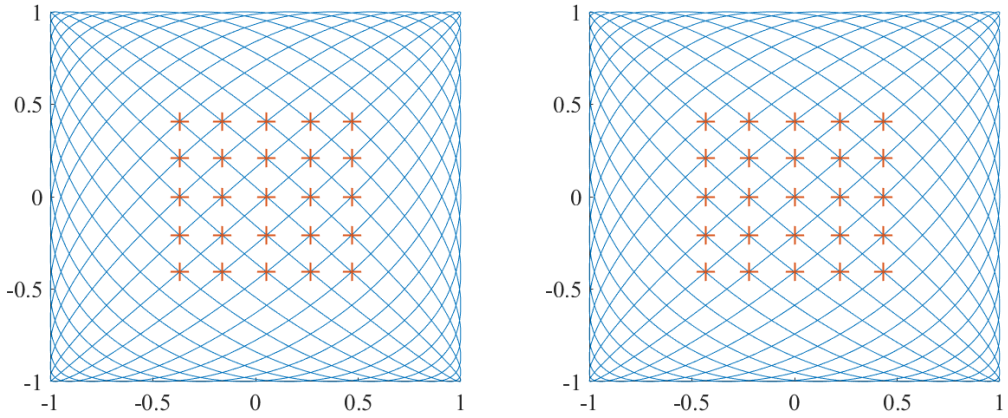

Figure 3.26: Comparison of doubled and non-doubled Lissajous addressing patterns. Left: $f_1 = 90$ kHz, $f_2 = 87$ kHz (doubled curve); right: $f_1 = 90$ kHz, $f_2 = 84$ kHz (non-doubled). Each grid point (red crosses) is visited 4 times per scan cycle on the left figure, and only 2 times on the right. In both cases, the average addressing frequency for any grid point is 12 kHz.

– which would be severely reduced if the device was actuated off-resonance. Thus, it constitutes an effective solution to the frequency discrepancies existing between fabricated devices. It also provides a way towards an adaptable design where the scanning frequency can be changed based on current scan density and speed requirements.

This section demonstrated frequency tuning by both thermal and mechanical effects. These effects produce frequency changes large enough to mitigate the frequency discrepancies observed between individual devices and facilitate frequency selection for scanning configurations involving multiple mirrors. The remarkable difference in tuning sensitivity between tilting and tipping modes may also be exploited in future experiments to achieve two-dimensional Lissajous or circular scanning with a single mirror.

3.5 Thermal effects and operational limits

As was initially stated in the research framework (section 1.3), maximum admissible optical power is an important metric to consider for evaluating scanning performance. Many atom trapping and quantum optics applications benefit from higher laser powers due to the dependence of Rabi frequencies on laser intensity (see chapter 2). While

macroscale optics can easily accommodate several Watts of optical radiation, the small surface of MEMS scanners results in high power density and poor heat dissipation through natural conduction and convection, while their low mass and consequently low heat capacity makes them susceptible to rapid heating; both effects lead to potentially high equilibrium temperatures being reached when exposed to incident radiation, which in turn cause changes in scanning performance and ultimately permanent damage to the scanner. This is true in particular when operating at wavelengths where the scanning mirror exhibits poor reflectivity. A quick estimation reveals this limitation: a 1W circular beam with a 200 µm diameter corresponds to a power density of approximately 3.2 kW/cm^2. A 10 µm thick circular scanner with the same diameter has a heat capacity of approximately 2.3 µJ/K at 400 K [143]; with a 99% reflectivity, this scanner would absorb 10 mW of power, five thousand times its heat capacity per Kelvin every second. This brief calculation is of course not realistic, as it considers the mirror plate in a thermal vacuum, but is helpful in showing how differences in scale can result in extreme effects for MEMS devices, even for commonly used power values.

This rough estimation can be refined in a more quantitative model by considering thermal effects leading to heat dissipation, within the context of the fabricated device, that is a suspended MEMS attached to a silicon die and operating in room temperature and pressure. In these conditions, it can be expected that heat conduction and natural convection will have a significant influence on temperature distribution.

3.5.1 Thermal effects simulation

While building an analytical thermodynamic model taking these effects in account would be challenging, they can be computed by simulation software. The device geometry already reproduced in COMSOL for frequency analysis was used for a thermodynamic simulation in order to approximate the temperature distribution within the device for a given incident beam power. The suspended structure was simulated by considering the silicon die as a heat sink, the boundaries in contact with the die being defined as a fixed temperature. This boundary temperature, along with the incident optical power, were used as variable parameters to examine the effects of different boundary

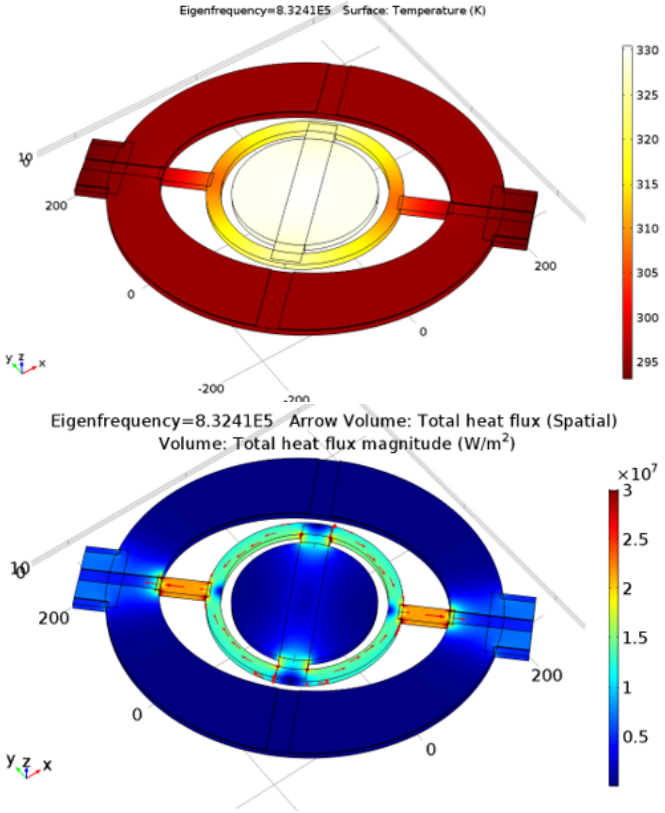

Figure 3.27: Results from the thermal simulation in steady state. Top: temperature distribution across the profile. Bottom: heat flow through the scanner structure. Simulation for 100 mW of absorbed radiation centered on the mirror plate and hinge extremities fixed at 293 K.

configurations on the temperature distribution, taking in account their evolution with temperature changes. Natural air convection was handled natively by the simulation software. The materials properties for heat conduction and thermal expansion were found in [143]. Figure 3.27 shows a typical temperature distribution profile obtained from this simulation.

While the resulting temperature profile appears to be quite intuitive, the heat flow distribution reveals that most of the heat transfer happens through the mirror plate suspension beam. Indeed, the thin (200 µm^2 cross section) beams act as a bottleneck between the mirror plate and the die bulk. Since any active cooling must be implemented through the die, this may act as a limitation to such methods. Figure 3.28 shows the influence of varying die bulk temperatures, including some lower than room temperature

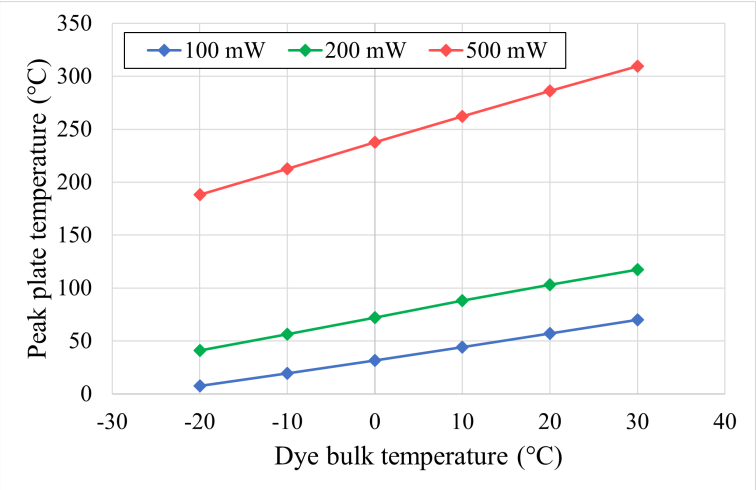

Figure 3.28: Variation of the simulated steady state temperature of the 200 µm mirror plate for different values of the fixed bulk temperature. Each line corresponds to a different value of absorbed radiation power.

to represent active cooling effects, on peak mirror plate temperature.

The above results show how a cool bulk die only has a limited effect on mirror plate temperature, a consequence of the limited heat transfer through the suspension beams. Furthermore, when operating in normal atmospheric conditions, die temperatures under 4°C can induce dew condensation on the chip surface. The formation of water droplets can then negatively impact the device performance and lead to permanent surface damage.

Once a steady-state temperature distribution is obtained, a mechanical frequency analysis can be run again to evaluate the eigenfrequencies of the heated device while taking in account thermal expansion. The eigenfrequencies were evaluated once again for various combinations of thermal parameters, giving a prediction of their evolution as the scanner temperature rises. This data is shown on Fig. 3.29.

While some eigenmodes follow a mostly linear evolution with temperature, some eigenfrequencies see a change in regime past a certain point manifested by a jump in eigenfrequency, such as the astigmatic mode on Fig. 3.29. Others become imaginary, in the mathematical sense – the tip I, piston I and tilt I modes on the same figure. From a physical standpoint, this is interpreted as the corresponding modes vanishing due to changes in the mechanical properties of the structure. This effect correlates with

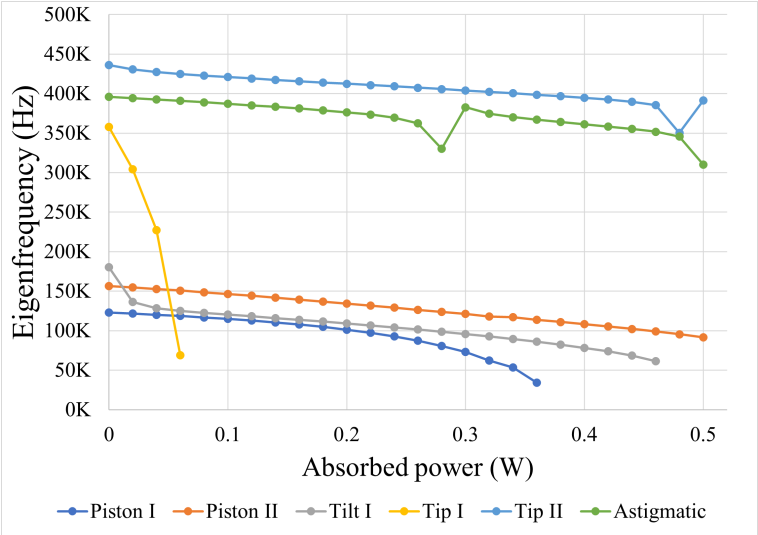

Figure 3.29: Variation of the eigenfrequencies of various simulated modes with absorbed power for a 200 µm diameter scanner. Values for which the eigenfrequency is imaginary are omitted.

the change in relative displacement observed for certain mode shapes, as variations in spring stiffness affect mechanical coupling within the resonant structure. This effect is shown on Fig. 3.30.

In conclusion, these simulation results provide useful insight in the effects of incident optical radiation on the performance of the scanner. First, by providing an estimate of the temperature distribution for a given value of absorbed radiation, thus giving bounds on the power levels that the device can realistically operate with; second, by linking the temperature distribution to the device's frequency response, showing how heating effects may affect scanning performance, and, in particular, by giving an estimation of the frequency shift of the scanning modes resulting from radiation heating.

An aspect that was not simulated here but remains of importance is the fact that frequency tuning through localized heating will induce an increase in mirror temperature, and effectively add another heat source to the system, thus lowering the damage threshold of the mirror. In general, the simulation results underline the importance of the coupling between device temperature and resonant response. Any application involving the scanners should therefore consider the levels of optical power involved and how it may impact their performance, along with other conditions such as ambient

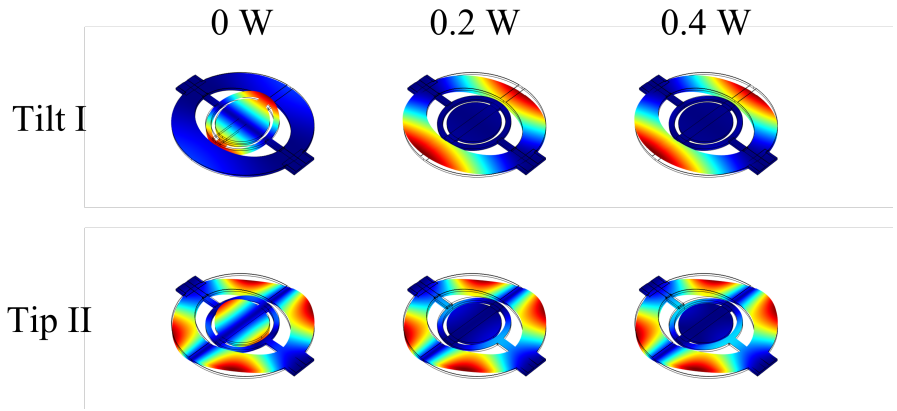

Figure 3.30: Illustration of mode shape evolution with absorbed power. The colorscale is arbitrary for each picture.

temperature and pressure.

3.5.2 Characterisation of radiation heating effects and damage thresholds

Experimental tests were conducted to determine the damage threshold of the scanners; that is the minimum incident power that may cause permanent damage to the mirror's surface. In addition to the frequency shift effects predicted by simulation, an expected consequence of radiation heating is changes in surface curvature as thermal expansion affects stress distribution within the mirror.

In order to measure scanner damage threshold under high incident power, the tested scanners were exposed to a 981 nm continuous wave laser diode (LIMO35-F100-DL980, fiber coupled) capable of delivering up to 35 W of average power. The incoming beam was focused down to a waist diameter of 140 µm ($1/e^2$) on the uncoated scanner surface with a normal incidence, corresponding to a peak intensity $I_{\max} = 2P/\pi w^2 = 3.25 \times 10^4$ W/cm^2 for a Gaussian beam with 1 W of total power. Given the small size of the devices, exposure of a few seconds was considered sufficient for the system to reach thermal equilibrium. For an uncoated 200 µm diameter scanner, with a reflectivity of 30% at 981 nm, permanent surface damage was observed after exposure to 700 mW of power, and partial melting of the silicon plate after exposure to 1.0 W.

A way to raise this limit to allow operation at higher power is to improve mirror reflectivity by adding a reflective coating layer, reducing the heating from absorbed radiation. A gold layer with approximately 100 nm thickness was deposited on some scanners, after masking using custom 3D printed masks to avoid shorting of the piezoactuators. The measured reflectivity after coating was only 60-65% at 981 nm, a low value compared to an expected reflectivity of at least 95% [193]. This low reflectivity might be due to the surface roughness resulting from the chemical vapour deposition process used for coating, leading to increased scattering away from the main reflection axis. Nevertheless, further measurements showed an increased damage threshold to 1.7 W of incident power, with plate melting observed after exposure to 2.4 W. This value might be increased further through the use of active cooling (see below).

Given these results, exposure to continuous radiation was considered safe for total incident power values up to 500 mW, or maximal intensity values of 1.6×10^3 W/cm^2 for uncoated devices. Even when operating under incident of 10 mW or greater, care should be taken as the frequency shift induced by heating effects may require compensation to keep the actuation signal on resonance. This effect was observed in another experiment using these MEMS scanners [194] and the corresponding shifts are shown on Fig. 3.31. The frequency shifts measured experimentally are about three orders of magnitude lower than the simulated shifts for equivalent absorbed power; it is likely that incorrect modelling of thermal effects led to an overestimation of the frequency shifts in the simulation model.

3.5.3 Active thermoelectric cooling for MEMS scanner

Mitigating the effects of heating on MEMS scanners can be done in several ways. One can seek to increase mirror reflectivity for wavelengths of interest, thus resulting is less absorbed radiation and thus reduced heating from incoming light. This method was studied in the previous section. Another method is to actively cool the device, draining the absorbed heat to reduce the equilibrium temperature for a given value of incident power, directly counterbalancing the effects of radiation heating.

The proposed implementation uses a Peltier cell, with the MEMS die placed on the

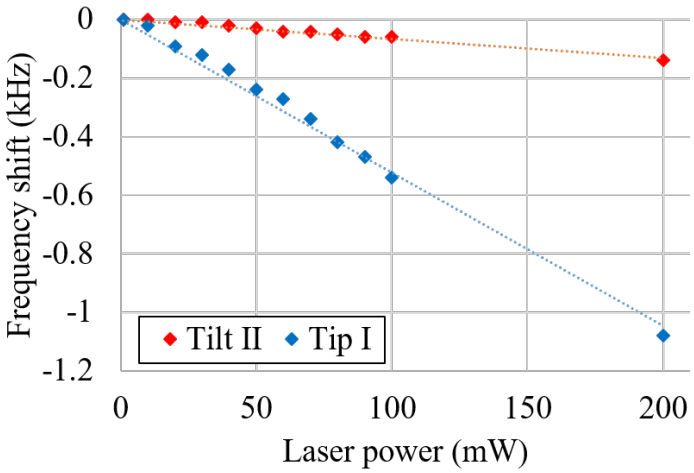

Figure 3.31: Frequency shifts of the second tilting and first tipping mode of a 400 µm diameter scanner with increasing incident power. Data courtesy of L. Herdly from the Strathclyde Photophysics group.

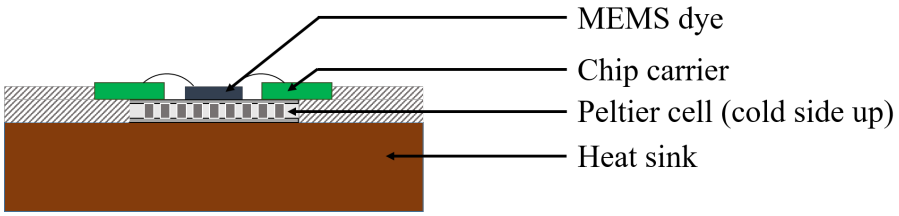

Figure 3.32: Layout of the thermoelectric cooling assembly. Thermal paste is applied on both sides of the Peltier cell to ensure good thermal conduction. Drawing not to scale.

cold side, and the hot side of the cell facing a heat sink. Heat conduction between the MEMS and the cell, as well as between the cell and the heatsink, is ensured by putting some thermal paste at the interfaces. Fig. 3.32 shows the structure of the cooling assembly, with the cell and MEMS carrier being fixed in place by a custom printed holder. Since the die needs to be in direct contact with the surface of the Peltier cell, the central part of the MEMS holder was drilled hollow such that it could be placed over the chip and wire-bonded to allow actuation. Wire-bonding was achieved after assembling the cell and carrier to the holder to ensure constant positioning during the bonding process.

Early tests showed that a heatsink that is too small may eventually be significantly

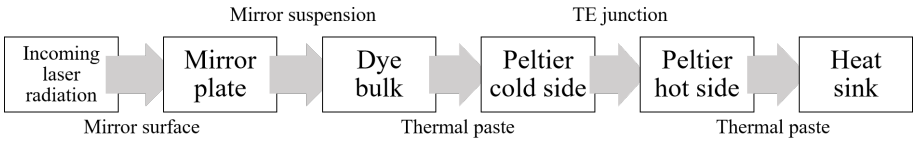

Figure 3.33: Summary of the TE cooling process. Heat is actively transferred from the cold side of the Peltier cell to its hot side.

heated by the thermoelectric (TE) cooling process, eventually resulting in a heat flow through the assembly and back into the MEMS chip. The heatsink used for power handling experiments was a 60x60x16mm aluminium sink, which proved to be able to dissipate enough heat when operating at high power, for durations of up to 10 minutes. It should be noted that regardless of radiation heating of the MEMS, thermoelectric cooling will result in a significant rise in temperature of the hot side of the cell, around 41 °C for an applied current of 1 A at rest. The cold side of the cell may conversely drop below room temperature, down to 9 °C for an applied current of 1 A with no additional heat sources, or even lower with a heat sink connected to the hot side. As mentioned previously, in normal room conditions, this can lead to condensation of surrounding humidity onto the MEMS surface and permanently impact the optical performance of the mirror. It is therefore important that the thermoelectric cell current be applied proportionately to the radiation heat absorbed. Fig. 3.33 summarizes the heat transfer process.

While the Peltier cell can theoretically drain several Watts of heat from its cold side (see Fig. 3.34), the main bottleneck remains the transfer from the MEMS device itself to the silicon die bulk, due to the small area of the suspensions, as mentioned above. We can thus expect that increasing thermoelectric cooling current will eventually fail to prevent increases in mirror temperature as a consequence of falling thermal conductivity in the silicon beams. This would in turn limit the heat flow out of the mirror plate, leading to increased thermal gradient rather than lower peak temperature.

We measured the effect of thermoelectric cooling by applying localized heating to a tunable scanner and measuring its frequency response for increasing values of the

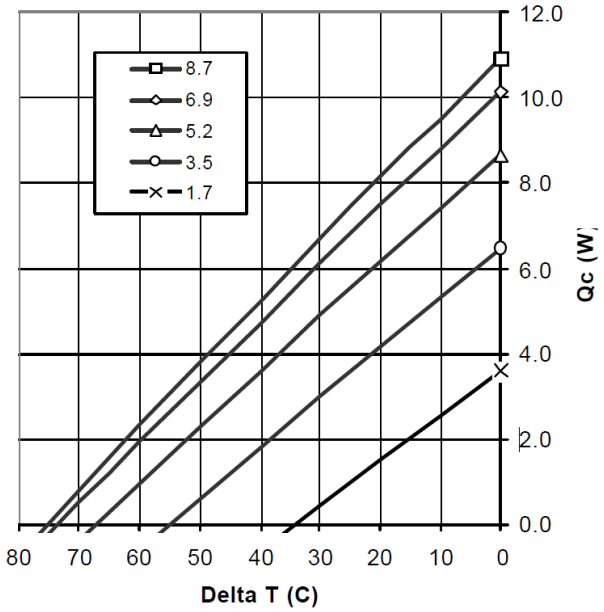

Figure 3.34: Specified heat flux through the Peltier cell as a function of input current (in amperes, shown in legend) and temperature difference between sides, for a hot side temperature of 50°C. Reproduced from the manufacturer specifications [195].

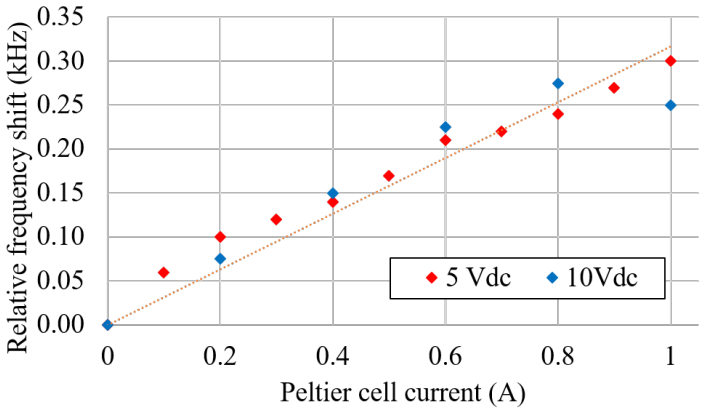

Figure 3.35: Relative frequency shift of the tip I mode of a 400 µm diameter scanner for two values of the chevron tuning tip voltage, as a function of Peltier cell current. The trendline is given for the 5 Vdc data.

Peltier currents. In this context, resonance frequencies are a useful measure of the equilibrium state of the scanner, as its temperature cannot be measured directly in this configuration; the data shown above suggests that resonance frequencies shift linearly with scanner temperature, with different linear coefficients for each mode. With this in mind, we can evaluate the effect of cooling against that of localized heating. Fig. 3.35 shows the measured frequency shifts for different base heating voltages.

These measurements show that thermoelectric cooling has a weaker impact on device temperature compared to localized heating, for an equivalent input power. The cooling produced a shift of 300 Hz at 1 A, whereas the shift due to tuning with 5 Vdc applied to the chevron actuator was -400 Hz, equivalent to an incident power of 75 mW based on the data shown on Fig. 3.31. When taking in account the reflectivity of the mirror plate, this value of equivalent power is much lower than the expected power flux through the Peltier cell – at least several hundred mW based on the specifications on Fig. 3.34. Furthermore, condensation on the die bulk was observed for high cooling currents, but not around the scanner area, indicating a strong temperature gradient around the suspended structure. These elements, combined with the simulation results, suggest that the heat flux through the MEMS suspensions is insufficient to compensate scanner heating.

3.6 Summary

This chapter has described the features of the scanners and examined their resonant behavior in detail, based on their frequency response and scan angles produced. External effects that may affect or be used to control this behavior were also studied, through simulation and experimental measurements.

The scanners can efficiently make use of resonant actuation and mechanical coupling to produce scan angles up to 9° mechanical, or 18° optical (Fig. 3.17). They exhibit high resonance frequencies in the 100-400 kHz range (Table. 3.3), compatible with the timescales of experiments described in chapter 2. The influence of thermal effects was exploited to compensate the discrepancies of several kHz in resonance frequencies existing between chips, with a thermal tuning system allowing a shift in frequency of up

to 8% (Table 3.5) ; this tuning capability greatly enhances synchronization possibilities when using multiple scanners (section 3.4.2).

Finally, optical power handling measurements showed that operation above 1 W of total incident optical power is possible with adequate metallic coatings, at the cost of a small but measurable reduction in resonance frequency in the order of 1 kHz (Fig. 3.31). Attempts to mitigate heating effects through active cooling were made but proved inefficient when taking in account the high power consumption required to achieve significant compensation (Fig. 3.35).

In light of the characterization results, the following chapters demonstrate how these MEMS scanners can be used in practical applications.

Chapter 4

Experimental demonstration of high-frequency 1D addressing

4.1 Optical design and basic applications

In order to demonstrate the optical performance of the selected high frequency scanner, a demonstration setup was designed, with the objective of showing how the device can be used to address points along a 1D space. The general layout of the setup is shown in Fig. 4.1.

The laser source used was a nanosecond pulsed laser diode (Thorlabs NPL49B) producing 488 nm laser pulses with a tunable pulse duration between 6 and 39 ns; the minimal pulse duration was used for all the measurements. Pulse triggering is controlled by an external input allowing arbitrary pulse sequences with a pulse frequency up to 10 MHz. The addressing pulses emitted from the source are coupled into a single mode fiber to ensure a TEM00 Gaussian beam shape. Due to the high divergence of the diode's output and the likely wide mode spread, along with experimental limitations, a coupling efficiency of only 2% was achieved, reducing the 20 mW average pulse power to approximately 400 µW. This is not problematic for the purposes of this demonstration, as the pulses need only to have enough intensity to be detected at the target plane. The power detected on the target plane is estimated to be less than 1% of the power output at the diode when taking in account other optical losses, on the scanning mirror

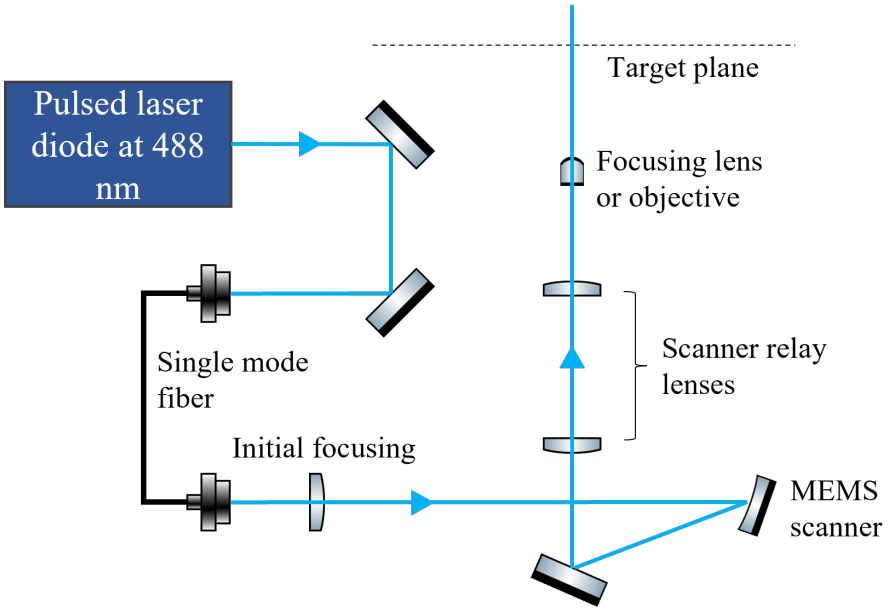

Figure 4.1: General layout of the 1D demonstration setup. See text for details. Not to scale

in particular, as the silicon surface has low (approx. 45%) reflectivity at the used wavelength.

4.1.1 MEMS actuation

The MEMS device is actuated using a commercial signal generator (Agilent 33250A) allowing simple control of the driving signal amplitude and frequency. The generator was connected to a 1 MHz bandwidth voltage amplifier (FLC F20A), for actuation voltages up to 60 Vpp. A second signal generator and amplifier was used for measurements involving all four actuators, using the built-in 10 MHz synchronization signal to ensure that each pair of actuator (north and south) was receiving opposed signals to drive a tipping mode.

The setup was tested with a 20 Vpp+10 Vdc sine wave applied to the mirror. Measurements made with different driving signal shapes (sine, square, triangular) showed no significant change in mirror movement shape, as the mechanical structure filters out higher frequency components in favor of the resonant mode.

4.1.2 Laser driving requirements

Although there is no minimum power needed for the demonstration setup, the speed of the laser pulse source will impact the addressing performance. The relevant values to characterise source speed in this context are pulse repetition rate and pulse duration.

For a mirror being actuated at a frequency f_{scan}, with a sinusoidal motion, the mirror will scan the entire addressed length L in half an actuation cycle, that is over a duration $T_{\text{add}} = 1/2f_{\text{scan}}$. For a pulsed source allowing arbitrary triggers with a maximum repetition rate f_{pulse} (corresponding to a minimum pulse delay $\Delta t_{\text{pulse}} = 1/f_{\text{pulse}}$), the number of points that can be addressed over one actuation cycle is

$$N_{\max} = \lfloor \frac{f_{\text{pulse}}}{f_{\text{scan}}} \rfloor \tag{4.1}$$

For addressing purposes, it must be noted that pulses spaced equally in time will result in addressed points having varying axial spacing as a consequence of the sinusoidal scan, which has non-uniform velocity. Assuming the addressed area is contained between positions $-L/2$ and $L/2$, a pulse emitted at time t will hit point $x(t) = \frac{L}{2}\cos(2\pi f_{\text{scan}} t)$, with the time origin chosen so that the MEMS motion has zero phase. Consequently, addressing a point at position x requires a pulse emitted at time $t(x) = \arccos(2x/L)/2\pi f_{\text{scan}}$[1].

To address N equally spaced points, with positions x_k such that

$$x_k = -\frac{L}{2} + \frac{L}{N-1}k \quad k \in [\![0, N-1]\!] \tag{4.2}$$

pulses must be emitted with corresponding timings $t_k = \arccos(2x_k/L)/2\pi f_{\text{scan}}$. From this, the pulse spacing can be calculated :

$$\Delta t_k = t_{k+1} - t_k = \frac{T_{\text{add}}}{\pi}(\arccos(-1 + \frac{2(k+1)}{N-1}) - \arccos(-1 + \frac{2k}{N-1})), \quad k \in [\![0, N-2]\!] \tag{4.3}$$

However, in this configuration, the edge points can only be addressed once per actu-

[1] The pulse timings calculated here are given modulo $1/f_{\text{scan}}$. In the following, we assume $t \in [0, 1/f_{\text{scan}}[$ for concision, corresponding to a double scan of the addressed length.

ation cycle, while the inner points can be addressed twice. A more optimal addressing method can be achieved by distributing the points along a portion of the scanned length to ensure that each point can be addressed twice per scan cycle.

If the addressed points are restricted to a length L_{eff}, that is

$$x_k = -\frac{L_{\text{eff}}}{2} + \frac{L_{\text{eff}}}{N-1}k \quad k \in [\![0, N-1]\!] \tag{4.4}$$

then the addressing pulse timings become

$$t_k = \frac{\arccos(2x_k/L_{\text{eff}})}{2\pi f_{\text{scan}}} \quad \text{and} \quad t'_k = \frac{2\pi - \arccos(2x_k/L_{\text{eff}})}{2\pi f_{\text{scan}}} \tag{4.5}$$

We must choose L_{eff} such that $t'_{N-1} - t_{N-1} \geq \Delta t_{\text{pulse}}$. From this we can calculate the maximum possible value of L_{eff}:

$$L_{\text{eff,max}} = L\cos(2\pi f_{\text{scan}}\frac{\Delta t_{\text{pulse}}}{2}) \tag{4.6}$$

and the maximum number of addressable points N depends on the minimal pulse delay: $\Delta t_{\text{kmin}} = t_{\text{kmin+1}} - t_{\text{kmin}} \geq \Delta t_{\text{pulse}}$. From the slope variations of the arccosine function, we can infer that $k_{min} = \lfloor \frac{N-2}{2} \rfloor$, and calculate the values of Δt_{kmin} :

$$\begin{aligned} \Delta t_{\text{kmin}} &= \tfrac{2}{2\pi f_{\text{scan}}} \arcsin(\tfrac{L_{\text{eff}}}{L\times(N-1)}) \text{ for } N \text{ even} \\ \Delta t_{\text{kmin}} &= \tfrac{1}{2\pi f_{\text{scan}}} \arcsin(\tfrac{L_{\text{eff}}}{2L\times(N-1)}) \text{ for } N \text{ odd} \end{aligned} \tag{4.7}$$

We can then obtain the maximum value of N as a function of Δt_{pulse} and L_{eff}

$$\begin{aligned} N &< \tfrac{L_{\text{eff}}}{L\sin(\pi f_{\text{scan}}\Delta t_{\text{pulse}})} + 1 \text{ , } N \text{ even} \\ N &< \tfrac{2L_{\text{eff}}}{L\sin(2\pi f_{\text{scan}}\Delta t_{\text{pulse}})} + 1 \text{ , } N \text{ odd} \end{aligned} \tag{4.8}$$

and if we choose $L_{\text{eff}} = L_{\text{eff,max}}$, we have finally

$$\begin{aligned} N &< \tfrac{\cos(2\pi f_{\text{scan}}\Delta t_{\text{pulse}})}{\sin(\pi f_{\text{scan}}\Delta t_{\text{pulse}})} + 1 \quad \text{, } N \text{ even} \\ N &< 2\tfrac{\cos(2\pi f_{\text{scan}}\Delta t_{\text{pulse}})}{\sin(2\pi f_{\text{scan}}\Delta t_{\text{pulse}})} + 1 \quad \text{, } N \text{ odd} \end{aligned} \tag{4.9}$$

the limits for N even and odd are typically within 1% of each other and close enough that their integer floors are equal, such that the parity of N does not matter.

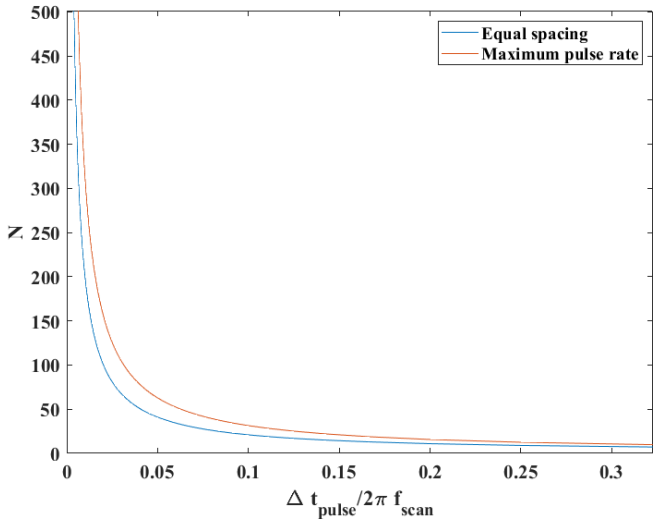

Figure 4.2: Maximum number of addressable points for increasing values of Δt_{pulse}. The maximum pulse rate does not take into account synchronization over both scan directions.

Furthermore, the equal spacing configuration implies a lower number of points than the maximum repetition rate configuration, with a ratio

$$\frac{2N_{\text{odd}}}{(\Delta t_{\text{pulse}} f_{\text{scan}})^{-1}} = 4\Delta t_{\text{pulse}} f_{\text{scan}} (\cot(2\pi f_{\text{scan}} \Delta t_{\text{pulse}}) + 1) > \frac{2}{\pi} \tag{4.10}$$

Fig. 4.2 shows the evolution of the maximal values of N as a function of Δt_{pulse}.

The choice of N also affects the optical design of the addressing setup: the addressing pulses must be focused enough to avoid any overlap with neighboring points. For pulses with diameter D at the addressing plane, the addressed length to pulse diameter ratio ρ_{add} must be such that

$$\rho_{\text{add}} = \frac{L_{\text{eff}}}{D} \geq N - 1 \tag{4.11}$$

For a MEMS scanner actuated at a frequency $f_{\text{scan}} = 335$ kHz, with a minimum pulse delay $\Delta t_{\text{pulse}} = 100$ ns (corresponding to the 10 MHz repetition rate of the pulsed source used), we have $L_{\text{eff,max}}/L = 0.978$ and $N_{\text{max}} = 10$, corresponding to 20 addressing pulses per cycle. In these conditions, we have $\Delta t_{\text{kmin}} = 103.5$ ns.

Pulse duration is also a critical factor of addressing performance, as longer pulses will induce smearing at the addressing plane, as the incoming pulse is reflected off the

moving scanner. If a pulse with duration τ_{pulse} is emitted so that it is centered around the addressed target – that is, between $t_k - \tau_{\text{pulse}}/2$ and $t_k + \tau_{\text{pulse}}/2$ – the induced smear will be

$$\begin{aligned} \Delta x &= (L/2)|\cos(2\pi f_{\text{scan}}(t_k + \tau_{\text{pulse}}/2)) - \cos(2\pi f_{\text{scan}}(t_k - \tau_{\text{pulse}}/2))| \\ &= (L/2)|2\sin(2\pi f_{\text{scan}} t_k)\sin(2\pi f_{\text{scan}}\tau_{\text{pulse}}/2)| \\ &\leq L\sin(2\pi f_{\text{scan}}\tau_{\text{pulse}}/2) \end{aligned} \tag{4.12}$$

For a pulse duration of $\tau_{\text{pulse}} = 6$ ns, the worst case smear length is then $\Delta x_{\max} = 0.0063L = 0.0065L_{\text{eff}}$. When taking in account pulse smearing, the addressed length to pulse diameter ratio condition becomes

$$\rho_{\text{add}} = \frac{L_{\text{eff}}}{D + \Delta x_{\max}} \geq N - 1 \tag{4.13}$$

with the parameters above, assuming a beam diameter $D = 5$ µm at the addressing plane requires a minimal effective addressed length $L_{\text{eff}} \geq D/(\frac{1}{N-1} - \frac{\Delta x_{\max}}{L_{\text{eff}}})$, which translate to a full scanline length $L \geq 48.9$ µm. This is equivalent to a scanner with a 2° optical angular range placed 1.4 mm away from the addressing plane. Of course, bringing a MEMS scanner this close to the target would be impractical for the placement of optical elements, but this calculation shows that a sufficient ρ_{add} can be achieved easily with low scan angles.

4.1.3 Optical setup

The detector used is a FLIR GS3-U3-32S4M-C camera, with a 2048×1536 pixel detector with 3.45×3.45 µm^2 pixel size. The data connection speed limits the live frame rate to roughly 10 frames per second; consequently, at the chosen actuation frequency, recorded images are the sum of several thousands of pulsing cycles.

The pulsed diode laser can be driven either at multiples of the scanner frequency, addressing fixed points whose position depends on the relative phase of the laser and scanner driving signals, or at any arbitrary high frequency (that is not an integer multiple of the scanner frequency), producing a continuous scan line after temporal inte-

gration by the camera, producing the same effect as continuous wave illumination as pulses are evenly distributed along the addressed line.

This demonstration setup focused on achieving high focusing power, thus reducing the spot size to a diameter comparable to that used in most experiments involving trapped atoms, typically a few microns [58,103,104]. While beam waists of this size can easily be produced with commercial optics, taking in consideration the small diameter of the MEMS scanners, and the limited numerical aperture achievable – as optics must be placed sufficiently far away from the MEMS chip in order to not obstruct the incoming and reflected beams – along with the spot size to scan length and beam quality requirements, one finds that the design of an adequate addressing setup is nontrivial. Field curvature stemming from beams at the target plane being nonparallel can, in particular, severely impact performance, as shown on Fig. 4.3.

Regarding the spot size to scan length ratio, several observations can be made. If one attempts to focus the beam onto the surface of the MEMS to minimize beam deformation from surface aberrations, the beam divergence and MEMS scan angle will have the same geometric center; in particular, focusing down the beam further in the system will also mean suppressing the MEMS scanning. In this case, the spot size to displacement ratio is related to the beam divergence to scan angle ratio :

$$\rho_{\text{add}} = \frac{L}{D} = \frac{\sin\theta_{\text{MEMS}}}{\sin\theta_{\text{beam}}} \tag{4.14}$$

if we consider a geometric beam diverging from the location of the scanner, the scan angle and divergence angle both having the same geometric origin. The right side of this equation is an invariant for any optics placed after the scanner, as any magnification or reduction of either angle will similarly affect the other. The divergence θ_{beam} is determined by the effective numerical aperture of the focusing optics used to bring the beam onto the scanner; a lower divergence will allow for higher values of ρ_{add}, but also implies weaker focusing onto the scanner. Assuming a maximum admissible beam size of $d_{MEMS} = 150$ µm on the scanner, the corresponding minimum numerical aperture is

$$NA_{\text{min}} = \frac{\lambda}{2d_{\text{MEMS}}} = 0.0016 \tag{4.15}$$

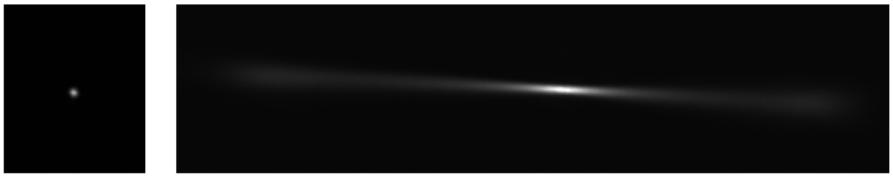

Figure 4.3: Example of beam distortion from a diverging scanline at the target plane, from an early version of the addressing setup. The beam has a waist of 38 µm with the MEMS scanner at rest (left). Scanning produces a 1.89 mm wide scanline, but deforms the beam to a waist of approximately 175 µm at the edges of the scanline (right). These images were obtained using a Thorlabs DCC1545M CMOS camera

which will simply ensure a small enough diffraction limit. If we consider a focused Gaussian beam, and a well collimated incoming beam (the optical fiber coupler used specifies a divergence of approximately .06°at 488 nm), with a diameter d_{beam} of 1.35 mm, corresponding to what was measured after the fiber coupler, the focal length f_{MEMS} of the focusing lens needed to achieve this numerical aperture NA_{min} is $f_{\text{MEMS}} = \pi d_{\text{beam}} d_{\text{MEMS}}/(4\lambda) \leq 326$ mm. Now considering the scan length to spot size ratio, at a distance $z_R = 145$ mm from the scanner, roughly equal to the Rayleigh length of a Gaussian beam with waist d_{MEMS}, for an optical scan angle of $\theta_{\text{opt}} = 2°$, we have

$$\rho_{\text{add}} \approx \frac{z_R \theta_{\text{opt}}}{\sqrt{2} d_{\text{MEMS}}} = 23.8 \tag{4.16}$$

While this is in line with our first estimation of $\rho_{\text{add}} = 20$, several issues remain unaddressed with this optical configuration. We have mentioned that low divergence is preferable to optimize the ratio ρ_{add}. Using a 325 mm focal length lens for diffraction-limited focusing is impractical, requiring long distances and likely to degrade beam quality from spherical aberration (for a plano-convex lens) or other variations in alignment and incoming beam shape. Furthermore, scanning will result in beam deformation at the target plane for maximal deflection angles. This is especially true if one wishes to focus the scanned beams on a small target, requiring focusing optics with high numerical aperture exacerbating the curvature of the scan line. Fig. 4.3 shows an example of how a diverging scan line can dramatically impact beam performance.

A more favourable approach requires ensuring beam focusing and scanning angles

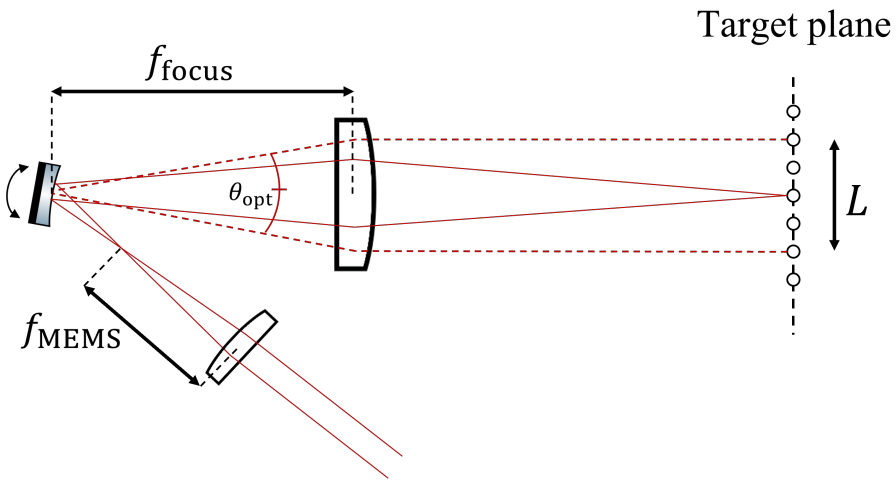

Figure 4.4: Diagram illustrating the telecentric beams approach. The scanner is placed in the object plane of the final focusing lens, allowing the scanned beams to travel parallel while being focused onto the target plane.

could be controlled separately, and allow minimization of both the spherical deformation and the spot size at the target plane. This was achieved by placing the MEMS scanners slightly off from the focal point of the initial focusing optics, while making sure that the incident beam still fit onto the mirror plate, as illustrated on Fig. 4.4. Consequently, having the scanned beams in a telecentric configuration – that is, ensuring the angled beams travel parallel to each other – can be done while focusing the beam itself on the target, therefore enhancing the displacement to spot size ratio and allowing the use of diffraction-limited target sizes; conversely, the beam can travel collimated between relay optics while the scan line is focused, reducing the aperture needed within the system for well-chosen optics.

In this configuration, the ratio ρ_{add} depends on the resolving power and aperture of the final optics focusing the beams on the target. Assuming a final focusing objective with focal length f_{focus}, with the scanner (or an image of the scanner) placed in its object plane, with the beam collimated to a diameter d_{focus}, the beam will be focused down to a waist w_{target} such that

$$w_{\text{target}} \approx \frac{2\lambda f_{\text{focus}}}{\pi d_{\text{focus}}} \tag{4.17}$$

corresponding to a beam width $d_{\text{target}} = 2w_{\text{target}}$. Taking, for a first estimation of these values, a beam diameter $d_{\text{focus}} = \sqrt{2}d_{\text{MEMS}}$ and $f_{\text{focus}} = 7.5$ mm (one of the shortest values available for commercial achromats), we get $d_{\text{target}} = 22$ µm at $\lambda = 488$ nm. With the same parameters, the scan length for $\theta_{\text{opt}} = 2°$ is

$$L \approx \theta_{\text{opt}} f_{\text{focus}} = 261 \text{ µm} \tag{4.18}$$

for a final scan length to point size ratio $\rho_{\text{add}} = 11.9$. This is half of the value expected with the beam focused on the MEMS; however, this ratio can be improved by further refining the optical design (see below) while retaining the inherent advantage of separating scan line focusing from beam focusing.

4.1.4 Ray-tracing simulation

In order to construct and validate an optical design that implements the principle described above, a ray-tracing simulation was performed using OpTaliX to take into account the lens specifications of off-the-shelf parts and to evaluate system performance. The final simulated layout is pictured on Fig. 4.5. It involves a pair of 30 mm achromatic lens used to image the MEMS onto the focal plane of the focusing lens, to avoid the difficulty of aligning a short focal length in very close proximity to the MEMS mirror. The simulation is run with the assumption of a perfectly collimated incoming beam with diameter 1 mm, focused by a 150 mm focal length achromatic doublet (Thorlabs AC254-150-A), resulting in a focused beam diameter $d_1 = 93$ µm. If we place the MEMS at a distance $z_M = 35$ mm away from the focal point, we then have

$$d_{\text{MEMS}} = d_1 \sqrt{1 + \left(\frac{z_M \lambda}{\pi (d_1/2)^2} \right)^2} = 252 \text{ µm} \tag{4.19}$$

This would be too wide to fit on a 200 µm diameter mirror, but could be fit on a 400 µm diameter mirror. This value of z_M is sufficient to allow practical and independent control of beam and scanline focusing. After being reflected on the MEMS scanner, the beam is realigned by a silver mirror and transmitted through a pair of 30 mm achromatic lenses (Thorlabs AC-127-030-A) in a "4f" configuration, and to the final

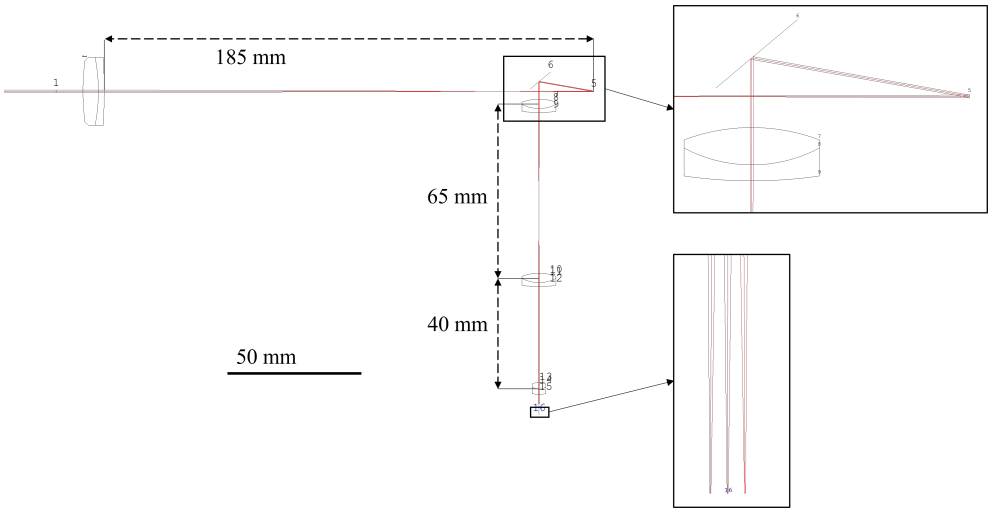

Figure 4.5: Optical layout as simulated in OpTaliX. The scanner is the element n. 5, the element n. 6 being a silver mirror to realign the optical axis with table axes for practical alignment. Lens surface data was obtained from the manufacturer [196].

focusing lens. The MEMS is placed in the object plane of the lens pair, so that it is imaged onto the object plane of the focusing lens – a 7.5 mm focal length achromatic lens (Thorlabs AC050-008-A-ML) was used for the simulation. In this configuration, the distance between each lens of the pair is adjusted so that the angled beams are collimated and overlap at the object plane of the focusing lens, resulting in an effective separation slightly larger than 60 mm. It follows that in the image plane of the focusing lens, the beams are focused and run parallel. The beam size on target is therefore equal to the value d_{target} calculated above.

As shown on Fig. 4.6, beams deviated by the scanner movement do not show any significant deformation once focused at the target plane, ensuring consistent spot size along the scanned line. The deformation remains within acceptable limits even for large scan angles (see section 4.2). This setup also has the advantage of being easily aligned and adjusted by hand, as lens distances are conditioned by collimation of the beam or the scanline which can easily be ensured during assembly. In practice, the placement of the MEMS relative to the initial focusing lens is the element subject to the largest imprecision, but this can be corrected further down the optical path.

To further improve performance, the final focusing lens was changed from the 7.5

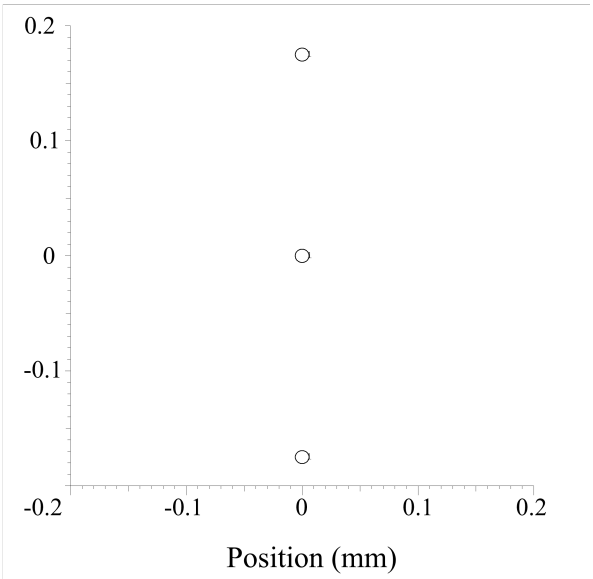

Figure 4.6: Spot shapes at the target plane, for the simulated setup with -1°, 0°, and +1° angles on the MEMS scanner. The circles represent the spatial extent of the rays as simulated by OpTaliX.

mm achromat used in the simulation to a microscope objective with 40x magnification and 0.5 numerical aperture. In order to make use of the full numerical aperture of that objective, the second 30 mm lens was swapped for a 125 mm lens (Thorlabs AC254-125-A), enlarging the beam to approximately 1 mm in diameter on the back aperture of the microscope objective. Further simulations showed that these changes result in a FWHM spot size of $d_{\text{target}} \approx 2$ µm, roughly twice the diffraction limit for an objective with 0.5 numerical aperture. This is a consequence of underfilling of the objective back aperture, leading to a lower effective numerical aperture.

Figure 4.7 shows the layout of the optical elements after the scanner. In this configuration, the scan length L at the target plane, i.e. the microscope objective sample plane, is equal to $L = \theta'_{\text{opt}} f'_{\text{focus}}$; θ'_{opt} is the optical scan angle seen after the 4f lens pair, and f'_{focus} is the back focal length of the microscope objective. In first approximation, we take the back focal length to be equal to the object plane focal length. For a $M = 40$ magnification objective with a reference focal length of $l_r = 160$ mm, this gives

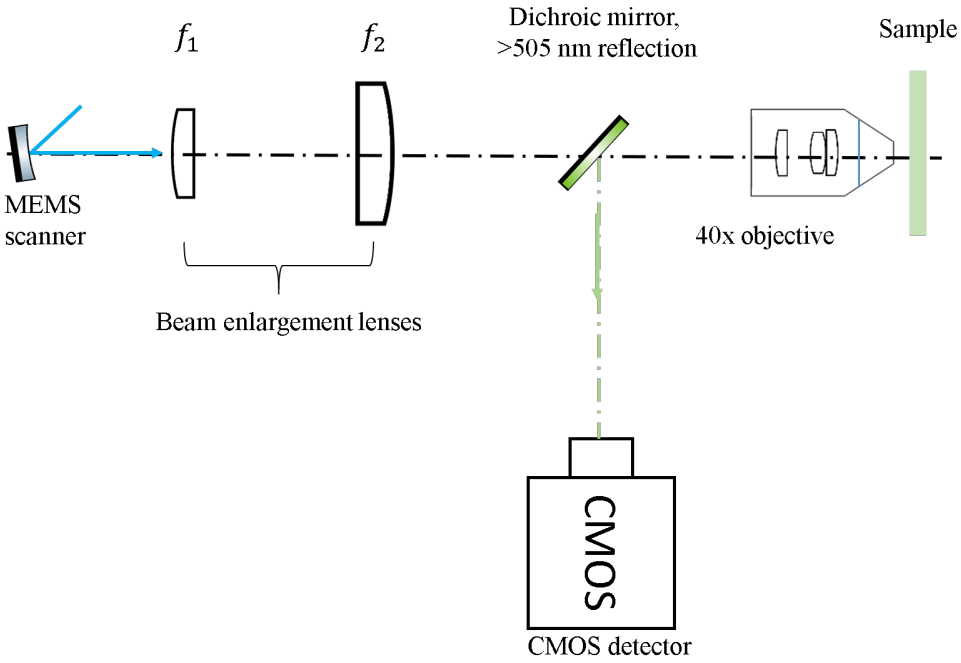

Figure 4.7: Schematic layout of the fluorescing target setup. Not to scale.

$f'_{\text{focus}} = l_r/M = 4$ mm. Furthermore, in the 4f configuration, we have

$$\theta'_{\text{opt}} \approx \frac{\theta_{\text{opt}} f_1}{f_2} \tag{4.20}$$

With the values specified above, we then find $L = 33.5$ µm, which corresponds to $\rho_{\text{add}} = 16.8$. This is a significant improvement both in the target size, and the scan length to spot size ratio. Most importantly, as was mentioned before, a spot size in the micrometer range is in line with common ion trapping experiments [58, 103, 104].

4.2 Experimental results

Beam focusing In order to confirm the optical performance of the system, the incoming beam was observed at the target plane through a 20x microscope objective. The beam waist at focus was measured to be under 5 µm (D4σ diameter), with a Gaussian profile mostly free of aberrations. An image of the beam is shown on Fig. 4.8. This corresponds to a FWHM of 2.9 µm, close to the simulated value of 2 µm.

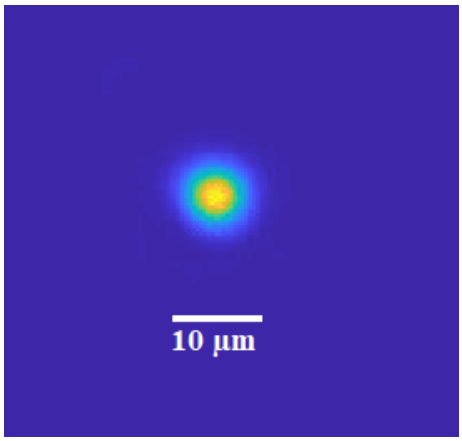

Figure 4.8: Image of the focused laser spot at the image plane. This image was obtained through a 20x microscope objective focused onto the target plane and observing the incoming beam without a sample.

Measurements with MEMS scanning show that a scanner actuated with a single actuator at 20 Vpp can scan a length of 143 µm at resonance, giving an effective scan length to spot size ratio of $\rho_{\text{add,eff}} = 29$, comfortably higher than the ratio of 13.9 expected from the simulation, likely because of deflection angles higher than 1° produced by the scanner. With the values of the simulation, this ratio corresponds to a total optical scan angle of 4.2°.

Demonstration targets and imaging A concrete demonstration of the addressing system requires the use of actual targets to show the system's ability to address a given structure. Since this system was only intended as a proof of concept, including an actual ion trap for demonstration would be too complex; however, the addressing performance can still be demonstrated and quantified by using a substitute of corresponding scale.

The chosen targets must satisfy certain requirements. It is important that the measured signal produced by the target is an accurate representation of the system's performance, and not limited by the target's size or response time. Furthermore, for targets producing an optical signal when addressed, that signal must be distinguishable from the incoming addressing signal, from a detection standpoint, either by filtering the addressing signal after it hits the target, or by having a separate optical path for the measured signal. In the following, the targets used exhibit a fluorescence peak above

500 nm, conveniently allowing filtering of the 488 nm laser light by a 500 nm long pass filter (Thorlabs FEL 0500).

In order to ensure proper imaging, the target used must have a thickness shorter or equal to the depth of field of the objectives used. The depth of field for a 40x objective with 0.65 numerical aperture, and a detector with 3.45 µm resolution, is approximately 1.5 µm [197]. A sufficiently thin layer of fluorescing material can be obtained simply by placing a small amount of fluorescing solution between two glass slips, or by depositing it on the surface of a glass slide and allowing the solvent to dry, leaving only the nanobeads that adhered to the glass surface. However, the latter method may result in uneven material deposition leading to a degraded signal.

To obtain a target with homogeneous deposition of fluorescing material, samples were prepared using APTMS (3-amino-propyltrimethoxysilane) to bond fluorescein salt in a single layer onto a glass slide. The preparation protocol was adapted from [198]. Again, the emission properties of fluorescein make it suitable for filtering of the addressing light with a 500 nm longpass filter [199].

A consequence of using a thin sample is a dramatic reduction of fluorescence intensity. Detecting the emitted signal requires setting the CMOS detector to high exposure and gain values, leading to increased optical and electronic noise thresholds. Furthermore, it is difficult to filter transmitted laser light enough that it does not affect significantly the fluorescence reading. Measurements show that even using two 500 nm longpass filters in succession, resulting in an absorbance value of approximately 9, is not sufficient to eliminate transmitted light. In order to mitigate this issue, we modified the setup by placing a 505 nm cutoff dichroic mirror (Thorlabs DMSP505T) between lens f_2 and the focusing microscope objective, at a 45°angle. The longer wavelength fluorescence, emitted through the microscope objective in the direction opposite to the propagation of the addressing laser, is then deflected by the mirror and focused onto the detector using a 150 mm focal length achromat, roughly matching the reference focal length of the focusing objective, now also acting as an imaging objective. A longpass filter was still necessary after the dichroic mirror to eliminate the laser light reflected by the sample slide glass surface.

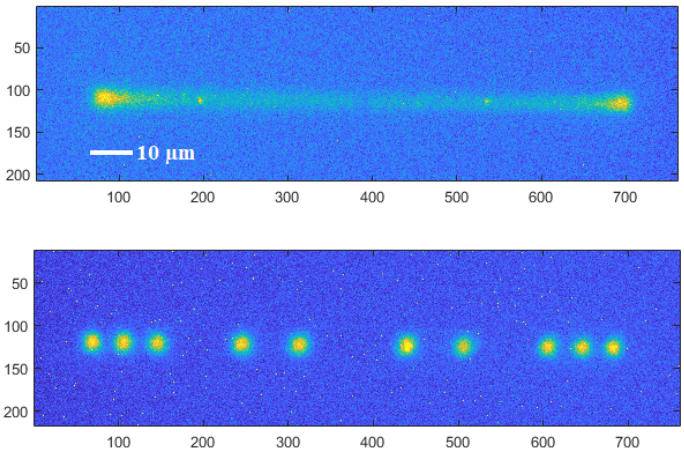

Figure 4.9: Top: Fluorescence from a continuous scan of the sample at 87.4 kHz. Bottom: same scan with a pulse repetition rate of 874 kHz.

This configuration also presents the advantage of using a single microscope objective both for target illumination and imaging, simplifying alignment of the sample and detector. An imaging magnification of 34x was achieved this way, sufficient to achieve diffraction-limited imaging.

Fig. 4.9 shows the result of a one dimensional scan on the fluorescein coated target. The fluorescence spots observed when pulsing the laser at multiples of the scanner frequency of 87.4 kHz have a D4σ diameter of 6.4 µm, which is in line with the focused beam waist when accounting for increased fluorescence scattering at high power density. Pulses near the edges of the scanline exhibit negligible distortion, indicating no divergence of the scanning beam trajectories, and negligible smearing from the scanning motion. The total scanned length is 123 µm, roughly 19 times the width of a single florescence spot.

The sinusoidal motion of the scanner affects the power distribution along the scanline, with more power being concentrated near the edges, where the instantaneous angular velocity of the scanner decreases. For discrete pulses, this translates into an uneven spatial distribution for pulses emitted at a fixed frequency. This effect underlines the necessity for a source capable of emitting arbitrary sequence of pulses, as discussed in section 4.1.

4.3 Summary

These results have demonstrated how the system can be used to address small targets while making full use of the MEMS scanner's capabilities. An optical setup for one-dimensional addressing was designed and optimized through gaussian beam optics calculations and ray-tracing simulation, resulting in a predicted spot diameter $d_{\text{target}} \approx 2$ µm and a scan length to spot diameter ratio $\rho_{\text{add}} = L/d_{\text{target}} = 16.8$. Laser source seed was also discussed, showing that a pulsed source with a 10 MHz repetition rate is enough to address 10 equally spaced points at 335 kHz.

The design was then assembled and evaluated experimentally. Using thin fluorescing samples and large scanner deflection angles produced a scan length to spot diameter ratio of $\rho_{\text{add}} = 19$ with a spot diameter of $d_{\text{target}} = 6.4$ µm. This configuration also satisfied the requirement for low aberrations at the edge of the scan line, with no distortion of the outermost spots observed.

The system's performance is adequate for targets that are of similar sizes to atomic particle traps, and consists only of commercially available optics in addition to the scanners. The final setup has a relatively small footprint, contained within a volume of 45x45x20 cm, making it easy to displace and integrate into more complex macro-scale systems. The main limitation of the scanning system remains the resonant actuation of the scanner, imposing strict constraints on the addressing frequency and making synchronization with other short-timescale systems more difficult; this will be the case when using a pair of scanners in conjunction for a two-dimensional addressing system.

Chapter 5

Towards a small-scale quantum control system: 2D addressing

5.1 The synchronization problem: Lissajous scanning and other schemes

For a variety of applications, the ability to scan a point in a 2D space is of much greater interest than the single-axis scanning discussed so far. These include tracking systems and optical sensors for example to detect targets in a two dimensional (spherical) range. In general, two dimensional scanning is a core feature of display scanner applications [40, 128, 137, 200, 201]. While necessary to draw images, it can also greatly extend the capacity of an addressing system by increasing its spatial range. Regarding atom traps, two-dimensional arrays of trapped particles can be formed from optical lattices organising trapping locations in regular 2D grids (see chapter 2).

Although the general principles exposed in the following section apply to any kind of optical scanners, most of the discussion is in the context of utilizing MEMS scanners to generate 2D scanning. A crucial issue to solve in order to construct such a system is to design an addressing scheme that covers a two-dimensional range with MEMS devices producing one-dimensional movement. Indeed, while it was shown that the MEMS micromirrors could produce movement along either of the in-plane axes, these motions correspond to separate resonant modes with highly different resonances so that achiev-

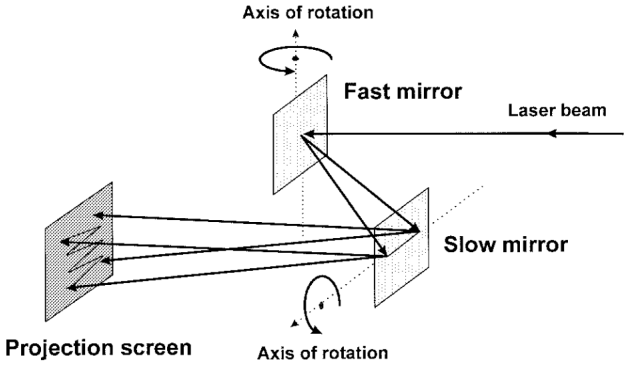

Figure 5.1: Illustration of raster scanning using using a fast-axis and a slow axis mirror. Reproduced from [36] with permission, ©1999 IEEE.

ing 2D movement using a single MEMS micromirror with sufficient control is highly unlikely. Two micromirrors must then be used, each addressing one of two perpendicular, or at least nonparallel, axes. 2D addressing can then be achieved by reflecting light consecutively on both mirrors. Moreover, additional control is required as we desire to address some arbitrary points and not the whole space; this requires synchronization between the motion of each mirror, and the driving of the light sources. To this end three different control schemes were compared in the following: slow axis/fast axis scanning, single frequency scanning, and Lissajous scanning.

Two dimensional scanning with a slow axis and a fast axis is the most widespread for displays [35]. It uses either two mirrors, one with resonant and one with quasi-static motion, or one mirror simultaneously driven along two perpendicular axes, to perform a raster scan of the target space. This requires the fast axis frequency to be a multiple of the slow axis frequency to ensure consistent addressing of the target space. The higher the fast axis to slow axis frequency ratio, the more lines in the raster scan, allowing for higher resolution. Scan repetition rate, or frame rate, is equal to the slow axis frequency. The principle of raster scanning is illustrated on Fig. 5.1. The devices used for single-scanner raster scanning, however, usually operate with slow axis frequencies in the sub kHz range [155, 200, 202] which would be insufficient for addressing at the short timescale of atom physics and quantum optics.

Given that the devices presented in chapter 3 are identical, with very similar ac-

tuation frequencies, a raster scan setup cannot be used: considering resonant modes, the highest frequency mode of the device (around 405 kHz for the 200 µm diameter scanner) is only about 2.5 times that of the slowest mode (173 kHz). Consequently, the possibility for scanning using the same actuation frequency on both axes is examined. In other words, we discuss the case where two 1D scanners having identical resonance frequencies and scanning modes are utilized.

The principle of this single frequency scanning approach is to navigate the target space along ellipses instead of lines. The ellipses follow the parametric equations

$$\begin{cases} x(t) &= \cos(2\pi f t) \\ y(t) &= \sin(2\pi f t + \phi) \end{cases} \qquad \phi \in [0, 2\pi], t > 0 \tag{5.1}$$

assuming both mirrors have the same normalized displacement amplitude, with no modulation of said amplitude. Controlling the phase ϕ changes the ellipticity parameter of the traced curve, and thus the addressed points. A grid of points can thus be addressed by successive changes in the phase delay between the actuation signal of each mirror, in a pattern illustrated on Fig. 5.2

While this allows for 2D addressing of arbitrary points, addressing a square grid of equally spaced points requires a number of ellipses proportional to the grid side length squared (that is, the number of points in the grid) [1], while raster scanning only requires a number of lines proportional to the side length. This is important as shifting the phase delay to move from one ellipse to another has a significant time cost, affecting overall operation speed.

Preliminary measurements, using different methods for inducing a phase shift in the actuation signal – instant phase jumps in actuation signal, fast phase modulation, with or without added amplitude modulation – showed that applying a phase shift to the mirror movement demands an exceedingly long time (several milliseconds), accompanied with a significant loss in amplitude during the transition when using resonant actuation – the mechanical energy stored in the device is lost and must be built up again as a result

[1] It can be shown rather intuitively that, allowing displacement amplitude to exceed the grid length so that a circle covers eight grid points, the number of ellipses necessary to cover a grid of $N \times N$ points is $(\frac{N}{2})^2 - \frac{N}{2} + 1$ for N even, and $(\frac{N-1}{2})^2 + 1$ for N odd.

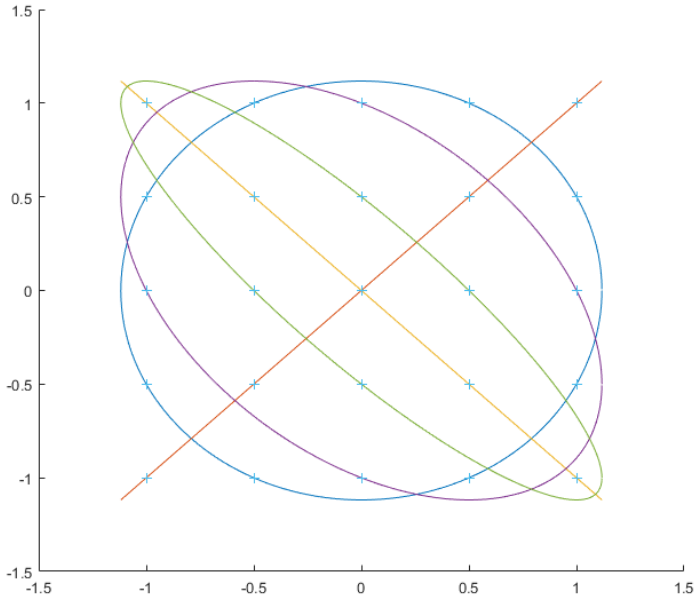

Figure 5.2: Example of an ellipse pattern to address a rectangular grid.

of the phase transition. Consequently, this approach to synchronization is incompatible with high operation frequencies.

Moreover, the discrepancies in resonance frequencies between fabricated chips with identical scanner designs, along with the narrow frequency width of resonant modes, make it difficult to find pairs of devices that can be actuated at the same frequency with similar amplitude (see section 3.3.4). As discussed earlier, frequency tuning can be used to mitigate this issue (see section 3.4), but the long timescales required for phase shifts make synchronized actuation unattractive for high speed applications. This observation led to the development of an original 2D addressing method using close, but distinct actuation frequencies on each axis.

Parametric curves following sinusoidal equations for each (cartesian) coordinate in two dimensions are a family known as Lissajous curve, that is, curves of the form

$$\begin{cases} x(t) &= A\cos(2\pi f_1 t) \\ y(t) &= B\sin(2\pi f_2 t + \phi) \end{cases} \tag{5.2}$$

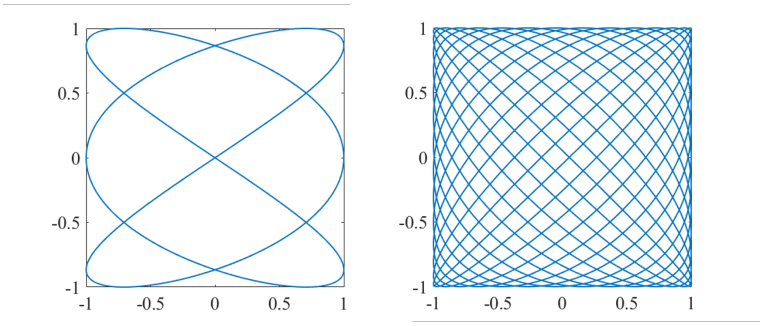

Figure 5.3: Left: Lissajous curve for $f_1 = 6$ and $f_2 = 9$. Right: Lissajous curve for $f_1 = 90$ and $f_2 = 87$, with $\phi = 0$.

For $f_1 = f_2$, this is the equation of ellipses used above (Eq. 5.1). For $f_1 \neq f_2$, the curve exhibits a number of crossing points (see Fig. 5.3).

The number and position of crossing points depends on the ratio between each axis frequency, and the scan frequency which is equal to the greater common divisor (GCD) of both. As this ratio increases, the density of points increases, forming a grid-like pattern in the center of the addressed area. This is shown in Fig. 5.4.

The detailed mathematical derivation of the position and corresponding phase of the crossing points can be found in appendix B. These crossing points are valuable for an addressing setup as they can be visited up to four times during each actuation cycle; consequently, addressing a grid of points aligned with crossing points would allow for a single-point operation rates equal to four times the cycle frequency. Higher cycle frequencies give higher operation rates at the cost of reduced point density and increased grid distortion. Since the devices used have similar resonance frequencies, low cycle frequency to axis frequency ratios can be expected, with the cycle (Lissajous) frequency being roughly 10 to 50 times lower than the axial frequencies. It should also be noted that only the central part of the scanned space, where grid distortion remains low, can be addressed; depending on the precision needed for the setup, the available area can be as low as 25% of the total addressed area. Overall, the Lissajous scan is a faster and more consistent addressing scheme than single frequency scanning, at the cost of reduced range.

Lissajous scanning is also more suited to addressing a large number of different points

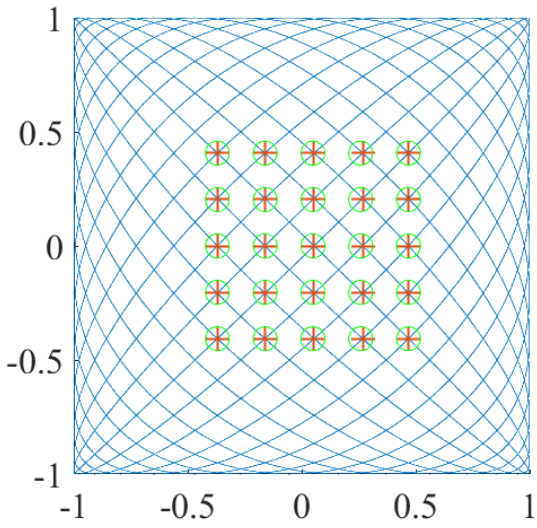

Figure 5.4: Lissajous curve for $f_1 = 90$ and $f_2 = 87$, with $\phi = 0$. Crosses indicate the Lissajous pattern crossing points used for grid addressing, circles form a perfectly rectangular grid aligned with the corners of the 5x5 grid for comparison.

in sequence rather than hitting the same point with consecutive pulses; for points at the center of the pattern, similar to raster scanning, the path followed by the Lissajous scan goes through every addressed point before coming back to its starting position.

This method of scanning imposes stricter timing requirements in order to minimize blur. While the maximum spot velocity for one dimensional addressing was $v_{max,1D} = 2\pi f L$ m.s^{-1}, the same expression for 2D Lissajous scanning gives $v_{max,2D} = 2\pi\sqrt{f_1^2 + f_2^2}L$ m.s^{-1}, L being the characteristic length, in meters, of the space being addressed; for $f_1 \approx f_2$, that is an increase of 40% ($\sqrt{2} - 1$) in velocity. Spot size requirements will also vary depending on the Lissajous cycle frequency and the density of the addressing grid, to avoid overlap between neighboring points (see section 5.2.2).

In light of the above discussion, Lissajous scanning was chosen to be exclusively used for the 2D addressing demonstration. It offers numerous advantages over the other discussed schemes, the main one being looser requirements on actuation frequency: while raster and single-frequency scanning require perfect matching of axis frequencies, Lissajous scanning allows a compromise based on the cycle frequency. Since the same cycle frequency can be achieved for different values of axis frequencies, it is sufficient that

the effective resonant frequency of the device used is close enough to one of these values. Furthermore, a wide range of cycle frequencies can be used with satisfactory results, depending on the number of points to address, addressing rate, and grid distortion tolerance – see below.

5.2 Design of a MEMS based 2D addressing system

Demonstrating 2D addressing requires an experimental setup allowing for synchronization of two MEMS mirrors with a pulse source, with the necessary beam shaping optics to ensure good performance in terms of optical resolution and spatial range. The design of this setup revolves around two main parts: beam shaping and electronic controls for synchronization.

5.2.1 Optical considerations

Constructing a 2D addressing system with one scanner for each axis requires some design work to ensure optimal system performance and footprint.

This work already highlighted the importance of synchronization and timing for the actuation and laser source electronics in relation to the addressed target. We will now consider the implementation of the MEMS scanners as optical elements.

The configuration used here is adapted from the 1D addressing setup described in section 4.2. The objective was to add a second MEMS scanner to this setup without changing the beam focusing strategy, and to keep the same optical elements to produce a similar performance. To achieve this, the first scanner was imaged onto the second one, so that the scan angles originate from the same point along the optical axis. In practice, this was done through a 100 mm focal length matched lens pair (Thorlabs MAP10100100-A) in a '1f-1f' configuration, with each scanner placed in the focal planes of the pair, on either side. This also ensures that the angled beams from the first scanner converge on the second one, and are not affected by scanner deformation.

The scanners are actuated using the same resonant mode, chosen based on frequency matching requirements (see section 5.1); one of the scanners is mounted with a 90° in

plane rotation relative to the other so that the scanlines are perpendicular to each other.

With this configuration, the image of the first scanner and the real second scanner are superimposed at one point of the optical axis and can be treated as one by the following optics. Regarding the separation of beam focusing and scanline focusing, the effect of the matched pair remains moderate: for a distance between beam focus and scanner of $\Delta f = 35$ mm, and approximating the lens pair as an ideal thin lens with a 50 mm focal length, we have the following expression for the scanner to focus separation after the lens pair, $\Delta f'$:

$$\Delta f' = \frac{f_{\text{PAIR}} \times \Delta f}{f_{\text{PAIR}} + \Delta f} = 20.6 \text{ mm} \tag{5.3}$$

which remains sufficient to ensure focused beams at the target plane with parallel scanlines. In practice, this change in optical properties can be compensated for when assembling the system, as the criteria for focusing the beams on target remain qualitative: the beam must be collimated after the 2f-2f pair, while the second MEMS image must be placed at the object plane of the final lens or objective.

The modified system is shown on Fig. 5.5. The scanners are placed with an identically low incidence angle, to minimize the beam distortion on the MEMS surface and ensure good positioning of the optical axis; except for the matched lens pair, all the optical elements can be placed parallel to the axes of an orthogonal coordinate system, facilitating assembly on an optical table. The parts used are the same as in chapter 4.

The alignment of the incoming beam onto the MEMS scanners was ensured by observing the image produced after the beam enlargement lenses. Once assembled and aligned, the effective magnification was first evaluated by placing a resolution test target (Thorlabs R2L1S4P) at the sample plane and comparing the size of the image to the known size of the target (see Fig. 5.6). This resulted in a magnification of approximately 17× using a 20× microscope objective; the discrepancy in effective magnification can be explained by a slight mismatch between objective tube length – 160 mm on an infinity corrected objective – and the 150 mm focal length achromat used to focus the objective image onto the detector. While the resolution of the system was enough to resolve even the smallest features available, we estimated system resolution by measuring edge blur

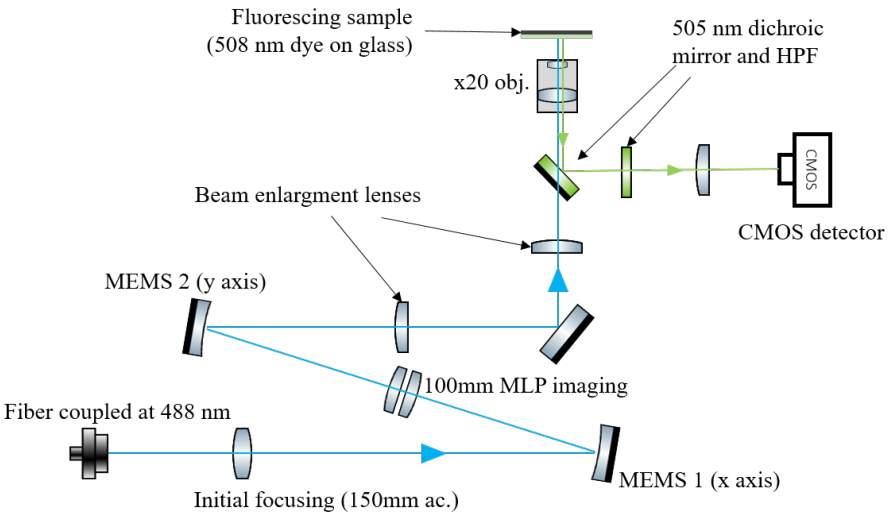

Figure 5.5: Schematic layout of the 2-axis scanning setup with a fluorescing target. Not to scale.

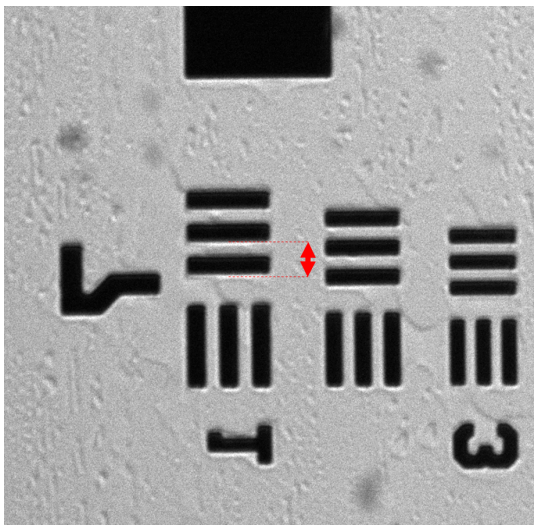

Figure 5.6: Image of the resolution test target seen through the imaging system. The red arrow occupies a length of 131.1 µm on the detector and has a real size of 7.8 µm, corresponding to a magnification of 16.8×

after applying a Sobel edge detection filter [203] to the detector image; the edge profile was then fitted to a Gaussian profile, giving an estimated resolution of 1.0 µm under white-light illumination. For comparison, the theoretical imaging resolution limit at 488 mm is $r_{min} = \lambda/2NA = 542$ nm for the objective used with a numerical aperture of 0.45.

5.2.2 Electronics and synchronized operation

A critical point for a practical realisation of this addressing scheme, beyond optical considerations, is synchronization between each of the MEMS actuation signal, and the pulse trigger signal. The results shown for the crossing points of the scanning pattern hold only with zero phase difference between each actuation signal, and precise control over addressing pulse timing is necessary to ensure proper positioning at the target space; the addressed point position depends entirely on the timing of the corresponding pulse. In this chapter, the synchronization was done experimentally using three identical signal generators (Agilent 33250A) for each of the input signals (MEMS 1, MEMS 2, pulse trigger). The signal generators were connected in a master-slave configuration, synchronized on the 10 MHz clock integrated to the pulse trigger generator. The phase delay between each signal could then be remotely controlled for each actuation generator using a GPIB interface. This setup required manual calibration of the phase compensation every time the addressing signal was started or modified, as the clock reference was reset and the phase delay was changed to an unknown value. For the demonstration setup, the calibration must be done by a human operator monitoring the position of the pulses received on the detector, knowing the expected pattern once the phases are properly calibrated; however, the process is simple enough that basic image recognition software could be used as feedback, and perform the calibration automatically.

Further iterations of a similar application can better solve the synchronisation problem by using dedicated synchronous actuation signal control with constant phase delays; the main sources of phase delay in the presented setup are asynchronous triggering of the actuation signals, variable phase between the actuation signal and the MEMS displacement, and signal propagation delay, all of which could be corrected by adapted

electronics. Phase feedback could also be obtained directly from the scanners by using one of the piezoactuators as a displacement sensor to obtain a voltage signal corresponding to the MEMS motion.

The startup and synchronization sequence for the demonstration system presented here was as follows :

- select the desired axial frequencies, then calculate the corresponding crossing point timings; this was done with a Matlab script implementing the results derived in appendix B.
- Enable scanner actuation and approach the desired axial frequencies from a lower starting frequency. This ensures that the resonant scanner is placed in the high amplitude branch of the hysteresis cycle. (see Fig. 3.14)
- Select the grid points to address and generate an arbitrary waveform containing pulses at the corresponding timings, then load this waveform into the laser diode trigger generator.
- Manually set the phase of the scanner actuation signals to ensure zero phase with the pulse driving signal. Subsequent changes in the addressed points requires setting the phase again.

Electronics and source speed Similarly to one-dimensional scanning, the choice of axial frequencies imposes requirements on pulse repetition rate to ensure that adjacent grid points can be addressed properly. As is shown in appendix B, the time coordinates of the crossing points are of the form

$$t = \frac{1}{2}(\pm\frac{k_1}{f_1} \pm \frac{k_2}{f_2}) \quad \text{or} \quad \frac{1}{2}(\pm\frac{k_1}{f_1} \pm \frac{k_2}{f_2}) + \frac{1}{4f_2}, \quad k_1, k_2 \in \mathbb{Z}^* \tag{5.4}$$

When addressing a grid pattern, one can derive from the results in appendix B that the minimal timing interval between two neighboring points on the grid is $\Delta t_{\min} = |\frac{1}{f_1} - \frac{1}{f_2}|/2$ when the curve does not wrap over, or $\Delta t_{\min} = |\frac{1}{f_1} - \frac{1}{f_2}|$ when it does. It is not surprising that denser patterns, which have closer axial frequencies, will require

higher pulse repetition rates to address concentrated crossing points. Therefore, frequency selection must be done according to the desired grid spacing, but also within the limitations of the pulse source.

Point spacing and spot size When addressing a two-dimensional grid with spacing parameters a and b, the diameter D of the pulses at the target plane must be small enough to avoid overlap between neighboring pulses (see Fig. 5.7), that is

$$D < \min(a, b) \tag{5.5}$$

For Lissajous scanning, the addressed grid will be affected by distortion as the crossing points get closer to each other near the edges of the scan pattern; however, the higher bound on the distance between two neighboring crossing points is a good approximation of the grid parameters :

$$\begin{aligned} a \lessapprox \Delta x_{\min} &= \tfrac{L}{2}\sin(2\pi f_1 \Delta t_{\min}) \\ \text{and similarly} \quad b \lessapprox \Delta y_{\min} &= \tfrac{L}{2}\sin(2\pi f_2 \Delta t_{\min}) \end{aligned} \tag{5.6}$$

where L is the total scanned length, supposed to be equal for both axes. The spot size condition becomes

$$D < \frac{L}{2}\sin(2\pi f_{\min}\Delta t_{\min}) \quad \text{with } f_{\min} = \min(f_1, f_2) \tag{5.7}$$

When taking in account pulse smearing, it is easy to calculate the effect of the pulse duration on the axial diameter at the target plane with the same expression as eq. 4.12 :

$$\Delta x \leq L\sin(2\pi f \tau_{\text{pulse}}/2) \tag{5.8}$$

where τ_{pulse} is the duration of the pulse and f is the axial frequency of either axis, Δx being the pulse smear along that axis. We then obtain the pulse size condition taking in account pulse smearing :

$$D < \frac{L}{2}(\sin(2\pi f_{\min}\Delta t_{\min}) - 2\sin(2\pi f_{\min}\tau_{\text{pulse}}/2)) \tag{5.9}$$

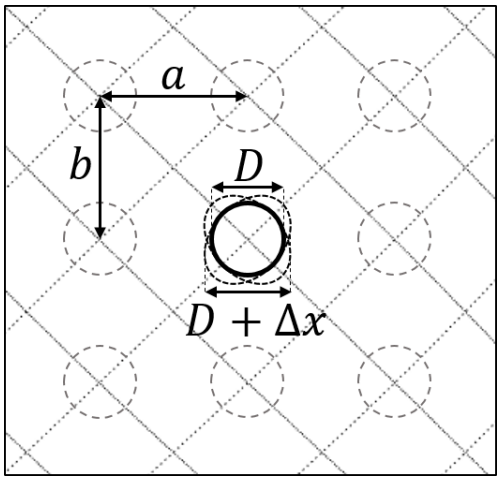

Figure 5.7: Illustration of the Lissajous addressing parameters on the central part of a Lissajous pattern with $f_1 = 90$ and $f_2 = 87$.

this condition can be expressed in terms of spot size to displacement ratio

$$\rho_{\text{add}} = \frac{L}{D + \Delta x_{\min}} > \frac{1}{\sin(2\pi f_{\min} \Delta t_{\min})/2 - \sin(2\pi f_{\min} \tau_{\text{pulse}}/2)} \tag{5.10}$$

Fig. 5.7 shows an illustration of the various pulse and Lissajous scan parameters. Overall, the choice of axial frequencies for Lissajous scanning is a compromise between grid distortion, point density, addressing speed, and grid size, and must be adapted to the requirements of the desired applications.

Table 5.1 lists these values for different pairs of axial frequencies corresponding to scanner resonance frequencies observed experimentally. We define the maximal grid distortion as the maximal distance between the Lissajous pattern crossing point and the corresponding rectangular grid point, for a 7 by 7 points grid whose corner points are aligned with the closest pattern crossing points. More precisely, if we consider a point whose expected coordinates on a regular rectangular grid are (x_i, y_j), and visited at time $t_{i,j}$ by the Lissajous scan, the distortion $d(i, j)$ for this point is

$$d(i,j) = \sqrt{(L\cos(2\pi f_1 t_{i,j}) - x_i)^2 + (L\sin(2\pi f_2 t_{i,j}) - y_j)^2} \tag{5.11}$$

These results show how the addressing parameters vary depending on the choice

f_1 (kHz)	336	90	87	90	80
f_2 (kHz)	342	87	90	84	72
Lissajous frequency (kHz)	6	3	3	6	8
Average addressing frequency (kHz)	24	12	6	12	16
Δt_{min} (ns)	52	383	192	397	329
a	0.0548	0.107	0.0524	0.111	0.0823
b	0.0558	0.104	0.0542	0.104	0.0741
Max. distortion	1.94e-3	13.7e-3	1.41e-3	11.7e-3	4.88e-3
$\rho_{add,min}$	20.6	9.78	19.7	9.76	13.7

Table 5.1: Comparison of Lissajous scan characteristics for a selection of frequency pairs. Length values a, b and distortion are given as a fraction of the total scan length L. Addressing ratios account for pulse smearing with a pulse duration $\tau_{\text{pulse}} = 6$ ns.

of scanning frequencies, with potentially large variations depending on whether the curve wraps over (second column) or not (third column). The change in addressing frequencies when swapping frequencies of each scanner is a consequence of the phase condition $\phi = 0$ imposed for scanner synchronisation (see appendix B). For the swapped frequencies $f_1 = 87$ kHz, $f_2 = 90$ kHz, the same addressing frequency can be achieved by using the condition $\phi = \pi$. In either case, using a wrapped-over pattern will result in a lower point density and thus a higher grid distortion. This table also confirms that these frequency choices lead to realistic values for an experimental realisation of the system, in terms of pulse source speed (Δt_{min}) and MEMS angular range (ρ_{add}).

5.3 Experimental results and performance

We adapted the previously shown 1D addressing setup with a second MEMS scanner according to the setup shown on Fig. 5.5. The first scanner was a non-tunable 400 µm diameter mirror with a fundamental tipping mode at approximately 87.6 kHz with 30 Vpp applied to one actuator. The second was a tunable 400 µm diameter mirror, with the same mode at approximately 91.4 kHz. We consequently selected addressing frequencies $f_1 = 87$ kHz and $f_2 = 90$ kHz to produce a properly spaced Lissajous pattern for grid addressing. This required tuning the second scanner by applying 7.8 Vdc to the

chevron thermal actuator (see section 3.4), and a voltage increase to approximately 40 Vpp on the first scanner to obtain equal scan lengths along both axes.

The relatively low average addressing frequency of 6 kHz led to a proportionally low signal to noise ratio, even for long camera exposure times. The target used was a thin layer of fluorescing solution held between two glass coverslips, which was found to give enough fluorescence to be detected at this addressing frequency. The spot diameter at the target plane was measured at 10.5 µm (D4σ), an increase from the one-dimensional setup which is explained by the increased scattering of the fluorescing sample, as well as the change from a 40× objective to a 20× objective in an effort to increase working distance, from 4 to 8 mm, alleviating the need to place targets in near contact with the objective.

The laser source and scanner electronics were controlled using Labview through a GPIB interface for handling of the startup sequence and actuation parameters. The voltage amplifiers used to actuate the MEMS (FLC 400A) ensured easy impedance handling, as they offer high (10 MΩ) input impedance and low (1 Ω) output impedance.

The scanners produced a scan length of 159 µm in the sample plane, corresponding to a scan length to spot size ration of $\rho_{\text{add}} = 15.1$. This was not enough to avoid overlapping of adjacent pulses ($\rho_{\text{add,min}} = 19.7$), but sufficient for the addressed points to remain easily distinguishable and evaluate the shape and distortion of addressed patterns. Fig. 5.8 shows images of various fluorescence images obtained with this configuration.

The observed patterns show a slight rotation of the grid axes due to the limited precision of the scanner assembly, with the x axis being rotated -2.5° from the horizontal and the y axis -2° from the vertical. The sample also exhibits variations in fluorescence intensity from uneven distribution of fluorescing material and localized photobleaching from repeated use. These effects are inherent to the experimental setup and can be improved with a different design, e.g. with a scanner mounting system allowing for in-plane rotation and a target free from bleaching.

The checker pattern shown on the left of Fig. 5.8 was used to evaluate the grid distortion resulting from the inherent deformation of the Lissajous pattern and potential

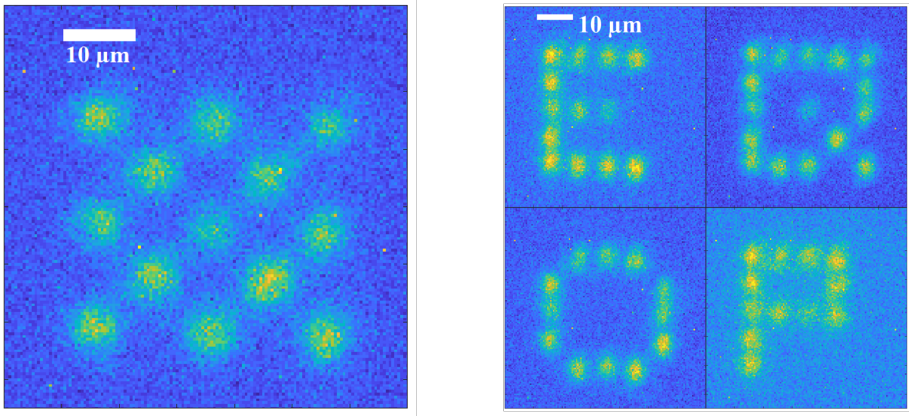

Figure 5.8: Fluorescence images obtained by addressing points on a 5x5 grid with an average addressing frequency of 6 kHz, after phase adjustment.

optical aberrations through the system. The position of the center of each fluorescence spot was compared to the expected position of the corresponding point on a 2D grid fitted to the top left, top right, and bottom left fluorescence points. Fitting the grid directly to those points is appropriate here, as changing the actuation voltage of the scanners allows control of the spacing parameters of the grid pattern. For the figure shown, this results in a 5x5 points, 33x30 µm grid.

Fig. 5.9 shows the same pattern with a rectangular grid superimposed for comparison. Overall, the center of every addressed point falls within 1 µm of the corresponding grid point, with a maximal deviation of 700 ± 420 nm. This value is much greater than the theoretical maximal distortion of 65 nm for this pattern, and thus cannot be explained by the Lissajous scan pattern alone. It is more likely that these discrepancies are due to the optical limitations of the system, as they remain close to the resolution limit of $\lambda/2\text{NA} = 542$ nm, and alignment imprecisions that arise from the manual assembly of a macroscale optical system. Overall, this maximal distortion translates to a deviation of 8.3% of the horizontal spacing and 8.2% of the vertical spacing parameters. This value could be further improved by using precision optomechanics for the alignment of parts, or within a carefully engineered design using fixed parts with strict tolerances to minimize aberrations within the system. Addressing precision is also limited by phase synchronization, which must be done manually for this system, as well as timing jitter in driving electronics which can lead to blurring as the laser pulses are not perfectly

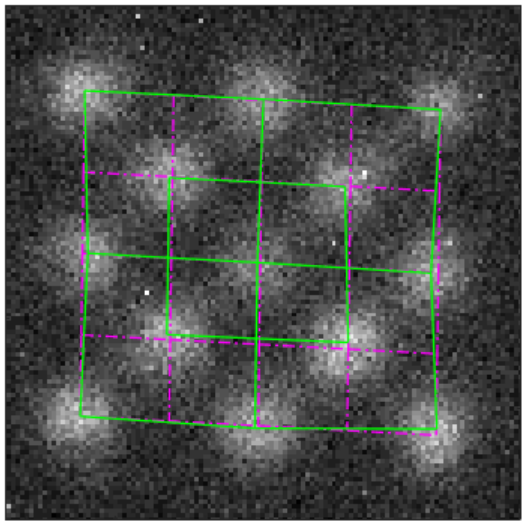

Figure 5.9: Comparison between addressed spot positions (green lines) and a rectangular grid (purple lines). The top left, top right and bottom left corners are matched to the corresponding spots.

synchronized with the scanning pattern: the Agilent 33250A signal generator used to drive the pulsed source specifies a frequency jitter of 30 parts-per-million for arbitrary waveforms, corresponding to 10 ns at a cycle frequency of 3 kHz, or approximately 5% of the minimal point-to-point duration. Pattern deformation from synchronisation effects are most visible in the images on the right of Fig. 5.8, notably on the "Q" and "O" patterns where uneven point alignment and spacing are visible.

Similarly, we have mentioned the insufficient scan length to spot size ratio to ensure fully separated spots. In first instance, this ratio could be improved by increasing scanner displacement, either through higher voltages or the use of several actuators, or by selecting different Lissajous frequencies to obtain a less dense pattern, for example swapping the axial frequencies to $f_1 = 90$ kHz and $f_2 = 87$ kHz or adding a phase factor $\phi = \pi$ to obtain a wrapped-over pattern (see section 5.2.2 and appendix B). This latter change would come at the cost of an increase in theoretical distortion by an order of magnitude, and likely an increase in optical aberrations from the larger pattern size. Again, these are issues that could likely be accounted for and corrected in an improved design.

5.4 Summary

The results presented in this chapter have demonstrated how the MEMS scanners can be used in a 2D addressing system, with a target scale appropriate for trapped atom and quantum optics experiments. It proposed a realisation of a simple optical design to achieve precise, high-speed addressing using resonant actuation in a Lissajous scan with well selected axial frequencies. The novel addressing method described here exploits the geometric properties of Lissajous curves to convert a continuous scan into sequential access to discrete points regularly spaced in a rectangular grid. This chapter showed an experimental implementation of this method for a 5×5, 30×30 µm grid. Grid distortion was contained within 1 µm for each point, or 8.3% of the grid geometric parameters.

Experimental results have demonstrated an effective random-access addressing frequency of 6 kHz, or $25 \times 6 = 150$ kHz for sequential addressing, with the capability to increase grid size while retaining the same addressing frequency. The current limitations of the system lie in the laser source speed, with a maximal repetition rate of 10 MHz preventing operation at maximal point density (see Table 5.1); optical precision, which appears to be the main contributor to the measured distortion; and electronics synchronization, the signal generators used being limited to a 10 ns resolution for pulse triggers and phase synchronization. These can all be improved through careful design using state-of-the-art elements. Frequency-tuning was also used to correct frequency discrepancies and implement Lissajous scanning at the desired frequencies, successfully producing a frequency shift of 1.4 kHz or 1.5% of the original resonance frequency.

Even without an arbitrary pulsed source available, continuous scanning can be useful to shape patterns in a continuous medium, or as a low-cost alternative to other beam-shaping elements for wide-field illumination [194]. The next chapter describes an experiment applying continuous Lissajous scanning in the context of a cold atom experiment.

Chapter 6

MEMS control system for spatially resolved addressing of trapped atoms

Following the demonstration of addressing of lattice locations on an artificial small-scale target shown in the previous chapter, the next step is the application of the MEMS scanner to an experiment including trapped atomic particles. Trapped-atom experiments come with their own set of requirements and constraints, such that adapting the scanning demonstration setup to an effective experimental configuration is a nontrivial task. It would then provide an opportunity to evaluate the performance of the previously characterised MEMS scanners within the context of such an experiment. It would also prove that precise control of trapped atomic particles using resonant MEMS scanners is indeed possible, completing the characterisation of the devices by demonstrating the scope of applications in which they can be used. The following chapter describes state preparation of rubidium atoms trapped within a magneto-optical trap.

While chapter 5 focused on the addressing of discrete, evenly spaced points, the experiment described here uses scanning of a cloud of cold atoms, which forms a continuous medium susceptible to any pattern fit within its spatial extent. This leads to an overall simpler configuration, eliminating the need for a light source capable of arbitrary pulse sequences, as well as fine control of the number of particles within the trap;

the number of atoms needs only to be sufficient to allow detection of the addressed locations. Nevertheless, demonstration of such addressing would still be a valid proof-of-concept, showing how the high resonance frequency MEMS scanners can be used to selectively control the state of trapped atoms inside a larger set, e.g. for state preparation in a quantum optics experiment. The requirements regarding scanner performance remain similar to the case of discrete addressing : the scan length to spot size ratio must allow addressing of the atom cloud with sufficient resolution – realistically ratios of 10 or greater – while frequency synchronisation is necessary for addressing specific patterns, e.g. ellipses with the scanners being actuated at equal frequencies. The scan frequency must also be fast enough to comply with the short duration of the experiment and atomic lifetime inside the cloud. With atom exposure durations in the order of 1 ms [111, 204], scan frequencies near 100 kHz are appropriate to form homogenous addressing patterns.

6.1 Experimental realization of 2D scanning within an atom trap

The following section describes the detail of the experimental apparatus and its operation. The design of the experiment involved three main parts: the magneto-optical trap for the containment of a cold atom cloud, the optical structure of the scanning system, and the control of scanner actuation. The general layout of the experiment is shown on Fig. 6.1, and a picture of the system is shown on Fig. 6.2.

Magneto-optical trap design and experiment sequence The atom trapping system is a magneto-optical trap (MOT), using a pair of coils to produce a magnetic quadrupole field, leading to the confinement of atoms through radiative force applied to the Zeeman-shifted energy levels of the atoms (see chapter 2). Unlike standard MOTs, the trap uses a diffractive grating to achieve confinement in three dimensions with a single beam through the interference of the incoming beam with the reflected diffraction orders [107,126], as previously mentioned in section 1.2. More precisely, the grating car-

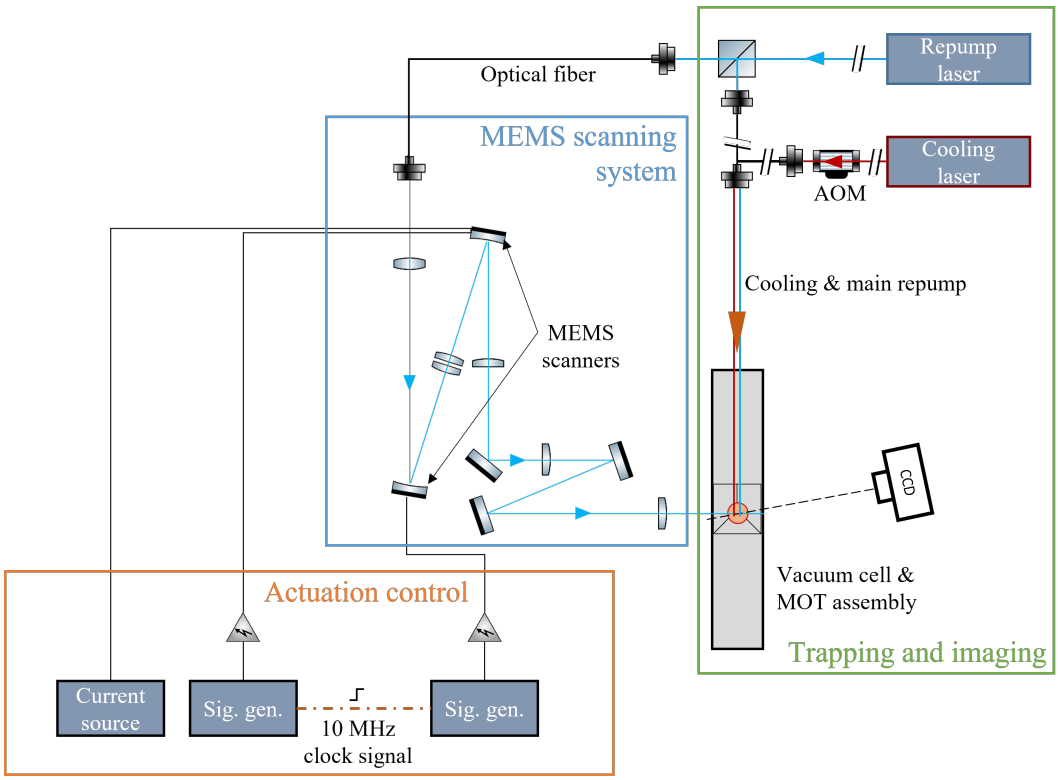

Figure 6.1: Simplified schematic of the trapped atom scanning experiment. The cooling laser, along with the optics for shaping, routing and control of the cooling and repump beams before the scanning system, are not shown. Not to scale.

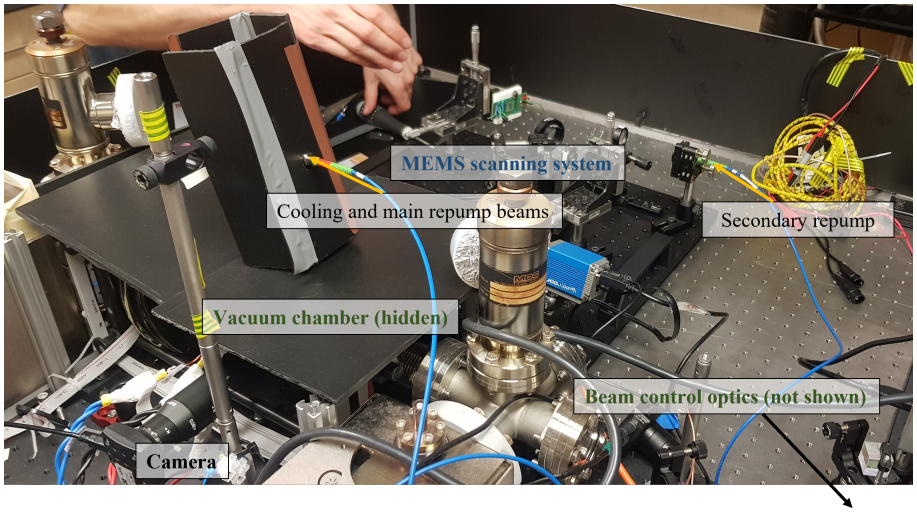

Figure 6.2: Picture of the MEMS scanning system integrated to the atom trapping experimental setup. Laser safety screens cover the cooling and interaction regions to protect the user during operation.

ries a triangular pattern forming a tetrahedral trapping potential, as shown for example in [108]. This configuration grants easier optical access to the atoms trapped within the MOT by leaving the side windows of the MOT chamber free of trapping elements. The MOT uses ^{87}Rb atoms, cooled in an optical molasses configuration through the $5^2S_{1/2}, F = 2 \rightarrow 5^2P_{3/2}, F = 3$ transition to form an atom cloud of approximately 10^6 atoms at a temperature of 50 µK; this results in atom velocities of the order of 10 cm/s with the trapping magnetic and optical fields turned off. The cooled atoms are confined within a volume with a characteristic length of approximately 2 mm, inside of a glass vacuum chamber with a 3x3 cm^2 cross-section. These values were monitored during the experiment by analyzing the fluorescence distribution of the atom cloud. The cooling beam, tuned to the cooling transition wavelength at 780 nm, has a power density of 4 mW/cm^2 with a top-hat profile over a diameter of roughly 2 cm, generated from a µQUANS ILS780-CST-01 laser with a linewidth of less than 50 kHz. The coil pair, made of two 8-turn coils with a 2.9 cm diameter separated by 34 mm, produces a field gradient of 14 G/cm near the center of the trapping potential. An acousto-optic modulator (AOM) is used to switch the trapping laser on and off, and the trap parameters can be controlled remotely to execute experimental sequences with precise timing.

When using the cooling transition $5^2S_{1/2}, F = 2 \rightarrow 5^2P_{3/2}, F = 3$, the cooling laser also drives the off-resonant transition $5^2S_{1/2}, F = 2 \rightarrow 5^2P_{3/2}, F = 2$, which may then decay to the $S_{1/2}, F = 1$ state; the resulting $F = 1$ state cannot be excited again by the cooling beam. The MOT configuration classically uses a "repump" beam to counteract this undesired effect. As the off-resonant transition is very weak compared to the main cooling transitions, the repump intensity necessary is similarly low, in the order of 0.1 mW/cm^2. While a typical cooling process requires illumination over the whole trap to preserve a large number of atoms, a repump beam smaller than the extent of the atom cloud can be used to selectively keep atoms in the cooling cycle. This effect can be observed as the atoms emit fluorescence when scattering through the cooling transition, while the non-repumped atoms are in the $F = 1$ "dark" state and do not emit any fluorescence. This forms the basis of the experiment, as steering the repump beam allows "painting" of excitation patterns within the atom cloud and provides local

control over the internal state of the atoms.

The experiment sequence for loading, cooling, scanning, and imaging of the atom cloud was as follows :

- load the MOT using the coil magnetic field and a cooling beam red-detuned for the transition $5^2S_{1/2}, F = 2 \rightarrow 5^2P_{3/2}, F = 3$, down to a temperature of ∼500 µK;
- turn off the MOT coils and reduce the intensity of the cooling beam to roughly 25% of the loading stage value, for further cooling in the optical molasses;
- shift the frequency of the laser to a blue-detuned frequency relative to the $5^2S_{1/2}$, $F = 2 \rightarrow 5^2P_{3/2}, F = 2$ transition and turn on the repump beam to selectively maintain atoms in a fluorescing state. This so-called "blue molasses" configuration increases atom density and pushes down the temperature, achieving the measured 50 µK temperature;
- acquire an image of the fluorescing atoms using both cooling and repump beam, then turn off the beams before taking a background image to subtract from the first measurement.

The atom fluorescence from inside the MOT is imaged by a CCD camera (pco.pixelfly) through a telescope formed by a 75 mm and a 150 mm focal length plano-convex lens, giving a magnification $M = 2$. The imaging system is rotated by 12° from the repump beam optical axis to avoid any laser light onto the detector. The fluorescence wavelength matches that of the cooling transition, at 780 nm.

6.1.1 Scanning system design

The scanners were placed in the same configuration as in chapter 5, with the MEMS scanners imaged onto each other through a matching lens pair and relayed to the final focusing lens through a telescope. Placing the scanner slightly out of focus of the incoming beam ensures a focused beam at the target while keeping the scanned beam parallel to the optical axis.

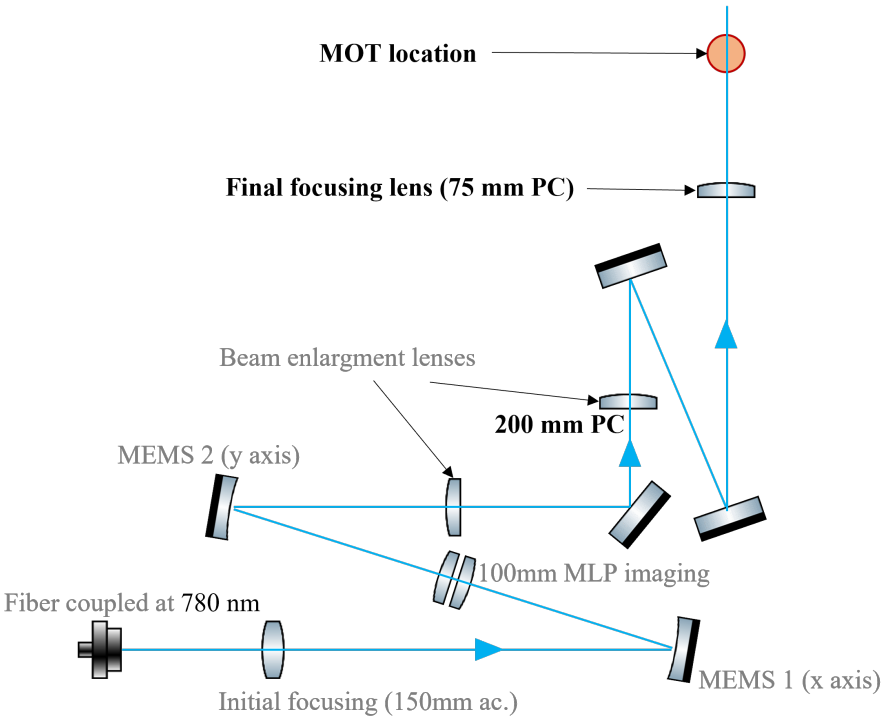

Figure 6.3: Adapted 2D scanning setup for the MOT painting experiment.

The focusing optics were adapted for the 780-nm wavelength repump beam, as the initial configuration was designed for 488-nm light and was susceptible to changes in beam size and focusing distances with the different wavelength. Furthermore, a longer working distance was required to focus the beam onto the atom cloud, as the vacuum chamber assembly only allowed optics to be placed 70 mm or further from the trap location. Consequently, the final focusing lens used was a 75-mm focal length plano-convex; the second telescope lens was changed to a 200 mm focal length plano-convex to ensure a small enough spot size, approximately 80 µm at the target plane, and its position shifted to ensure proper collimation. After alignment, the distance from the final lens to the MOT location was measured to be 90 mm. The adapted setup is shown on Fig. 6.3.

6.1.2 Frequency selection and tuning

An essential requirement of the experiment design was frequency synchronization of the scanners; operation at equal axial frequencies is necessary to form elliptic and diagonal

scanning patterns. The chosen axial frequency was 89 kHz, a compromise between the resonance frequencies of the horizontal (87.4 kHz for one actuator at 60 Vpp) and vertical (90.5 kHz) scanners. In order to achieve satisfactory scan lengths at this frequency, the vertical axis scanner was tuned using 7.5 Vdc on the chevron thermal actuator, just before the contact point to preserve displacement amplitude, and 10.5 Vdc on each of the single-track actuators. The non-tunable horizontal axis scanner was actuated using all 4 actuators. The phase between the actuators on either side of the rotation axis was controlled to produce maximal amplitude for the fundamental tipping mode, at approximately 140° phase. This discrepancy with the expected value of 180° is due to the differences in phase between actuation signal and scanner response, as the synchronization frequency corresponds to a different detuning from resonance for each scanner.

Both scanners were actuated with 60 Vpp applied to the actuators, providing enough displacement for this off-resonance actuation. It should also be noted that the horizontal axis scanner was actuated in the low amplitude branch of the hysteresis cycle to limit the scan length which would otherwise exceed the aperture of the matched lens pair.

In this configuration, and after adjustment of actuation voltages to produce scan lines of equal lengths, the scanning pattern is an ellipse whose axes are rotated 45° relative to the scanning axes and whose ellipticity depends on the phase between each axial scan. The length of the axes of the resulting ellipse can be calculated as a function of the phase by writing the axial coordinates equations as the parametric representation of an ellipse rotated by an angle of $\frac{\pi}{4}$:

$$\begin{cases} x(t) = \frac{L}{2}\cos(\omega t) = \frac{\sqrt{2}}{2}(a\cos u - b\sin u) \\ y(t) = \frac{L}{2}\sin(\omega t + \phi) = \frac{\sqrt{2}}{2}(a\cos u + b\sin u) \end{cases} \tag{6.1}$$

the sum and difference of these equations allow us to easily find

$$a = \frac{L}{\sqrt{2}}\cos\left(\frac{\pi}{4} - \frac{\phi}{2}\right), \quad b = \frac{L}{\sqrt{2}}\sin\left(\frac{\pi}{4} - \frac{\phi}{2}\right), \quad u = \omega t + \frac{\phi}{2} - \frac{\pi}{4}, \tag{6.2}$$

where L is the axial scan length, $\omega = 2\pi f$ the scanning frequency, ϕ the relative

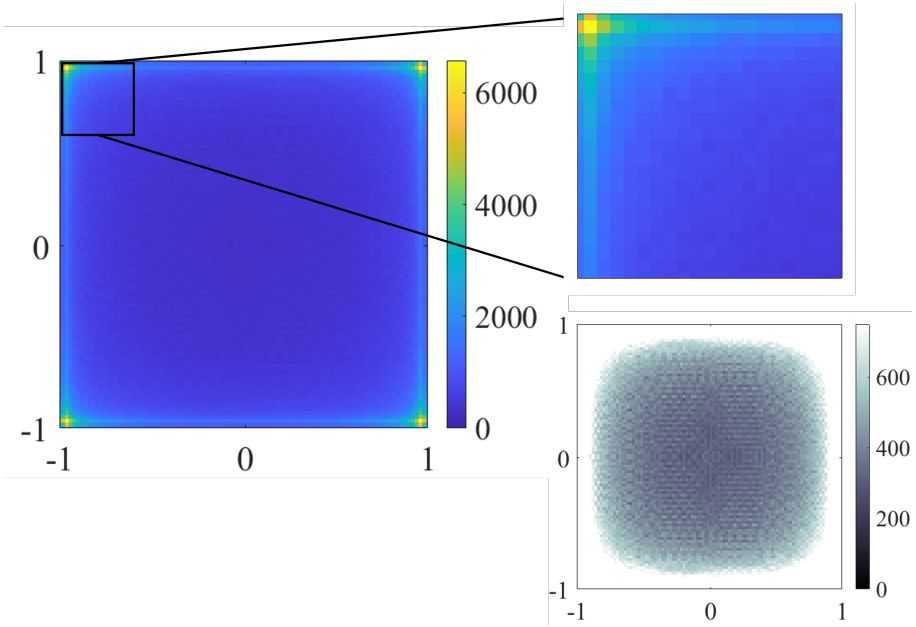

Figure 6.4: Power distribution for a Lissajous scan with $f_1 = 87.6$ kHz and $f_2 = 90.4$ kHz , and a truncated Gaussian beam with a width of 0.05, normalized to the scan amplitude. The corresponding pattern exhibits 1.97×10^5 crossing points. Bottom right shows the same figure with a lower maximum color value.

phase between both scanners, a and b the half-axes of the ellipse pattern, and u a normalized angular parameter. After synchronizing the internal clock of the actuation signal generators, the phase can be manually controlled at the time of the experiment. When combined with control over the scan length of each axis, this configuration is able to generate any line or ellipse pattern centered on the beam resting point that fits within the rectangle defined by the maximum length scan lines.

It is also possible to indiscriminately address a larger area by running the scanners unsynchronised at their own resonance frequencies, producing a dense Lissajous pattern illuminating the whole scanned area. This results in a non-uniform illumination, with higher average power at the corners and edges of the scanned area, as illustrated on figure 6.4

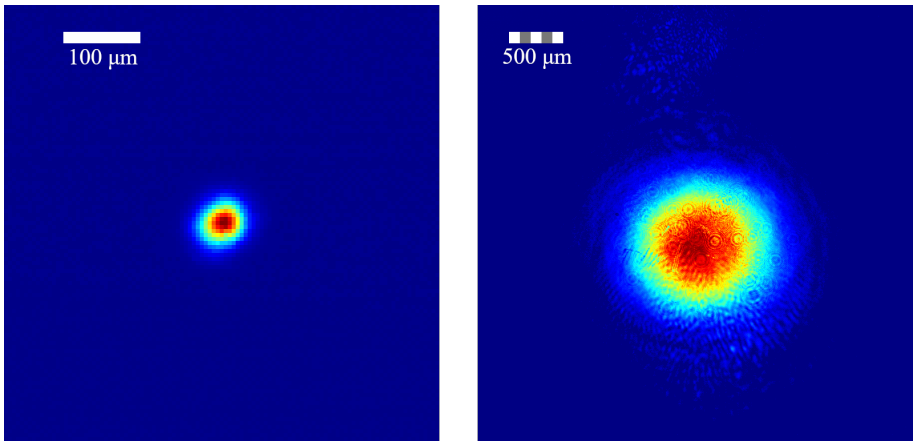

Figure 6.5: Left: profile of the focused beam at the MOT location, 90 mm away from the final focusing lens. Right: profile of the collimated beam, 189 mm before the final focusing lens. Colour scale is arbitrary for each picture.

6.2 Experimental results

6.2.1 Repump beam characterisation

The shape and size of the repump beam was measured before and after the final focusing lens. The corresponding beam profiles are shown on Fig. 6.5.

The collimated beam has a $1/e^2$ diameter of 1.36 mm, and is focused down to 80 µm at the MOT location; imprecision in collimation and optical alignment led to the MOT being slightly out of focus from the final lens, resulting in an effective beam size larger than the theoretical waist at focus of 55 µm. The beam retains a mostly Gaussian profile with an ellipticity of 0.87 (minor to major axis ratio). The collimated profile shows minor spherical aberration from reflections on the curved surface of the MEMS scanners. Similarly to the results shown in chapter 5, MEMS scanning did not induce any significant aberration onto the beam as the focused beams emerge parallel to the optical axis after the final lens.

The repump beam power was kept as low as possible to avoid saturation and scattering which may lead to an increased size of the addressed section. The total incoming power of the focused beam was measured at 9 nW, equal to an average intensity of 0.1 mW/cm^2 at the focus of the beam, roughly 4% of the saturation intensity for the transition [205].

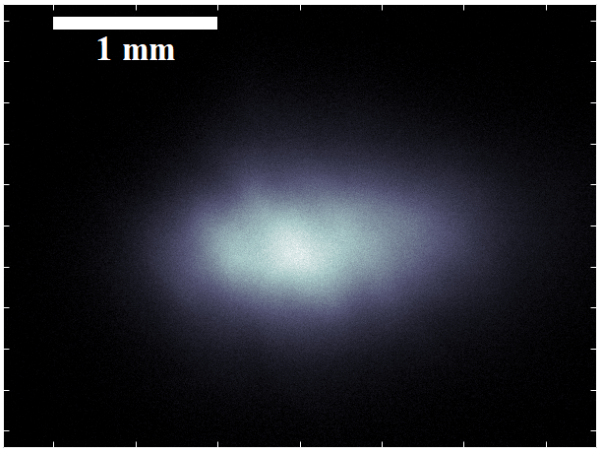

Figure 6.6: Fluorescence image of the MOT cloud, obtained with the main repump beam illuminating the trap with an exposure time of 1 ms. The estimated number of atoms for this measurement is 1.76×10^6.

MOT performance As previously stated, the magneto-optical trap produced atom clouds with approximately 10^6 atoms at a temperature of 50 µK; for comparison, the Doppler cooling limit for this transition is 145.6 µK [205]. Fig. 6.6 shows an image of the atom cloud with the main repump beam illuminating the whole trap; this beam uses the same optical path as the cooling beam and is not reflected off the scanners.

The cloud has the shape of an oblate spheroid, due to the shape of the trapping potential. It has a width of approximately 2.3 mm and a height of 1.2 mm (4σ Gaussian width). These values may slightly vary from measurement to measurement, as a result of changes in rubidium vapour density during loading and external vibrations affecting trapping beam alignment; the cloud remains large enough to fit the expected MEMS scan lines.

6.2.2 Atom cloud painting

Fig. 6.7 shows an image of the fluorescence obtained with the scanners at rest. The fluorescing spot has an elliptic Gaussian profile with a width of 340 µm and a height of 255 µm at half-maximum. The significantly larger spot size compared to the repump beam size is a consequence of re-scattering through the atomic cloud and atom motion during imaging – a velocity of 10 cm/s resulting in a displacement of 100 µm during the

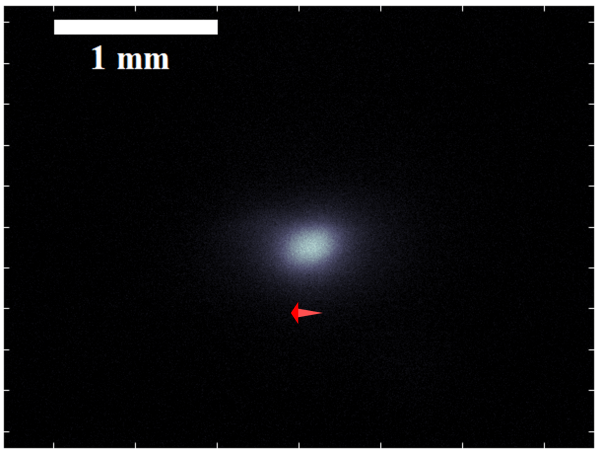

Figure 6.7: Fluorescence image of the cloud illuminated with the MEMS repump beam, with no actuation applied to the scanners, for an exposure time of 1 ms. The red arrow indicates the direction of beam propagation from the perspective of the camera – the beam propagates towards the detector, at an angle of 12° relative to the imaging axis.

imaging duration of 1 ms. The elliptic shape is in part due to the angle of the camera: a beam of diameter $w = 255$ µm, with fluorescence through the diameter $D_{\text{cloud}} = 2.3$ mm of the atom cloud, seen at an angle of $\theta_{\text{im}} = 12°$, would have an apparent width of $w_{\text{eff}} = w + D_{\text{cloud}} \sin(\theta_{\text{im}}) = 733$ µm; it is likely that this effect is mitigated by the depth of field of the imaging objective and the lower atom density near the edges of the atom cloud.

Turning on scanner the actuation produces the expected corresponding patterns, as shown on Fig. 6.8; in that case, the reduced average power seems to produce a smaller fluorescence feature size than for the beam at rest. For the horizontal scan (top left on the figure), the fluorescence spot width is 220 µm (FWHM) for a scan line length of 1.16 mm. The vertical scan has a line length of 705 µm for a width of 310 µm. The fluorescence intensity distributions for those patterns exhibits interesting properties. It is mostly uniform for horizontal scans (Fig. 6.8, top left), while it has a Gaussian shape matching that of the main repump fluorescence for vertical scans (top right); these properties are also observed for a rectangular scan (bottom left), while the intensity is not higher at the edges of the pattern, as would be expected from Fig. 6.4. This is a result of the specific three dimensional geometry of the atom cloud: fluorescence will saturate at lower repump intensities away from the center of the trap, where both the

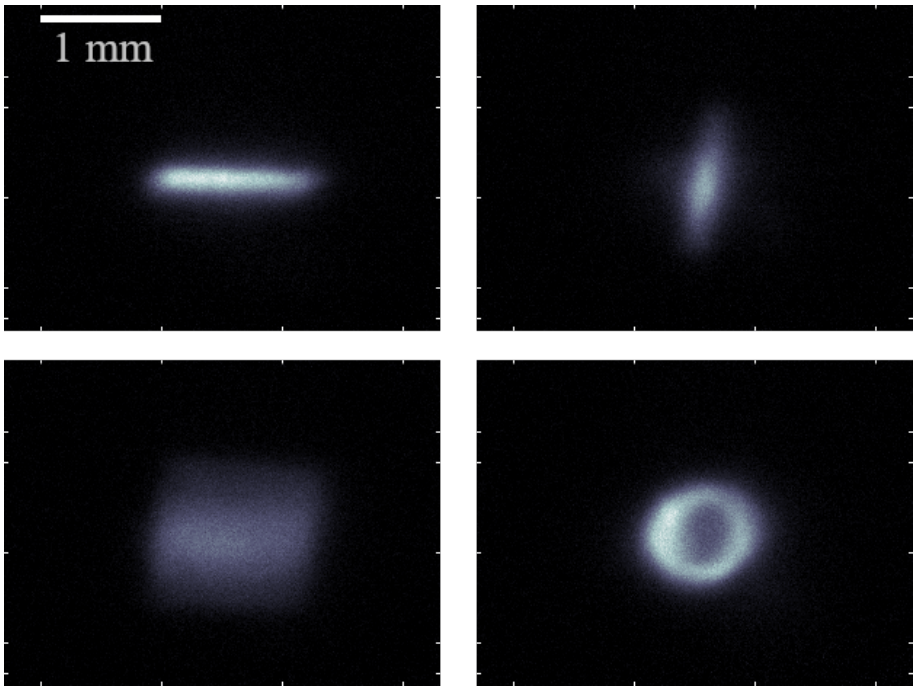

Figure 6.8: Fluorescence images with different repump scan configurations. Clockwise from top left: horizontal scan at 87.6 kHz; vertical scan at 90.4 kHz; synchronized scan with zero phase at 89 kHz; unsynchronized Lissajous scans at the same axial frequencies as the single axis scans. All pictures taken with 1 ms exposure time and with the same colour scale.

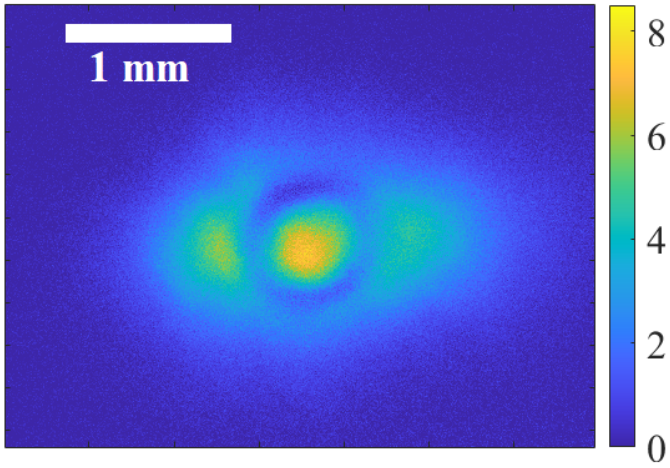

Figure 6.9: Subtraction of the image of a circular pattern from a fully repumped atom cloud. Colorscale units are arbitrary.

atom density and the thickness of the cloud traversed by the beam are reduced. Since the cloud is wider than it is high, the length covered by the horizontal scan is below saturation, while the vertical scan area is saturated except for the central region. In other words, fluorescence intensity is limited by beam power for the horizontal scan, and by atom number for the vertical scan. Regarding the rectangular scan, intensity at the edges of the pattern is again kept low by atom density. After phase synchronization and adjusting the axial amplitudes, the circular pattern has a diameter of 635 µm. The uneven linewidth corresponds to the ellipticity of the fluorescence spot on Fig. 6.7: in three dimensions, the pattern has the shape of a cylinder whose axis is that of the repump beam. From the perspective of the imaging system, this pattern appears as the two-dimensional projection of this cylinder, rotated by an angle θ_{im} from its axis. The apparent thickness of the line is in fact the projection of the height of the cylinder pattern.

Fig. 6.9 shows a subtraction of the circular pattern on Fig. 6.8 from the MOT image on Fig. 6.7. The reduced contrast near the horizontal axis of the MOT supports the previous observation of unsaturated fluorescence along the horizontal direction, and saturation near the vertical edges of the MOT.

Thus, these images show how the system can be used to selectively control the state of trapped atoms.

6.3 Summary

This chapter described and discussed the application of the 2D Lissajous scanning system to a magneto-optical trapping experiment. This experiment is based on a trapping and cooling procedure producing clouds of 10^6 rubidium 87 atoms at a temperature of 50 µK, contained in a volume of $2.3 \times 2.3 \times 1.2 = 6.3$ mm^3.

The scanning system was adapted to the trapping system, producing a repump beam with a waist of 80 µm focused on the center of the MOT, and steered with synchronized axial frequencies in an elliptical pattern at 89 kHZ. The scanned space has a size of 1160×705 µm, and a circular pattern with a diameter of 635 µm was produced, with well-resolved features when taking in account the uneven atom density within the cloud.

The experimental procedure has yielded significant findings: (1) the scanning speed is fast enough to be unaffected by atomic motion during the illumination process. The scanning period at 89 kHz is 11.2 µs, corresponding to an atom displacement of 1 µm at 10 cm/s. The increase in spot size on the images shown previously is instead a consequence of the considerably higher imaging duration (1 ms). (2) Frequency tuning can be used to synchronize scanners with different resonance frequencies to allow actuation at a single frequency while retaining satisfactory scan amplitude, even at frequencies far from the original device resonance. In this case, a shift of 1.4 kHz was produced with a corresponding optical scan angle greater than 2°. Finally, this experiment demonstrates how the MEMS scanners can operate at scales compatible with trapped atom requirements, generating scanning patterns with a size in the mm range, with features of the order of 100 µm. Such a system can be used as a basis for more complex experiments, by allowing preparation of arbitrary groups of atoms into different quantum state with high precision.

Chapter 7

General conclusions and future research perspectives

This work has examined many aspects of various theoretical and experimental approaches in optical MEMS and atom physics. This final chapter summarizes the findings described above to establish a general perspective of the presented work.

7.1 On MEMS design, characterization, and performance as optical devices

Micro-electromechanical system design is a domain as vast as their applications. The references discussed in the literature review reveal how a relatively narrow area of optical MEMS, resonant optical scanners, contains many device types varying in their size, manufacturing techniques, methods of actuation, performance and intended use. A drawback of the simple operation principles and high integration of MEMS is their lack of flexibility in their application; from this rigidity stems the need to develop new devices in order to achieve new applications. This was one of the motivations for this work, as the use of MEMS for quantum optics is still relatively new and limited. The devices presented here, however, were designed for an investigative approach, aiming to explore the device capabilities before examining the exact requirements for a given application, and with the intent of producing novel designs to expand the state-of-the-art of MEMS

scanners. These new scanners were nevertheless based on common MEMS design ideas, and should be considered as an evolution of previously existing elements rather than an entirely novel concept.

Consequently, this work details a characterization process of the presented MEMS, starting before the manufacturing step through simulation methods. This early analysis provided an estimate for the performance of the devices and their viability compared to other existing devices. In particular, it confirmed that smaller device scales would result in higher operating speeds, reaching frequency domains uncommon for optical scanners yet useful in the context of quantum optics. It also indicated that mechanical coupling could be used to leverage the low displacement, fast response times of piezoactuators to produce large stroke lengths and scanning angles, a key element to scanner performance. Further simulations of the device behaviour under thermal effects helped anticipate the operating limits and response of the scanners under high levels of incident radiation leading to heating effects, underlining the value of simulation software as a tool to analyse devices prior to their fabrication. Comparison with experimental results also revealed the limits of the simulation, in particular for predicting the magnitude of thermal effects.

A core part of the experimental results was the characterisation of the devices after they were manufactured through a multiuser microfabrication process. The performance of the devices was measured in terms of frequency response and scanning amplitudes, and the space of operational parameters was explored to find configurations that would optimize these values. The influence of scanner size and actuation amplitude was discussed, and overall the results obtained met the requirements outlined in the introductory chapters for single scanner performance. Table 7.1 regroups the results of the characterisation process for a few metrics of interest.

Device stability and reproducibility was a key point of the experimental findings. Scanner response measurements showed how the imperfections of the fabrication process led to large deviations in the operation frequencies – with standard deviations of 2-3%, see table 3.3 –, while hysteretic behavior for high scan amplitudes resulting from structure nonlinearities impacts the choice of operation parameters when large deflec-

Table 7.1: Summary of the MEMS scanner performance for various metrics, compared with values found in the literature for similar devices.

Scanner performance metric	This work	Typical values
Optical angular range (degrees)	18	20-50 [39, 149, 206, 207]
Scan frequency (kHz)	100-400	<50 [147, 208], 100-400 [209]
Maximum incident optical power (W/cm^2)	1600	48 [210], 0.1 [211]
Mirror plate length/diameter (mm)	0.2-0.4	0.5-1.5 [147, 207, 208, 212]
Maximum actuation voltage (Vpp)	60	5-60 [39, 147, 213]

tions angles are desired, as hysteresis cycles can span up to 2 kHz (see Fig. 3.15. The importance of frequency control for the synchronisation of resonant scanners led to the conception of a new device design that could circumvent these issues. Iterating upon the results obtained with the initial scanners, the tunable scanner design was proposed as a way to broaden the operational frequency range and make synchronization of several resonant scanners easier, by using thermoelectric heating to locally increase the temperature of the MEMS. The characterisation of these devices showed how localized on-chip heating can be used to produce significant frequency shifts at a moderate cost in chip space and power (less than 10 W with currents in the 100 mA range), while successfully enabling synchronization despite the existing discrepancies between scanners. This simple implementation of localized heating consequently increased the operational range of the scanners significantly, with induced frequency shifts of up to 8% of the original resnoance frequency. The resulting frequency tuning can be applied dynamically and reversibly at the time of operation, with much more flexibility than other approaches such as mass addition or removal, and is a feature that has not been found elsewhere in the literature.

This observation of temperature influence upon resonance frequencies prompted further examination of the devices' response to thermal effects, in particular frequency shifts induced by absorbed incident power and corresponding damage thresholds. Possibilities for active cooling were also investigated as a way to reverse the changes induced

by external heating. While cooling is possible by using the thermoelectric effect to drain heat from the MEMS die, measurements showed that the impact on scanner response is limited by the heat flux through the suspended structure. Cooling also comes at a significant space and power cost, requiring large heat sinks to dissipate the heat absorbed by a Peltier cell. Therefore, thermoelectric cooling does not appear as a viable method to mitigate radiation heating, except in situations where power levels and resonance frequency are critical and make the trade-off for an increased footprint acceptable. However, it may be applied with better results to larger devices that can more easily transfer heat to the die bulk and the Peltier cell. In general, thermal conditions and optical power levels should be considered when using any microfabricated optics, and the resonant scanners described here exhibit high sensitivity to these conditions, although not in a manner that should prevent device operation for reasonable values of power and temperature.

Overall, the characterisation results demonstrated how small, resonant scanners can produce high deflection angles by using thin-film piezoactuation, at frequencies much higher than other scanners described in the literature. It also showed how control elements can be used to improve or circumvent some of the limitations inherent to resonant devices so they can be adapted into more complex systems.

7.2 On their application to quantum optics and quantum control

The basis driving the design of the presented devices was the intent of integrating them into quantum optic applications, and in particular trapped atoms systems. While the initial characterisation showed that the scanners can operate at frequencies matching the requirements of quantum optics, the demonstration of such operation in a context relevant for practical use required additional considerations.

The first issue when using resonant scanners for addressing is the construction of an addressing scheme compatible with the constraints of scanner displacement imposed by the constant motion – the scanner cannot be paused at a given point of its motion

– but also with the requirements of the target. For the addressing of continuous media such as a cloud of atoms, power distribution is an important factor and will be affected by the harmonic motion of the scanners, applying higher average power at the edge of the scan line for a constant input power, although the power distribution may be approximated as constant near the center of the scan line. For discrete targets such as individually trapped particles, selective addressing requires a source that can be turned on or off at speeds matching that of the scanner. The nonlinear motion of the scanner makes the illumination timings nontrivial for evenly spaced targets, so that a pulsed source with a fixed repetition rate is not enough. That being said, modern laser diodes can provide extremely fast switching times in a wide range of wavelengths and power values, for arbitrary sequences of triggers; the limitations of laser sources rarely lie in optical switch-on/switch-off times, but rather in the bandwidth of electronics used, especially for applications requiring short ($<$ 10 ns) sequences of pulses at high frequencies and intensity. In any case, additional optical elements are likely to be required to tailor the MEMS scan obtained to the demands of an addressing experiment; the optical properties of the scanners make careful optical design all the more important. A limitation of the MEMS scanners is their small diameter, requiring focusing to fit the beam to the mirror plate. Surface imperfections and dynamic deformation may also degrade optical performance for applications that require precise control over the power distribution, although such an application has been demonstrated in another recent work [194]. Beam size and shape at the target plane are also an important concern for trapped particle experiments, and angular scanning can be a source of optical aberration if not accounted for adequately. Consequently, when considering a specific application, the drawbacks of the MEMS scanners – resonant actuation requirements, small aperture, surface imperfections, power sensitivity – must be weighed against their advantages – high frequency, small footprint, frequency stability, large deflection angles, low power requirements.

When considering two-dimensional addressing using a pair of scanners, synchronization between scanners must be taken into account in addition to the synchronization with the source and target. The relatively narrow range and statistical uncertainty

of scanning frequencies between different MEMS chips may render addressing schemes challenging to realise. This work proposes a novel method that makes use of the frequency discrepancies between devices to address evenly spaced 2D grids through Lissajous scanning. The mathematical description of this Lissajous addressing scheme show that high addressing rates can be retained (upwards of 20 kHz single-point frequency) provided that the axial frequencies were adequately chosen, and that the effective pattern is a good approximation of a 2D grid; to the knowledge of the author, this is the first time that Lissajous scanning has been implemented for discrete 2D addressing. The frequency tuning measurements also demonstrated how tuning may be used to facilitate frequency selection. Overall, it is statistically likely that any pair of devices can be used for Lissajous addressing, regardless of their specific resonance frequencies, using frequency tuning, although better performance may be reached for "well-matched" devices. Furthermore, the pattern spacing and density can be controlled by the individual frequencies of each axis, within the available range, to fit the target requirements. However, this addressing method retains the limitations of resonant scanning: each grid point is only addressed for a short time (∼10 ns) during each actuation cycle. Lissajous addressing is therefore better suited for targets requiring either very short addressing pulses in the nanosecond range, or on the other hand for effects with long timescales where the effect of short addressing pulses can be averaged over many scan cycles. Table 7.2 gives an overview of the addressing performance as it was exprimentally demonstrated in chapters 4 and 5.

The MOT painting experiment (chapter 6) also showed how 2D continuous scanning can be used for quantum control of groups of trapped particles. Specifically, it demonstrated the formation of arbitrary fluorescence patterns in a cloud of cold rubidium atoms, at a sub-millimeter scale with features approximately 300 µm in size. This allows preparation of certain areas of the cloud into an excited state, within a short time frame (11.2 µs scan time at 89 kHz) compared to the trapping duration scale (∼1ms). In this context, exact synchronization of axial scans proved useful as it allows formation of continuous 2D patterns to give greater control over the addressed regions, whereas a Lissajous pattern is of little use given the relative size of the target and of

Table 7.2: Summary of experimental addressing performance for one-dimensional and two-dimensional scanning. Sequential addressing frequency is calculated as the single-point addressing frequency multiplied by the number of points.

Scanner performance metric	1D scanning	2D scanning
Cycle frequency (kHz)	87.4	3
Number of addressable points	19	25
Average single-point addressing frequency (kHz)	174.8	6
Effective sequential addressing frequency (kHz)	3321.2	150
Spot size (µm)	5	10.5
Scan length (µm)	123	30
Maximal spot deviation (nm)	None	700±420

the addressing beams. Again, frequency tuning capability proved essential to achieve synchronization of the scanners on each axis.

7.3 On the miniaturization of experimental applications

The introduction chapter mentioned improved integration and miniaturization as one of the main motivations for this work, after observing how small size is an essential property of MEMS. While this work did not demonstrate a fully integrated system, steps were made towards significant reduction in the scale and size of the considered applications. A common method for beam steering involves using acousto-optic deflectors (AODs) to produce harmonic scanning using diffraction effects [88]. However, AODs have a number of drawbacks limiting their use: the produced deflection angle is wavelength-dependent, they require high RF power (∼1 W) signals for driving, and are limited to scan frequencies above 100 MHz [214]. Their fabrication also requires complex materials and the stringent crystal shape requirements makes the process expensive while making them relatively voluminous elements. The use of MEMS scanners instead of AODs thus presents a number of advantages, and particularly when smaller sizes are desired.

The literature review has shown the continuing interest for small-scale systems in quantum optics and photonics technologies in general. Quantum computing systems require high levels of vacuum and cooling, which are more readily obtainable in small

Table 7.3: Comparison between the performance of the studied devices and typical AODs. AOD data is taken from [214] unless specified otherwise.

Scanner performance metric	This work	AOD scanners
Aperture (mm)	0.2-0.4	1-10
Optical angular range (degrees)	18	$\leq$3
Average scan velocity (10^3 deg/s)	3600-14400	250-15000
Response time (µs)	$\gg 10^3$	0.5-15
Optical efficiency	65%	60-80%
Maximum optical power (W/cm^2)	1600	10^2-10^4
Electrical power consumption (W)	$< 10^{-3}$	1-2 [215, 216]

volumes. Additionally, constructing compact and robust systems is a key step towards the industrial production of quantum optics systems. The use of MEMS could be beneficial in this regard, since MEMS fabrication processes are already streamlined at industrial scales.

The optical setup used for demonstration of the 2D addressing, and the MOT painting experiment was fitted in a 45×45×20 cm^3 volume, whereas other systems such as AODs commonly require a footprint larger than 1 m^2 to fit the beam steering and relay optics. While still very much a macroscale system, this made it significantly easier to transport than optics mounted on an optical table, and demonstrate a basic degree of integration of the scanners within an optical system. Given the small size of the MEMS die (9×4.45 mm^2) and its 1"×1" carrier, there is no doubt that higher levels of miniaturization can be reached with a well-engineered design, beyond the proof of principle shown in this thesis.

7.4 Further research perspectives

While the characterisation of the devices represent a sizeable part of the present work , there are still many interesting elements and application opportunities that further research may explore.

This work demonstrated 1 and 2-dimensional scanning by using one scanner for each axis. The feasibility of 3-dimensional scanning using MEMS devices could be investigated as an extension of the system. 3D beam control requires a way to shift the

beam focus along the optical axis in addition to steering in the image plane, a function that cannot be realised by the scanners described here. Adding a varifocal mirror could enable focus shifting, a method that was previously demonstrated [217–219]. A 3D addressing system would offer even finer control when addressing 3D continuous media, and be relevant for addressing individual atoms in a 3D optical lattice [102,104]. Achieving the required optical performance, along with synchronization of three MEMS scanners, would pose an interesting design challenge, and static actuation might be preferable for the focus shift function.

Considering the present scanners, further work can be done in terms of advanced characterisation and potential design improvements. An in-depth study of resonance nonlinearity and phase response, including their exact physical origin and bistability conditions could bring light on new actuation control methods, along with the analysis of the scanners' response to perturbations and step response. A theoretical basis for the modeling of these nonlinearities would also be useful to quantify the mechanical properties of the device.

The reflectivity of base silicon remains suboptimal for mirrors operating at various optical ranges useful for quantum optics, be it UV ($<$ 60% at 370 nm, a cooling transition wavelength of ytterbium ions [220]), visible ($<$40% at 590 nm, the D_2 line of sodium [221]) or near-infrared ($<$35% at 780 nm, the D_1 line of rubidium 87 [205]). A refined coating method for deposition of smooth metallic layers could bring scanner reflectivity above 95%, greatly enhancing the optical efficiency of the mirror and reducing its susceptibility to thermal effects. Attempts at post-processing coating indicate that integrating the coating to the industrial fabrication process would be ideal to obtain satisfactory results. While the PiezoMUMPS process offers metallic layers, the surface quality of the layers is not specified and processing steps after metal deposition may lead to poor optical performance.

The frequency tuning capabilities of the scanners is an interesting feature that opens many possibilities even for single scanners. Measurements with summed eigenfrequencies signals revealed that tilting and tipping modes can be driven simultaneously, leading to Lissajous scanning with a single device. This could not be used for 2D addressing,

due to the large difference in resonance frequencies; however, the long suspension beams of the tunable scanner design resulted in the tilt II and tip I eigenfrequencies being separated by approximately 8kHz, making 2D Lissajous addressing with a single mirror potentially viable, especially since the tip I mode is affected much more strongly than tilting modes by heating frequency shifts. This would eliminate the need for a second scanner, greatly simplifying the optical structure and control electronics.

Perhaps the most interesting development from an experimental standpoint would be a further reduction in system size, as mentioned above. While the MEMS scanners themselves have a characteristic scale in the millimeter range, the applications described above are still human scaled, and intended for human assembly and operation. While this was sufficient for demonstrating the performance of the scanner, investigating possible designs using small size integrated optics to create an optical scanning system with a characteristic size of 10 cm or less would certainly be of great value. Device integration could then progress further by including the light source and driving electronics into the packaged system, a non-trivial development given the actuation requirements and in particular the current supply (up to 500 mA) required to operate the thermal tuning actuators. This could still probably be achieved in the current state-of-the-art with dedicated engineering.

As a closing observation, the scanners described here, while using common MEMS geometries and actuation methods, still showed novel results in their performance and behavior at high frequency. It is likely that these devices, and others of the same kind, can find a use for many applications in various domains beyond trapped particles, such as microscopy as was demonstrated in [194], communications, or optical sensing. They were presented in the context of the advancing state-of-the-art of MEMS technology and might be used as a basis for further evolutions of MEMS scanning methods.

Bibliography

[1] J. B. Angell, S. C. Terry, and P. W. Barth, "Silicon Micromechanical Devices.," *Scientific American*, vol. 248, no. 4, pp. 44–55, 1983.

[2] R. Ghodssi and P. Lin, *MEMS materials and processes handbook*, vol. 1. Springer Science & Business Media, 2011.

[3] R. P. Feynman, "There is plenty of room at bottom," *Engineering and Science*, vol. 23, no. 5, pp. 22–36, 1960.

[4] E. Drexler, "There's plenty of room at the bottom." `http://metamodern.com/2009/12/29/theres-plenty-of-room-at-the-bottom"-feynman-1959/`, Dec 2009. Retrieved from a 05/03/2016 snapshot on 10/02/2021.

[5] B. J. Kim and E. Meng, "Review of polymer MEMS micromachining," *Journal of Micromechanics and Microengineering*, vol. 26, p. 013001, nov 2015.

[6] A. A. Vasiliev, A. V. Sokolov, A. V. Legin, N. N. Samotaev, K. Y. Oblov, V. P. Kim, S. V. Tkachev, S. P. Gubin, G. N. Potapov, Y. V. Kokhtina, and A. V. Nisan, "Additive technologies for ceramic MEMS sensors," *Procedia Engineering*, vol. 120, pp. 1087–1090, 2015.

[7] H. Nathanson, W. Newell, R. Wickstrom, and J. Davis, "The resonant gate transistor," *IEEE Transactions on Electron Devices*, vol. 14, pp. 117–133, mar 1967.

[8] M. E. Motamedi, *MOEMS: Micro-opto-electro-mechanical Systems*, vol. 126. SPIE press, 2005.

[9] H. A. Waggener, "Electrochemically Controlled Thinning of Silicon," *Bell System Technical Journal*, vol. 49, pp. 473–475, mar 1970.

[10] R. M. Finne and D. L. Klein, "A Water-Amine-Complexing Agent System for Etching Silicon," *Journal of The Electrochemical Society*, vol. 114, no. 9, p. 965, 1967.

[11] F. Faggin, "The MOS silicon gate technology and the first microprocessors," *Rivista del Nuovo Cimento*, vol. 38, no. 12, pp. 575–620, 2015.

[12] E. W. Backer, W. Ehrfeld, D. Münchmeyer, H. Betz, A. Heuberger, S. Pongratz, W. Glashauser, H. J. Michel, and R. v. Siemens, "Production of separation-nozzle systems for uranium enrichment by a combination of X-ray lithography and galvanoplastics," *Naturwissenschaften*, vol. 69, pp. 520–523, nov 1982.

[13] H. Jansen, M. D. Boer, R. Legtenberg, and M. Elwenspoek, "The black silicon method: a universal method for determining the parameter setting of a fluorine-based reactive ion etcher in deep silicon trench etching with profile control," *Journal of Micromechanics and Microengineering*, vol. 5, pp. 115–120, jun 1995.

[14] H. Xie and G. K. Fedder, "Fabrication, characterization, and analysis of a DRIE CMOS-MEMS gyroscope," *IEEE Sensors Journal*, vol. 3, no. 5, pp. 622–631, 2003.

[15] D. L. Hitt, C. M. Zakrzwski, and M. A. Thomas, "MEMS-based satellite micropropulsion via catalyzed hydrogen peroxide decomposition," *Smart Materials and Structures*, vol. 10, no. 6, pp. 1163–1175, 2001.

[16] K. Noda, Y. Hashimoto, Y. Tanaka, and I. Shimoyama, "MEMS ON ROBOT APPLICATIONS The University of Tokyo , Tokyo , Japan . Information and Robot Technology (IRT) Research Initiative , Tokyo , Japan . MEASUREMENT," *Technology*, pp. 2176–2181, 2009.

[17] C. Liu, "Recent developments in polymer MEMS," *Advanced Materials*, vol. 19, no. 22, pp. 3783–3790, 2007.

[18] D. Zhang, B. Su, and T. W. Button, "Microfabrication of three-dimensional, free-standing ceramic MEMS components by soft moulding," *Advanced Engineering Materials*, vol. 5, no. 12, pp. 924–927, 2003.

[19] G. Tang, J. Q. Liu, B. Yang, J. B. Luo, H. S. Liu, Y. G. Li, C. S. Yang, D. N. He, V. D. Dao, K. Tanaka, and S. Sugiyama, "Fabrication and analysis of high-performance piezoelectric MEMS generators," *Journal of Micromechanics and Microengineering*, vol. 22, no. 6, 2012.

[20] P. Van Kessel, L. Hornbeck, R. Meier, and M. Douglass, "A mems-based projection display," *Proceedings of the IEEE*, vol. 86, no. 8, pp. 1687–1704, 1998.

[21] J. Ma, "Advanced MEMS-based technologies and displays," 2015.

[22] O. Solgaard, F. S. A. Sandejas, and D. M. Bloom, "Deformable grating optical modulator," *Optics Letters*, vol. 17, p. 688, may 1992.

[23] M. C. Wu, O. Solgaard, and J. E. Ford, "Optical MEMS for lightwave communication," *Journal of Lightwave Technology*, vol. 24, no. 12, pp. 4433–4454, 2006.

[24] L. J. Hornbeck, "128 × 128 Deformable Mirror Device," *IEEE Transactions on Electron Devices*, vol. 30, no. 5, pp. 539–545, 1983.

[25] R. S. Nesbitt, S. L. Smith, R. A. Molnar, and S. A. Benton, "Holographic recording using a digital micromirror device," in *Practical Holography XIII* (S. A. Benton, ed.), vol. 3637, pp. 12 – 20, International Society for Optics and Photonics, SPIE, 1999.

[26] D. Dudley, W. M. Duncan, and J. Slaughter, "Emerging digital micromirror device (DMD) applications," in *MOEMS Display and Imaging Systems* (H. Urey, ed.), vol. 4985, pp. 14 – 25, International Society for Optics and Photonics, SPIE, 2003.

[27] H. Urey and D. L. Dickensheets, "Display and imaging systems," in *MOEMS micro-opto-electro-mechanical systems* (M. E. Motamedi, ed.), ch. 8, pp. 369–452, Bellingham, WA: SPIE, 2005.

[28] B. R. Critchley, P. W. Blaxtan, B. Eckersley, R. O. Gale, and M. Burton, "Picture quality in large-screen projectors using the Digital Micromirror Device," *Journal of the Society for Information Display*, vol. 3, no. 4, p. 199, 1995.

[29] D. Dan, M. Lei, B. Yao, W. Wang, M. Winterhalder, A. Zumbusch, Y. Qi, L. Xia, S. Yan, Y. Yang, P. Gao, T. Ye, and W. Zhao, "DMD-based LED-illumination Super-resolution and optical sectioning microscopy," *Scientific Reports*, vol. 3, pp. 1–7, 2013.

[30] A. G. York, S. H. Parekh, D. D. Nogare, R. S. Fischer, K. Temprine, M. Mione, A. B. Chitnis, C. A. Combs, and H. Shroff, "Resolution doubling in live, multicellular organisms via multifocal structured illumination microscopy," *Nature Methods*, vol. 9, pp. 749–754, jul 2012.

[31] N. Huynh, E. Zhang, M. Betcke, S. Arridge, P. Beard, and B. Cox, "Single-pixel optical camera for video rate ultrasonic imaging," *Optica*, vol. 3, no. 1, p. 26, 2016.

[32] V. A. Aksyuk, F. Pardo, C. A. Bolle, S. Arney, C. R. Giles, and D. J. Bishop, "Lucent microstar micromirror array technology for large optical crossconnects," in *MOEMS and Miniaturized Systems* (M. E. Motamedi and R. Goering, eds.), vol. 4178, pp. 320–324, aug 2000.

[33] Tze-Wei Yeow, K. Law, and A. Goldenberg, "MEMS optical switches," *IEEE Communications Magazine*, vol. 39, no. 11, pp. 158–163, 2001.

[34] H. Schenk, P. Duerr, D. Kunze, H. K. Lakner, and H. Kueck, "Design and modeling of large deflection micromechanical 1D and 2D scanning mirrors," in *MOEMS and Miniaturized Systems* (M. E. Motamedi and R. Goering, eds.), vol. 4178, pp. 116–125, aug 2000.

[35] S. T. Holmström, U. Baran, and H. Urey, "MEMS laser scanners: A review," *Journal of Microelectromechanical Systems*, vol. 23, no. 2, pp. 259–275, 2014.

[36] P. M. Hagelin and O. Solgaard, "Optical raster-scanning displays based on surface-micromachined polysilicon mirrors," *IEEE Journal on Selected Topics in Quantum Electronics*, vol. 5, no. 1, pp. 67–74, 1999.

[37] H. Miyajima, N. Asaoka, T. Isokawa, M. Ogata, Y. Aoki, M. Imai, O. Fujimori, M. Katashiro, and K. Matsumoto, "A mems electromagnetic optical scanner for a commercial confocal laser scanning microscope," *Journal of Microelectromechanical Systems*, vol. 12, no. 3, pp. 243–251, 2003.

[38] A. Wolter, S.-T. Hsu, H. Schenk, and H. K. Lakner, "Applications and requirements for MEMS scanner mirrors," in *MOEMS and Miniaturized Systems V* (A. El-Fatatry, ed.), vol. 5719, p. 64, jan 2005.

[39] T. Iseki, M. Okumura, and T. Sugawara, "High-speed and wide-angle deflection optical MEMS scanner using piezoelectric actuation," *IEEJ Transactions on Electrical and Electronic Engineering*, vol. 5, no. 3, pp. 361–368, 2010.

[40] D. W. Wine, M. P. Helsel, L. Jenkins, H. Urey, and T. D. Osborn, "Performance of a biaxial MEMS-based scanner for microdisplay applications," in *MOEMS and Miniaturized Systems* (M. E. Motamedi and R. Goering, eds.), vol. 4178, pp. 186–196, aug 2000.

[41] Changho Chong, K. Isamoto, and H. Toshiyoshi, "Optically Modulated MEMS scanning endoscope," *IEEE Photonics Technology Letters*, vol. 18, pp. 133–135, jan 2006.

[42] J. Yao, "Wide-field fast-scanning photoacoustic microscopy based on a water-immersible MEMS scanning mirror," *Journal of Biomedical Optics*, vol. 17, p. 080505, aug 2012.

[43] H. Becker and C. Gärtner, "Polymer microfabrication technologies for microfluidic systems," *Analytical and Bioanalytical Chemistry*, vol. 390, no. 1, pp. 89–111, 2008.

[44] O. Rötting, W. Röpke, H. Becker, and C. Gärtner, "Polymer microfabrication technologies," *Microsystem Technologies*, vol. 8, no. 1, pp. 32–36, 2002.

[45] S. G. Kim, S. Priya, and I. Kanno, "Piezoelectric MEMS for energy harvesting," *MRS Bulletin*, vol. 37, no. 11, pp. 1039–1050, 2012.

[46] R. E. March, "Quadrupole ion traps," *Mass Spectrometry Reviews*, no. 28, pp. 961–989, 2009.

[47] W. Paul and H. Steinwedel, "Verfahren zur trennung bzw. zum getrennten nachweis von ionen verschiedener spezifischer ladung." Patent DE944900C (Germany), Jun 1956. Accessed at `https://patents.google.com/patent/DE944900C/da%20US4325121.pdf`.

[48] P. H. Dawson and N. R. Whetten, "Ion Storage in Three-Dimensional, Rotationally Symmetric, Quadrupole Fields. II. A Sensitive Mass Spectrometer," *Journal of Vacuum Science and Technology*, vol. 5, no. 1, pp. 11–18, 1968.

[49] H. Dehmelt, *Stored-Ion Spectroscopy*, pp. 153–187. Boston, MA: Pearson, 1983.

[50] D. J. Wineland, J. C. Bergquist, W. M. Itano, J. J. Bollinger, and C. H. Manney, "Atomic-Ion Coulomb Clusters in an Ion Trap," *Physical Review Letters*, vol. 59, no. 26, pp. 2935–2938, 1987.

[51] J. I. Cirac and P. Zoller, "Quantum computations with cold trapped ions," *Physical review letters*, vol. 74, no. 20, p. 4091, 1995.

[52] D. Kielpinski, C. Monroe, and D. J. Wineland, "Architecture for a large-scale ion-trap quantum computer," *Nature*, vol. 417, no. 6890, pp. 709–711, 2002.

[53] J. Reichel, W. Hänsel, and T. W. Hänsch, "Atomic micromanipulation with magnetic surface traps," *Physical Review Letters*, vol. 83, no. 17, pp. 3398–3401, 1999.

[54] R. Folman, P. Kröger, D. Cassettari, B. Hessmo, T. Maier, and J. Schmiedmayer, "Controlling cold atoms using nanofabricated surfaces: Atom chips," *Physical Review Letters*, vol. 84, no. 20, pp. 4749–4752, 2000.

[55] E. L. Raab, M. Prentiss, A. Cable, S. Chu, and D. E. Pritchard, "Trapping of Neutral Sodium Atoms with Radiation Pressure," *Physical Review Letters*, vol. 59, no. 23, pp. 2631–2634, 1987.

[56] D. Stick, W. Hensinger, S. Olmschenk, M. Madsen, K. Schwab, and C. Monroe, "Ion trap in a semiconductor chip," *Nature Physics*, vol. 2, no. 1, pp. 36–39, 2006.

[57] D. J. Wineland, D. Leibfried, M. D. Barrett, A. Ben-Kish, J. C. Bergquist, R. B. Blakestad, J. J. Bollinger, J. Briton, J. Chiaverini, B. Demarco, and et al., "Quantum control, quantum information processing, and quantum-limited metrology with trapped ions," *Laser Spectroscopy*, pp. 393–402, Dec 2005.

[58] G. Wilpers, P. See, P. Gill, and A. G. Sinclair, "A monolithic array of three-dimensional ion traps fabricated with conventional semiconductor technology," *Nature Nanotechnology*, vol. 7, no. 9, pp. 572–576, 2012.

[59] S. Seidelin, J. Chiaverini, R. Reichle, J. J. Bollinger, D. Leibfried, J. Britton, J. H. Wesenberg, R. B. Blakestad, R. J. Epstein, D. B. Hume, W. M. Itano, J. D. Jost, C. Langer, R. Ozeri, N. Shiga, and D. J. Wineland, "Microfabricated surface-electrode ion trap for scalable quantum information processing," *Physical Review Letters*, vol. 96, no. 25, pp. 1–5, 2006.

[60] D. Stick, K. Fortier, R. Haltli, C. Highstrete, D. Moehring, C. Tigges, and M. Blain, "Demonstration of a microfabricated surface electrode ion trap," *arXiv e-prints*, pp. arXiv–1008, 2010.

[61] D. L. Moehring, C. Highstrete, D. Stick, K. M. Fortier, R. Haltli, C. Tigges, and M. G. Blain, "Design, fabrication and experimental demonstration of junction surface ion traps," *New Journal of Physics*, vol. 13, no. 7, p. 075018, 2011.

[62] U. Tanaka, K. Suzuki, Y. Ibaraki, and S. Urabe, "Design of a surface electrode trap for parallel ion strings," *Journal of Physics B: Atomic, Molecular and Optical Physics*, vol. 47, no. 3, p. 035301, 2014.

[63] A. Van Rynbach, P. Maunz, and J. Kim, "An integrated mirror and surface ion trap with a tunable trap location," *Applied Physics Letters*, vol. 109, no. 22, p. 221108, 2016.

[64] M. Brownnutt, V. Letchumanan, G. Wilpers, R. C. Thompson, P. Gill, and A. G. Sinclair, "Controlled photoionization loading of88Sr+for precision ion-trap experiments," *Applied Physics B: Lasers and Optics*, vol. 87, no. 3, pp. 411–415, 2007.

[65] E. Mount, S. Y. Baek, M. Blain, D. Stick, D. Gaultney, S. Crain, R. Noek, T. Kim, P. Maunz, and J. Kim, "Single qubit manipulation in a microfabricated surface electrode ion trap," *New Journal of Physics*, vol. 15, no. 9, p. 093018, 2013.

[66] D. T. Allcock, T. P. Harty, H. A. Janacek, N. M. Linke, C. J. Ballance, A. M. Steane, D. M. Lucas, R. L. Jarecki, S. D. Habermehl, M. G. Blain, D. Stick, and D. L. Moehring, "Heating rate and electrode charging measurements in a scalable, microfabricated, surface-electrode ion trap," *Applied Physics B: Lasers and Optics*, vol. 107, no. 4, pp. 913–919, 2012.

[67] K. K. Mehta, A. M. Eltony, C. D. Bruzewicz, I. L. Chuang, R. J. Ram, J. M. Sage, and J. Chiaverini, "Ion traps fabricated in a CMOS foundry," *Applied Physics Letters*, vol. 105, no. 4, p. 044103, 2014.

[68] F. Lindenfelser, B. Keitch, D. Kienzler, D. Bykov, P. Uebel, M. A. Schmidt, P. S. J. Russell, and J. P. Home, "An ion trap built with photonic crystal fibre technology," *Review of Scientific Instruments*, vol. 86, no. 3, p. 033107, 2015.

[69] R. Bowler, J. Gaebler, Y. Lin, T. R. Tan, D. Hanneke, J. D. Jost, J. P. Home, D. Leibfried, and D. J. Wineland, "Coherent diabatic ion transport and separation in a multizone trap array," *Physical Review Letters*, vol. 109, no. 8, pp. 1–4, 2012.

[70] A. Walther, F. Ziesel, T. Ruster, S. T. Dawkins, K. Ott, M. Hettrich, K. Singer, F. Schmidt-Kaler, and U. Poschinger, "Controlling fast transport of cold trapped ions," *Physical Review Letters*, vol. 109, no. 8, pp. 1–5, 2012.

[71] C. Monroe and J. Kim, "Scaling the Ion Trap Quantum Processor," *Science*, vol. 339, no. 6124, pp. 1164–1169, 2013.

[72] M. H. Devoret and R. J. Schoelkopf, "Superconducting Circuits for Quantum Information: An Outlook," *Science*, vol. 339, pp. 1169–1174, mar 2013.

[73] E. Mount, C. Kabytayev, S. Crain, R. Harper, S. Y. Baek, G. Vrijsen, S. T. Flammia, K. R. Brown, P. Maunz, and J. Kim, "Error compensation of single-qubit gates in a surface-electrode ion trap using composite pulses," *Physical Review A - Atomic, Molecular, and Optical Physics*, vol. 92, no. 6, p. 060301, 2015.

[74] Y. Wang, M. Um, J. Zhang, S. An, M. Lyu, J. N. Zhang, L. M. Duan, D. Yum, and K. Kim, "Single-qubit quantum memory exceeding ten-minute coherence time," *Nature Photonics*, vol. 11, no. 10, pp. 646–650, 2017.

[75] D. J. Wineland, "Superposition, entanglement, and raising Schrödinger's cat," *Annalen der Physik*, vol. 525, no. 10-11, pp. 739–752, 2013.

[76] D. Hayes, D. N. Matsukevich, P. Maunz, D. Hucul, Q. Quraishi, S. Olmschenk, W. Campbell, J. Mizrahi, C. Senko, and C. Monroe, "Entanglement of atomic qubits using an optical frequency comb," *Physical Review Letters*, vol. 104, no. 14, pp. 1–4, 2010.

[77] S. Debnath, N. M. Linke, C. Figgatt, K. A. Landsman, K. Wright, and C. Monroe, "Demonstration of a small programmable quantum computer with atomic qubits," *Nature Publishing Group*, vol. 536, no. 7614, pp. 63–66, 2016.

[78] C. Huerta Alderete, S. Singh, N. H. Nguyen, D. Zhu, R. Balu, C. Monroe, C. M. Chandrashekar, and N. M. Linke, "Quantum walks and dirac cellular automata on a programmable trapped-ion quantum computer," *Nature Communications*, vol. 11, pp. 1–7, Jul 2020.

[79] S. Weidt, J. Randall, S. C. Webster, K. Lake, A. E. Webb, I. Cohen, T. Navickas, B. Lekitsch, A. Retzker, and W. K. Hensinger, "Trapped-Ion Quantum Logic with

Global Radiation Fields," *Physical Review Letters*, vol. 117, no. 22, p. 220501, 2016.

[80] C. Flühmann, T. L. Nguyen, M. Marinelli, V. Negnevitsky, K. Mehta, and J. Home, "Encoding a qubit in a trapped-ion mechanical oscillator," *Nature*, vol. 566, no. 7745, pp. 513–517, 2019.

[81] D. Leibfried, B. DeMarco, V. Meyer, M. Rowe, A. Ben-Kish, J. Britton, W. M. Itano, B. Jelenković, C. Langer, T. Rosenband, and D. J. Wineland, "Trapped-Ion Quantum Simulator: Experimental Application to Nonlinear Interferometers," *Physical Review Letters*, vol. 89, no. 24, pp. 1–4, 2002.

[82] J. W. Britton, B. C. Sawyer, A. C. Keith, C. C. Wang, J. K. Freericks, H. Uys, M. J. Biercuk, and J. J. Bollinger, "Engineered two-dimensional Ising interactions in a trapped-ion quantum simulator with hundreds of spins," *Nature*, vol. 484, no. 7395, pp. 489–492, 2012.

[83] C. Kokail, C. Maier, R. van Bijnen, T. Brydges, M. K. Joshi, P. Jurcevic, C. A. Muschik, P. Silvi, R. Blatt, C. F. Roos, and P. Zoller, "Self-verifying variational quantum simulation of lattice models," *Nature*, vol. 569, no. 7756, pp. 355–360, 2019.

[84] G. Pagano, A. Bapat, P. Becker, K. S. Collins, A. De, P. W. Hess, H. B. Kaplan, A. Kyprianidis, W. L. Tan, C. Baldwin, L. T. Brady, A. Deshpande, F. Liu, S. Jordan, A. V. Gorshkov, and C. Monroe, "Quantum approximate optimization of the long-range Ising model with a trapped-ion quantum simulator," *Proceedings of the National Academy of Sciences of the United States of America*, vol. 117, no. 41, pp. 25396–25401, 2020.

[85] M. Keil, O. Amit, S. Zhou, D. Groswasser, Y. Japha, and R. Folman, "Fifteen years of cold matter on the atom chip: promise, realizations, and prospects," *Journal of Modern Optics*, vol. 63, no. 18, pp. 1840–1885, 2016.

[86] J. Wang, F. Sciarrino, A. Laing, and M. G. Thompson, "Integrated photonic quantum technologies," *Nature Photonics*, vol. 14, pp. 273–284, may 2020.

[87] J. Kim, S. Crain, C. Fang, J. Joseph, and J. Kim, "Enabling Trapped Ion Quantum Computing with MEMS Technology," *2017 International Conference on Optical MEMS and Nanophotonics (OMN)*, pp. 4–5, 2017.

[88] C. Knoernschild, C. Kim, F. P. Lu, and J. Kim, "Multiplexed broadband beam steering system utilizing high speed MEMS mirrors.," *Optics express*, vol. 17, no. 9, pp. 7233–7244, 2009.

[89] M. Lee, M. Lee, S. Hong, K. Schüppert, Y. D. Kwon, T. Kim, Y. Colombe, T. E. Northup, D. I. Cho, and R. Blatt, "Microelectromechanical-System-Based Design of a High-Finesse Fiber Cavity Integrated with an Ion Trap," *Physical Review Applied*, vol. 12, no. 4, p. 1, 2019.

[90] C. Knoernschild, X. L. Zhang, L. Isenhower, A. T. Gill, F. P. Lu, M. Saffman, and J. Kim, "Independent individual addressing of multiple neutral atom qubits with a micromirror-based beam steering system," *Applied Physics Letters*, vol. 97, no. 13, pp. 1–4, 2010.

[91] S. Crain, E. Mount, S. Baek, and J. Kim, "Individual addressing of trapped 171Yb+ ion qubits using a microelectromechanical systems-based beam steering system," *Applied Physics Letters*, vol. 105, no. 18, pp. 1–4, 2014.

[92] D. I. D. Cho, S. Hong, M. Lee, and T. Kim, "A review of silicon microfabricated ion traps for quantum information processing," *Micro and Nano Systems Letters*, vol. 3, no. 1, pp. 31–34, 2015.

[93] R. Blatt and D. Wineland, "Entangled states of trapped atomic ions," *Nature*, vol. 453, no. 7198, pp. 1008–1015, 2008.

[94] C. D. Bruzewicz, J. Chiaverini, R. McConnell, and J. M. Sage, "Trapped-ion quantum computing: Progress and challenges," *Applied Physics Reviews*, vol. 6, no. 2, p. 021314, 2019.

[95] P. Jessen and I. Deutsch, "Optical lattices," *Advances in Atomic, Molecular, and Optical Physics*, vol. 37, pp. 95–138, 1996.

[96] T. Fukuhara, A. Kantian, M. Endres, M. Cheneau, P. Schauß, S. Hild, D. Bellem, U. Schollwöck, T. Giamarchi, C. Gross, I. Bloch, and S. Kuhr, "Quantum dynamics of a mobile spin impurity," *Nature Physics*, vol. 9, no. 4, pp. 235–241, 2013.

[97] M. Mitchell, A. Di Carli, G. Sinuco-León, A. La Rooij, S. Kuhr, and E. Haller, "Floquet solitons and dynamics of periodically driven matter waves with negative effective mass," *Physical review letters*, vol. 127, no. 24, p. 243603, 2021.

[98] M. Takamoto, F. L. Hong, R. Higashi, and H. Katori, "An optical lattice clock," *Nature*, vol. 435, no. 7040, pp. 321–324, 2005.

[99] B. J. Bloom, T. L. Nicholson, J. R. Williams, S. L. Campbell, M. Bishof, X. Zhang, W. Zhang, S. L. Bromley, and J. Ye, "An optical lattice clock with accuracy and stability at the 10-18 level," *Nature*, vol. 506, no. 7486, pp. 71–75, 2014.

[100] L. Isenhower, E. Urban, X. L. Zhang, A. T. Gill, T. Henage, T. A. Johnson, T. G. Walker, and M. Saffman, "Demonstration of a neutral atom controlled-nOT quantum gate," *Physical Review Letters*, vol. 104, no. 1, pp. 8–11, 2010.

[101] C. J. Picken, R. Legaie, K. McDonnell, and J. D. Pritchard, "Entanglement of neutral-atom qubits with long ground-Rydberg coherence times," *Quantum Science and Technology*, vol. 4, no. 1, 2019.

[102] K. D. Nelson, X. Li, and D. S. Weiss, "Imaging single atoms in a three-dimensional array," *Nature Physics*, vol. 3, no. 8, pp. 556–560, 2007.

[103] S. E. Anderson, K. C. Younge, and G. Raithel, "Trapping Rydberg atoms in an optical lattice," *Physical Review Letters*, vol. 107, no. 26, p. 263001, 2011.

[104] Y. Wang, X. Zhang, T. A. Corcovilos, A. Kumar, and D. S. Weiss, "Coherent Addressing of Individual Neutral Atoms in a 3D Optical Lattice," *Physical Review Letters*, vol. 115, no. 4, pp. 1–5, 2015.

[105] J. J. Arlt, O. Maragö, S. Webster, S. Hopkins, and C. J. Foot, "A pyramidal magneto-optical trap as a source of slow atoms," *Optics Communications*, vol. 157, no. 1-6, pp. 303–309, 1998.

[106] S. Pollock, J. P. Cotter, A. Laliotis, and E. A. Hinds, "Integrated magneto-optical traps on a chip using silicon pyramid structures," *Optics Express*, vol. 17, no. 16, p. 14109, 2009.

[107] M. Vangeleyn, P. F. Griffin, E. Riis, and A. S. Arnold, "Laser cooling with a single laser beam and a planar diffractor," *Optics Letters*, vol. 35, no. 20, p. 3453, 2010.

[108] C. C. Nshii, M. Vangeleyn, J. P. Cotter, P. F. Griffin, E. A. Hinds, C. N. Ironside, P. See, A. G. Sinclair, E. Riis, and A. S. Arnold, "A surface-patterned chip as a strong source of ultracold atoms for quantum technologies," *Nature Nanotechnology*, vol. 8, no. 5, pp. 321–324, 2013.

[109] M. Takamoto, I. Ushijima, N. Ohmae, T. Yahagi, K. Kokado, H. Shinkai, and H. Katori, "Test of general relativity by a pair of transportable optical lattice clocks," *Nature Photonics*, vol. 14, no. 7, pp. 411–415, 2020.

[110] S. Knappe, V. Shah, P. D. Schwindt, L. Hollberg, J. Kitching, L. A. Liew, and J. Moreland, "A microfabricated atomic clock," *Applied Physics Letters*, vol. 85, no. 9, pp. 1460–1462, 2004.

[111] D. Hunter, S. Piccolomo, J. D. Pritchard, N. L. Brockie, T. E. Dyer, and E. Riis, "Free-Induction-Decay Magnetometer Based on a Microfabricated Cs Vapor Cell," *Physical Review Applied*, vol. 10, no. 1, p. 1, 2018.

[112] S. J. Ingleby, I. C. Chalmers, T. E. Dyer, P. F. Griffin, and E. Riis, "Resonant very low-and ultra low frequency digital signal reception using a portable atomic magnetometer," *arXiv e-prints*, pp. arXiv–2003, 2020.

[113] O. S. Burrow, P. F. Osborn, E. Boughton, F. Mirando, D. P. Burt, P. F. Griffin, A. S. Arnold, and E. Riis, "Stand-alone vacuum cell for compact ultracold quantum technologies," *Applied Physics Letters*, vol. 119, no. 12, pp. 3–9, 2021.

[114] T. Brecht, W. Pfaff, C. Wang, Y. Chu, L. Frunzio, M. H. Devoret, and R. J. Schoelkopf, "Multilayer microwave integrated quantum circuits for scalable quantum computing," *npj Quantum Information*, vol. 2, p. 16002, nov 2016.

[115] A. Orieux and E. Diamanti, "Recent advances on integrated quantum communications," *Journal of Optics (United Kingdom)*, vol. 18, no. 8, p. 083002, 2016.

[116] J. Silverstone, J. Wang, D. Bonneau, P. Sibson, R. Santagati, C. Erven, J. O'Brien, and M. Thompson, "Silicon quantum photonics," in *2016 International Conference on Optical MEMS and Nanophotonics (OMN)*, vol. 1, pp. 1–2, IEEE, jul 2016.

[117] D. J. Wineland, C. Monroe, W. M. Itano, D. Leibfried, B. E. King, and D. M. Meekhof, "Experimental Issues in Coherent Quantum-State Manipulation of Trapped Atomic Ions," *Journal of Research of the National Institute of Standards and Technology*, vol. 103, no. 3, pp. 259–328, 1998.

[118] D. Leibfried, R. Blatt, C. Monroe, and D. Wineland, "Quantum dynamics of single trapped ions," *Review of Modern Physics*, vol. 75, no. 1, pp. 281–324, 2003.

[119] A. Steane, "The ion trap quantum information processor," *Applied Physics B: Lasers and Optics*, vol. 64, no. 6, pp. 623–642, 1997.

[120] P. K. Ghosh, *Ion traps*. Oxford science publications, Oxford : New York: Clarendon Press ; Oxford University Press, 1995.

[121] N. Akerman, N. Navon, S. Kotler, Y. Glickman, and R. Ozeri, "Universal gate-set for trapped-ion qubits using a narrow linewidth diode laser," *New Journal of Physics*, vol. 17, no. 11, p. 113060, 2015.

[122] Y. Lu, S. Zhang, K. Zhang, W. Chen, Y. Shen, J. Zhang, J. N. Zhang, and K. Kim, "Global entangling gates on arbitrary ion qubits," *Nature*, vol. 572, no. 7769, pp. 363–367, 2019.

[123] R. Blume-Kohout, J. K. Gamble, E. Nielsen, J. Mizrahi, J. D. Sterk, and P. Maunz, "Robust, self-consistent, closed-form tomography of quantum logic gates on a trapped ion qubit," *arXiv preprint arXiv:1310.4492*, 2013.

[124] C. J. Foot *et al.*, *Atomic physics*, vol. 7. Oxford University Press, 2005.

[125] J. Mcclelland, A. Steele, B. Knuffman, K. Twedt, A. Schwarzkopf, and T. Wilson, "Bright focused ion beam sources based on laser-cooled atoms," *Applied Physics Reviews*, vol. 3, p. 011302, 10 2015.

[126] J. P. McGilligan, P. F. Griffin, R. Elvin, S. J. Ingleby, E. Riis, and A. S. Arnold, "Grating chips for quantum technologies," *Scientific Reports*, vol. 7, no. 1, pp. 1–7, 2017.

[127] Y. Wang, A. Kumar, T.-Y. Wu, and D. S. Weiss, "Single-qubit gates based on targeted phase shifts in a 3D neutral atom array," *Science*, vol. 352, no. 6293, pp. 1562–1565, 2016.

[128] Y.-H. Seo, K. Hwang, H. Kim, and K.-H. Jeong, "Scanning MEMS Mirror for High Definition and High Frame Rate Lissajous Patterns," *Micromachines*, vol. 10, p. 67, jan 2019.

[129] C. H. Han, D. H. Choi, and J. B. Yoon, "Parallel-plate MEMS variable capacitor with superior linearity and large tuning ratio using a levering structure," *Journal of Microelectromechanical Systems*, vol. 20, no. 6, pp. 1345–1354, 2011.

[130] J. Bryzek and E. Abbott, "Control Issues for MEMS," in *42nd IEEE International Conference on Decision and Control (IEEE Cat. No.03CH37475)*, vol. 3, pp. 3039–3047, IEEE, 2005.

[131] L. Dong and J. Edwards, "Closed-loop voltage control of a parallel-plate MEMS electrostatic actuator," *Proceedings of the 2010 American Control Conference, ACC 2010*, pp. 3409–3414, 2010.

[132] W. Ye and S. Mukherjee, "Design and fabrication of an electrostatic variable gap comb drive in micro-electro-mechanical systems," *American Society of Mechanical Engineers, Dynamic Systems and Control Division (Publication) DSC*, vol. 66, no. 1, pp. 537–544, 1998.

[133] M. W. Judy and T. C. H. Nguyen, "Electrostatic-comb drive of lateral polysilicon resonators," *Micromechanics and MEMS: Classic and Seminal Papers to 1990*, vol. 23, pp. 194–197, 1997.

[134] J. Yao, S. Park, R. Anderson, and J. DeNatale, "A Low Power/Low Voltage Electrostatic Actuator for RF MEMS Applications," in *2000 Solid-State, Actuators, and Microsystems Workshop Technical Digest*, (San Diego, CA USA), pp. 246–249, Transducer Research Foundation, Inc., jun 2000.

[135] M. Sinclair, "A high force low area mems thermal actuator," in *ITHERM 2000. The Seventh Intersociety Conference on Thermal and Thermomechanical Phenomena in Electronic Systems (Cat. No.00CH37069)*, vol. 1, pp. 127–132, 2000.

[136] D. Yan, A. Khajepour, and R. Mansour, "Design and modeling of a MEMS bidirectional vertical thermal actuator," *Journal of Micromechanics and Microengineering*, vol. 14, no. 7, pp. 841–850, 2004.

[137] D. Wang, S. Strassle Rojas, A. Shuping, Z. Tasneem, S. Koppal, and H. Xie, "An Integrated Forward-View 2-Axis Mems Scanner for Compact 3D Lidar," in *2018 IEEE 13th Annual International Conference on Nano/Micro Engineered and Molecular Systems (NEMS)*, pp. 185–188, IEEE, apr 2018.

[138] M. Lara-Castro, A. Herrera-Amaya, M. A. Escarola-Rosas, M. Vázquez-Toledo, F. López-Huerta, L. A. Aguilera-Cortés, and A. L. Herrera-May, "Design and modeling of polysilicon electrothermal actuators for a MEMS mirror with low power consumption," *Micromachines*, vol. 8, no. 7, 2017.

[139] X. Zhang, L. Zhou, and H. Xie, "A fast, large-stroke electrothermal MEMS mirror based on Cu/W bimorph," *Micromachines*, vol. 6, no. 12, pp. 1876–1889, 2015.

[140] J. Morrison, M. Imboden, T. D. Little, and D. J. Bishop, "Electrothermally actuated tip-tilt-piston micromirror with integrated varifocal capability," *Optics Express*, vol. 23, no. 7, p. 9555, 2015.

[141] A. Paterson, R. Bauer, R. Li, W. Lubeigt, and D. Uttamchandani, "Wavelength tuning of a solid-state laser with a tilting MEMS micromirror," *International Conference on Optical MEMS and Nanophotonics*, vol. 2016-September, pp. 30–31, 2016.

[142] F. Han, W. Wang, X. Zhang, and H. Xie, "Modeling and control of a large-stroke electrothermal MEMS mirror for fourier transform microspectrometers," *Journal of Microelectromechanical Systems*, vol. 25, no. 4, pp. 750–760, 2016.

[143] L. Li, R. Bauer, G. Brown, and D. Uttamchandani, "A symmetric hybrid MEMS scanner with electrothermal and electrostatic actuators," *International Conference on Optical MEMS and Nanophotonics*, pp. 163–164, 2011.

[144] D. Wang, C. Watkins, S. Koppal, M. Li, Y. Ding, and H. Xie, "A Compact Omnidirectional Laser Scanner Based on an Electrothermal Tripod Mems Mirror for Lidar Please Leave," in *2019 20th International Conference on Solid-State Sensors, Actuators and Microsystems & Eurosensors XXXIII (TRANSDUCERS & EUROSENSORS XXXIII)*, vol. 1, pp. 1526–1529, IEEE, jun 2019.

[145] I. G. Mina, H. Kim, I. Kim, S. K. Park, K. Choi, T. N. Jackson, R. L. Tutwiler, and S. Trolier-McKinstry, "High frequency piezoelectric MEMS ultrasound transducers," *IEEE Transactions on Ultrasonics, Ferroelectrics, and Frequency Control*, vol. 54, no. 12, pp. 2422–2429, 2007.

[146] Y. Yang, R. Lu, T. Manzaneque, and S. Gong, "Toward Ka Band Acoustics: Lithium Niobate Asymmetrical Mode Piezoelectric MEMS Resonators," *IFCS 2018 - IEEE International Frequency Control Symposium*, pp. 1–5, 2018.

[147] U. Baran, D. Brown, S. Holmstrom, D. Balma, W. O. Davis, P. Muralt, and H. Urey, "Resonant PZT MEMS scanner for high-resolution displays," *Journal of Microelectromechanical Systems*, vol. 21, no. 6, pp. 1303–1310, 2012.

[148] Y. Zhu, W. Liu, K. Jia, W. Liao, and H. Xie, "A piezoelectric unimorph actuator based tip-tilt-piston micromirror with high fill factor and small tilt and lateral shift," *Sensors and Actuators, A: Physical*, vol. 167, no. 2, pp. 495–501, 2011.

[149] S. Gu-Stoppel, J. Janes, D. Kaden, H. J. Quenzer, U. Hofmann, and W. Benecke, "Piezoelectric resonant micromirror with high frequency and large deflection applying mechanical leverage amplification," *Micromachining and Microfabrication Process Technology XVIII, February 5, 2013 - February 7, 2013*, vol. 8612, pp. The Society of Photo–Optical Instrumentation Engineers, 2013.

[150] H. Lei, Q. Wen, F. Yu, D. Li, Z. Shang, J. Huang, and Z. Wen, "AlN film based piezoelectric large-aperture MEMS scanning micromirror integrated with angle sensors," *Journal of Micromechanics and Microengineering*, vol. 28, no. 11, 2018.

[151] M. D. Williams, B. A. Griffin, T. N. Reagan, J. R. Underbrink, and M. Sheplak, "An AlN MEMS piezoelectric microphone for aeroacoustic applications," *Journal of Microelectromechanical Systems*, vol. 21, no. 2, pp. 270–283, 2012.

[152] S. C. Minne, S. R. Manalis, and C. F. Quate, "Parallel atomic force microscopy using cantilevers with integrated piezoresistive sensors and integrated piezoelectric actuators," *Applied Physics Letters*, vol. 67, no. 1995, p. 3918, 1995.

[153] C.-B. Eom and S. Trolier-McKinstry, "Thin-film piezoelectric MEMS," *MRS Bulletin*, vol. 37, pp. 1007–1017, nov 2012.

[154] S. Tadigadapa and K. Mateti, "Piezoelectric MEMS sensors: State-of-the-art and perspectives," *Measurement Science and Technology*, vol. 20, no. 9, p. 092001, 2009.

[155] A. D. Yalcinkaya, H. Urey, D. Brown, T. Montague, and R. Sprague, "Two-axis electromagnetic microscanner for high resolution displays," *Journal of Microelectromechanical Systems*, vol. 15, no. 4, pp. 786–794, 2006.

[156] A. Arslan, D. Brown, W. O. Davis, S. Holmström, S. K. Gokce, and H. Urey, "Comb-actuated resonant torsional microscanner with mechanical amplification," *Journal of Microelectromechanical Systems*, vol. 19, no. 4, pp. 936–943, 2010.

[157] W. T. Ang, P. K. Khosla, and C. N. Riviere, "Feedforward controller with inverse rate-dependent model for piezoelectric actuators in trajectory-tracking applica-

tions," *IEEE/ASME Transactions on Mechatronics*, vol. 12, no. 2, pp. 134–142, 2007.

[158] Y. Cao and X. B. Chen, "A novel discrete arma-based model for piezoelectric actuator hysteresis," *IEEE/ASME Transactions on Mechatronics*, vol. 17, no. 4, pp. 737–744, 2012.

[159] T. Fujita, K. Maenaka, and Y. Takayama, "Dual-axis MEMS mirror for large deflection-angle using SU-8 soft torsion beam," *Sensors and Actuators, A: Physical*, vol. 121, no. 1, pp. 16–21, 2005.

[160] H. Urey, D. W. Wine, and T. D. Osborn, "Optical performance requirements for mems-scanner-based microdisplays," in *MOEMS and Miniaturized Systems*, vol. 4178, pp. 176–185, International Society for Optics and Photonics, 2000.

[161] R. G. Polcawich and J. S. Pulskamp, *Additive Processes for Piezoelectric Materials: Piezoelectric MEMS*, pp. 273–353. Boston, MA: Springer US, 2011.

[162] M. A. Dubois and P. Muralt, "Measurement of the effective transverse piezoelectric coefficient e31,f of AlN and Pb(Zrx,Ti1-x)O3 thin films," *Sensors and Actuators, A: Physical*, vol. 77, no. 2, pp. 106–112, 1999.

[163] K. Lefki and G. J. Dormans, "Measurement of piezoelectric coefficients of ferroelectric thin films," *Journal of Applied Physics*, vol. 76, no. 3, pp. 1764–1767, 1994.

[164] J. F. Domke, C. H. Rhee, Z. Liu, T. D. Wang, and K. R. Oldham, "Amplifying transmission and compact suspension for a low-profile, large-displacement piezoelectric actuator," *Journal of Micromechanics and Microengineering*, vol. 21, no. 6, p. 067004, 2011.

[165] K. E. Wojciechowski, R. H. Olsson, C. D. Nordquist, and M. R. Tuck, "Super high frequency width extensional aluminum nitride (AlN) MEMS resonators," *Proceedings - IEEE Ultrasonics Symposium*, pp. 1179–1182, 2009.

[166] H. Chandrahalim, S. A. Bhave, R. Polcawich, J. Pulskamp, D. Judy, R. Kaul, and M. Dubey, "Influence of silicon on quality factor, motional impedance and tuning range of pzt-transduced resonators," *Technical Digest - Solid-State Sensors, Actuators, and Microsystems Workshop*, pp. 360–363, 2008.

[167] H. C. Lee, J. H. Park, J. Y. Park, H. J. Nam, and J. U. Bu, "Design, fabrication and RF performances of two different types of piezoelectrically actuated Ohmic MEMS switches," *Journal of Micromechanics and Microengineering*, vol. 15, no. 11, pp. 2098–2104, 2005.

[168] P. Muralt, A. Kholkin, M. Kohli, and T. Maeder, "Piezoelectric actuation of PZT thin-film diaphragms at static and resonant conditions," *Sensors and Actuators, A: Physical*, vol. 53, no. 1-3, pp. 398–404, 1996.

[169] R. Ruby and P. Merchant, "Micromachined thin film bulk acoustic resonators," in *Proceedings of IEEE 48th Annual Symposium on Frequency Control*, pp. 135–138, IEEE, 1994.

[170] G. Wingqvist, "AlN-based sputter-deposited shear mode thin film bulk acoustic resonator (FBAR) for biosensor applications - A review," *Surface and Coatings Technology*, vol. 205, no. 5, pp. 1279–1286, 2010.

[171] K. Wasa, T. Matsushima, H. Adachi, I. Kanno, and H. Kotera, "Thin-film piezoelectric materials for a better energy harvesting MEMS," *Journal of Microelectromechanical Systems*, vol. 21, no. 2, pp. 451–457, 2012.

[172] S. Strite, "GaN, AlN, and InN: A review," *Journal of Vacuum Science & Technology B: Microelectronics and Nanometer Structures*, vol. 10, no. 4, p. 1237, 1992.

[173] G. A. Slack, R. A. Tanzilli, R. O. Pohl, and J. W. Vandersande, "The intrinsic thermal conductivity of AIN," *Journal of Physics and Chemistry of Solids*, vol. 48, no. 7, pp. 641–647, 1987.

[174] I. Yonenaga, "Hardness of bulk single-crystal GaN and AlN," *MRS Internet Journal of Nitride Semiconductor Research*, vol. 7, p. e6, jun 2002.

[175] K. Tonisch, V. Cimalla, C. Foerster, H. Romanus, O. Ambacher, and D. Dontsov, "Piezoelectric properties of polycrystalline AlN thin films for MEMS application," *Sensors and Actuators, A: Physical*, vol. 132, no. 2, pp. 658–663, 2006.

[176] V. Mortet, M. Nesladek, K. Haenen, A. Morel, M. D'Olieslaeger, and M. Vanecek, "Physical properties of polycrystalline aluminium nitride films deposited by magnetron sputtering," *Diamond and Related Materials*, vol. 13, no. 4-8, pp. 1120–1124, 2004.

[177] Q. Chen, L. Qin, and Q. M. Wang, "Property characterization of AlN thin films in composite resonator structure," *Journal of Applied Physics*, vol. 101, no. 8, 2007.

[178] J. F. Shepard, P. J. Moses, and S. Trolier-McKinstry, "The wafer flexure technique for the determination of the transverse piezoelectric coefficient (d31) of PZT thin films," *Sensors and Actuators, A: Physical*, vol. 71, no. 1-2, pp. 133–138, 1998.

[179] D. Chen, J. Wang, D. Xu, and Y. Zhang, "The influence of the AlN film texture on the wet chemical etching," *Microelectronics Journal*, vol. 40, no. 1, pp. 15–19, 2009.

[180] S. J. Pearton, C. R. Abernathy, F. Ren, J. R. Lothian, P. W. Wisk, A. Katz, and C. Constantine, "Dry etching of thin-film InN, AlN and GaN," *Semiconductor Science and Technology*, vol. 8, no. 2, pp. 310–312, 1993.

[181] M. A. Dubois and P. Muralt, "Stress and piezoelectric properties of aluminum nitride thin films deposited onto metal electrodes by pulsed direct current reactive sputtering," *Journal of Applied Physics*, vol. 89, no. 11 I, pp. 6389–6395, 2001.

[182] R. Maas, M. Koch, N. R. Harris, N. M. White, and A. G. Evans, "Thick-film printing of PZT onto silicon," *Materials Letters*, vol. 31, no. 1-2, pp. 109–112, 1997.

[183] R. Bouregba, G. Poullain, B. Vilquin, and H. Murray, "Orientation control of textured PZT thin films sputtered on silicon substrate with TiOx seeding," *Materials Research Bulletin*, vol. 35, pp. 1381–1390, jul 2000.

[184] L. E. McNeil, M. Grimsditch, and R. H. French, "Vibrational Spectroscopy of Aluminum Nitride," *Journal of the American Ceramic Society*, vol. 76, no. 5, pp. 1132–1136, 1993.

[185] J. J. Hall, "Electronic effects in the elastic constants of n-type silicon," *Physical Review*, vol. 161, no. 3, pp. 756–761, 1967.

[186] A. Cowen, G. Hames, K. Glukh, and B. Hardy, *PiezoMUMPS design handbook*. MEMSCAP Inc., Crolles, France, 2014.

[187] P. Castellini, M. Martarelli, and E. P. Tomasini, "Laser doppler vibrometry: Development of advanced solutions answering to technology's needs," *Mechanical systems and signal processing*, vol. 20, no. 6, pp. 1265–1285, 2006.

[188] J. C. Wyant, "White light interferometry," in *Holography: a tribute to yuri denisyuk and emmett leith*, vol. 4737, pp. 98–107, International Society for Optics and Photonics, 2002.

[189] R. Conant, J. Nee, K. Lau, and R. Muller, "Dynamic deformation of scanning mirrors," in *2000 IEEE/LEOS International Conference on Optical MEMS (Cat. No.00EX399)*, pp. 49–50, 2000.

[190] P. Chen, I. W. Jung, D. A. Walko, Z. Li, Y. Gao, G. K. Shenoy, D. López, and J. Wang, "Ultrafast photonic micro-systems to manipulate hard X-rays at 300 picoseconds," *Nature Communications*, vol. 10, no. 1, p. 1158, 2019.

[191] J. I. Lee, P. Sunwoo, E. Youngkee, J. Bongwon, and J. Kim, "Resonant frequency tuning of torsional microscanner by mechanical restriction using MEMS actuator," *Proceedings of the IEEE International Conference on Micro Electro Mechanical Systems (MEMS)*, no. c, pp. 164–167, 2009.

[192] M. A. Hopcroft, W. D. Nix, and T. W. Kenny, "What is the Young's modulus of silicon?," *Journal of Microelectromechanical Systems*, vol. 19, no. 2, pp. 229–238, 2010.

[193] P. B. Johnson and R. W. Christy, "Optical Constants of the Noble Metals," *Physical Review B*, vol. 6, pp. 4370–4379, dec 1972.

[194] L. Herdly, P. Janin, R. Bauer, and S. van de Linde, "Tunable Wide-Field Illumination and Single-Molecule Photoswitching with a Single MEMS Mirror," *ACS Photonics*, vol. 8, no. 9, pp. 2728–2736, 2021.

[195] Melcor, *Thermoelectric cooler*. Rev 1.01. Retrieved from `https://docs.rs-online.com/89b3/0900766b8048566d.pdf` on 05/03/2022.

[196] T. Inc., "Mounted achromatic doublets, ar coated: 400 - 700 nm." `https://www.thorlabs.com/newgrouppage9.cfm?objectgroup_id=2696`. Retrieved on 07/03/2022.

[197] H. Piller, *Microscope photometry*. Springer Science & Business Media, 2012.

[198] P. W. Tinning, R. Scrimgeour, and G. McConnell, "Widefield standing wave microscopy of red blood cell membrane morphology with high temporal resolution," *Biomed. Opt. Express*, vol. 9, pp. 1745–1761, Apr 2018.

[199] S. Prahl, "Fluorescein." `https://omlc.org/spectra/PhotochemCAD/html/037.html`, 2017. Retrieved on 22/06/2021.

[200] C. C. Tsai, Z. H. Li, Y. T. Lin, and M. S. Lu, "A Closed-Loop Controlled CMOS MEMS Biaxial Scanning Mirror for Projection Displays," *IEEE Sensors Journal*, vol. 20, no. 1, pp. 242–249, 2020.

[201] Q. A. A. Tanguy, O. Gaiffe, N. Passilly, J.-M. Cote, G. Cabodevila, S. Bargiel, P. Lutz, H. Xie, and C. Gorecki, "Real-time Lissajous imaging with a low-voltage 2-axis MEMS scanner based on electrothermal actuation," *Optics Express*, vol. 28, no. 6, p. 8512, 2020.

[202] J. Y. Kim, C. Lee, K. Park, G. Lim, and C. Kim, "Fast optical-resolution photoacoustic microscopy using a 2-axis water-proofing MEMS scanner," *Scientific Reports*, vol. 5, p. 7932, jul 2015.

[203] N. Kanopoulos, N. Vasanthavada, and R. L. Baker, "Design of an image edge detection filter using the sobel operator," *IEEE Journal of solid-state circuits*, vol. 23, no. 2, pp. 358–367, 1988.

[204] S. Zhang, J. Chen, C. Liu, S. Zhou, M. Loy, G. K. L. Wong, and S. Du, "A dark-line two-dimensional magneto-optical trap of 85rb atoms with high optical depth," *Review of Scientific Instruments*, vol. 83, no. 7, p. 073102, 2012.

[205] D. A. Steck, "Rubidium 87 d line data." `http://steck.us/alkalidata`, 2021. revision 2.2.2, 9 July 2021.

[206] H. Urey, S. Holmstrom, U. Baran, K. Aksit, M. K. Hedili, and O. Eides, "Mems scanners and emerging 3d and interactive augmented reality display applications," *2013 Transducers and Eurosensors XXVII: The 17th International Conference on Solid-State Sensors, Actuators and Microsystems, TRANSDUCERS and EUROSENSORS 2013*, pp. 2485–2488, 2013.

[207] J. G. Smits, K. Fujimoto, and V. F. Kleptsyn, "Microelectromechanical flexure pzt actuated optical scanner: Static and resonance behavior," *Journal of Micromechanics and Microengineering*, vol. 15, pp. 1285–1293, 6 2005.

[208] F. Filhol, E. Defay, C. Divoux, C. Zinck, and M.-T. Delaye, "Resonant micromirror excited by a thin-film piezoelectric actuator for fast optical beam scanning," *Sensors and Actuators A: Physical*, vol. 123, pp. 483–489, 2005.

[209] T. Naono, T. Fujii, M. Esashi, and S. Tanaka, "A large-scan-angle piezoelectric mems optical scanner actuated by a nb-doped pzt thin film," *Journal of Micromechanics and Microengineering*, vol. 24, 1 2014.

[210] F. Senger, T. von Wantoch, C. Mallas, J. Janes, U. Hofmann, B. Wagner, and W. Benecke, "Mems scanning mirrors for high power laser display and lighting applications," in *The 4th Laser Display and Lighting Conference (LDC'15)*, 2015.

[211] Ç. Ataman, S. Lani, W. Noell, and N. De Rooij, "A dual-axis pointing mirror with moving-magnet actuation," *Journal of Micromechanics and Microengineering*, vol. 23, no. 2, p. 025002, 2012.

[212] T. Iseki, M. Okumura, and T. Sugawara, "Shrinking design of a mems optical scanner having four torsion beams and arms," *Sensors and Actuators A: Physical*, vol. 164, no. 1-2, pp. 95–106, 2010.

[213] J.-H. Park, J. Akedo, and H. Sato, "High-speed metal-based optical microscanners using stainless-steel substrate and piezoelectric thick films prepared by aerosol deposition method," *Sensors and Actuators A: Physical*, vol. 135, no. 1, pp. 86–91, 2007.

[214] G. Römer and P. Bechtold, "Electro-optic and acousto-optic laser beam scanners," *Physics Procedia*, vol. 56, pp. 29–39, 2014. 8th International Conference on Laser Assisted Net Shape Engineering LANE 2014.

[215] V. B. Voloshinov, N. Gupta, G. A. Knyazev, and N. V. Polikarpova, "An acousto-optic x-y deflector based on close-to-axis propagation of light in the single te crystal," *Journal of Optics*, vol. 13, p. 015706, 2011.

[216] S. N. Antonov, "Acousto-optic deflector: A new method to increase the efficiency and bandwidth," *Technical Physics*, vol. 61, pp. 1597–1601, 10 2016.

[217] A. Paterson, R. Bauer, L. Li, W. Lubeigt, and D. Uttamchandani, "Range extension of a bimorph varifocal micromirror through actuation by a peltier element," *IEEE Journal of Selected Topics in Quantum Electronics*, vol. 21, no. 4, pp. 72–78, 2015.

[218] L. Li, R. Li, W. Lubeigt, and D. Uttamchandani, "Design, simulation, and characterization of a bimorph varifocal micromirror and its application in an optical imaging system," *Journal of Microelectromechanical Systems*, vol. 22, no. 2, pp. 285–294, 2013.

[219] P. Janin, R. Bauer, P. Griffin, E. Riis, and D. Uttamchandani, "Characterization of a fast piezoelectric varifocal mems mirror," in *2018 International Conference on Optical MEMS and Nanophotonics (OMN)*, pp. 1–5, 2018.

[220] S. Olmschenk, K. C. Younge, D. L. Moehring, D. N. Matsukevich, P. Maunz, and C. Monroe, "Manipulation and detection of a trapped yb^+ hyperfine qubit," *Phys. Rev. A*, vol. 76, p. 052314, Nov 2007.

[221] D. A. Steck, "Sodium d line data." `http://steck.us/alkalidata`, 2021. revision 2.2.1, 21 November 2021.

[222] J. Schwiegerling, J. E. Greivenkamp, and J. M. Miller, "Representation of videokeratoscopic height data with zernike polynomials," *JOSA A*, vol. 12, no. 10, pp. 2105–2113, 1995.

[223] M. Oleszko and H. Gross, "Analysis of freeform mirror systems based on the decomposition of the total wave aberration into zernike surface contributions," *Applied Optics*, vol. 57, no. 9, pp. 1998–2006, 2018.

[224] V. Lakshminarayanan and A. Fleck, "Zernike polynomials: A guide," *Journal of Modern Optics*, vol. 58, no. 7, pp. 545–561, 2011.

[225] M. Born and E. Wolf, *Principles of optics: electromagnetic theory of propagation, interference and diffraction of light*. CUP Archive, 2000.

[226] R. Navarro, J. Arines, and R. Rivera, "Direct and inverse discrete Zernike transform," *Optics Express*, vol. 17, no. 26, p. 24269, 2009.

[227] M. Ares and S. Royo, "Comparison of cubic B-spline and Zernike-fitting techniques in complex wavefront reconstruction," *Applied Optics*, vol. 45, no. 27, pp. 6954–6964, 2006.

[228] L. N. Thibos, R. A. Applegate, J. T. Schwiegerling, and R. Webb, "Standards for reporting the optical aberrations of eyes," *Journal of Refractive Surgery*, vol. 18, no. 5, pp. 652–660, 2002.

[229] P. Fricker, "Analyzing lasik optical data using zernike functions." https://uk.mathworks.com/company/newsletters/articles/analyzing-lasik-optical-data-using-zernike-functions.html, 2008. Retrieved on 10/06/2021.

[230] MathWorks, ""mldivide, '\'" in matlab documentation." https://uk.mathworks.com/help/matlab/ref/mldivide.html, 2021. Retrieved on 10/06/2021.

List of publications

The following references were published during the course of this project and contain some of the work presented here.

- P. Janin, R. Bauer, P. Griffin, E. Riis, and D. Uttamchandani, "Characterization of a fast piezoelectric varifocal mems mirror," in *2018 International Conference on Optical MEMS and Nanophotonics (OMN)*, pp. 1–5, 2018.

- P. Janin, R. Bauer, P. Griffin, E. Riis, and D. Uttamchandani, "Fast piezoelectric scanning MEMS mirror for 1D ion addressing," in *2019 International Conference on Optical MEMS and Nanophotonics (OMN)*, pp. 220–221, 2019.

- P. Janin, R. Bauer, P. Griffin, E. Riis, and D. Uttamchandani, "A high-frequency tunable piezoelectric MEMS scanner for fast addressing applications," in *2021 IEEE 34th International Conference on Micro Electro Mechanical Systems (MEMS)*, pp. 294–297, 2021.

- L. Herdly, P. Janin, R. Bauer, P. Griffin, and S. van de Linde, "Tuneable wide-field illumination and single-molecule photoswitching with a single MEMS mirror," *ACS Photonics*, vol. 8, n. 9, pp. 2728–2736, 2021.

Appendix A

List of simulated scanner modes

In addition to the three out-of-plane scanning modes studied throughout the characterisation process, the finite element simulation produced additional modes for the MEMS mechanical structure. They are given on Fig. A.1 below, for the non-tunable design with a plate diameter of 200 µm. Of those modes, only the first 5 fell within the characterisation range of 10-410 kHz and were observed for the fabricated scanners.

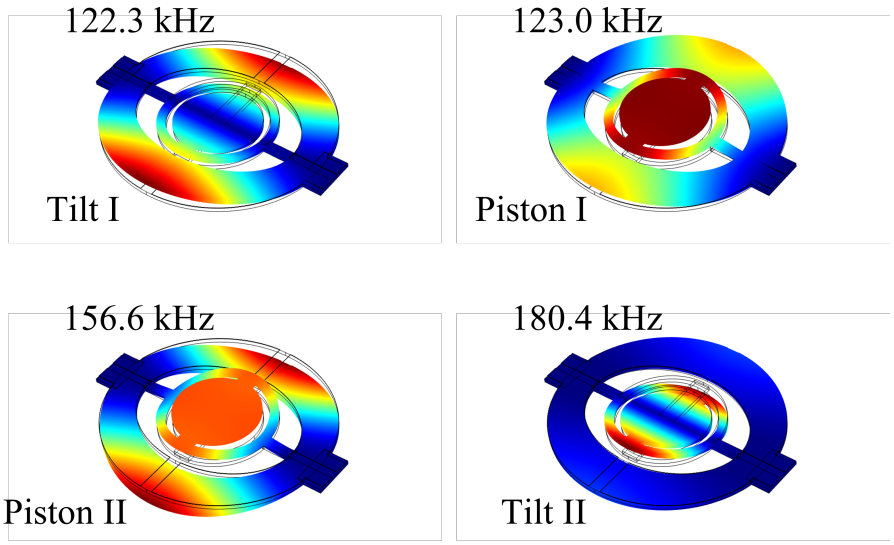

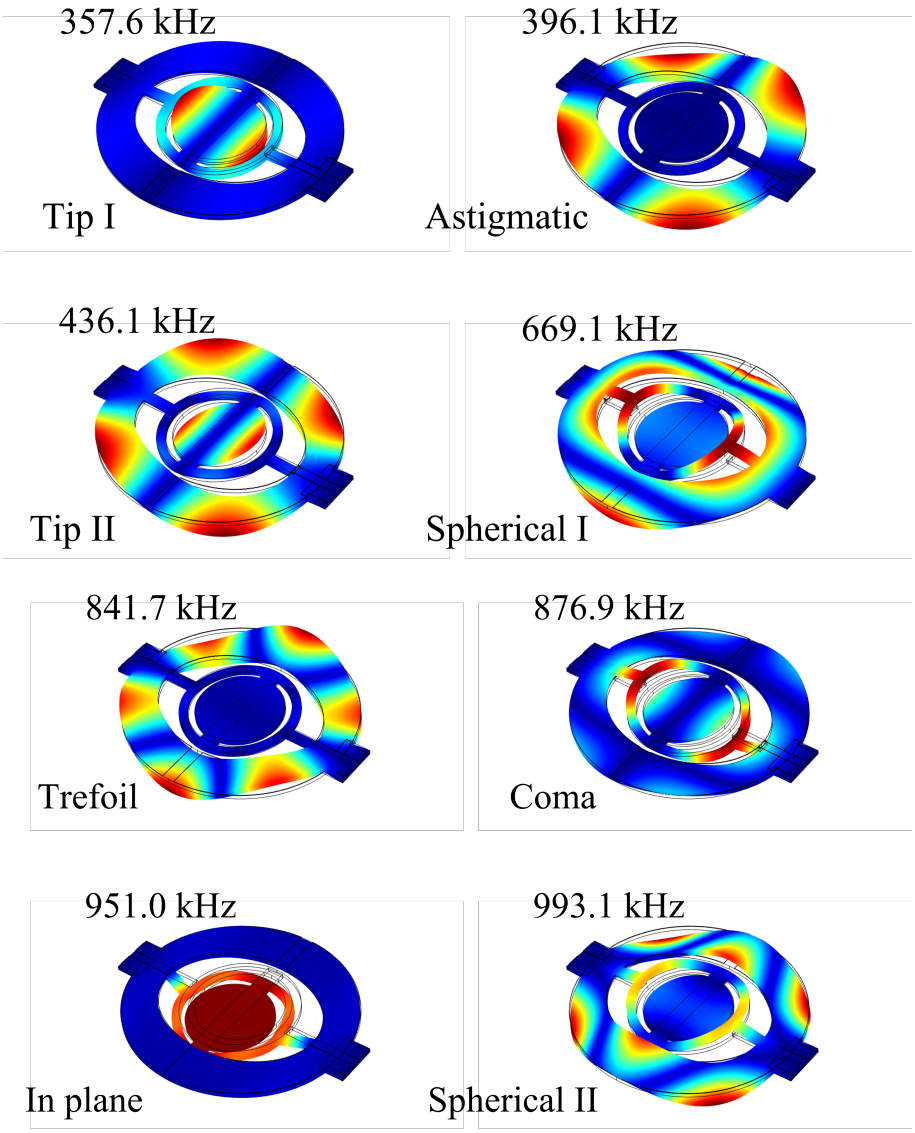

Figure A.1: Illustration of the 12 mode shapes for eigenfrequencies above 100 kHz, with the corresponding nomenclature. Simulated using COMSOL Multiphysics 5.2.

Appendix B

Mathematical details of Lissajous grid addressing

The frequency difference between two scanners can be exploited for 2D scanning : the point addressed by such unsynchronized scanners in a 2D configuration will move along a Lissajous curve, with a cycle frequency equal to the gcd of the scanner frequencies. The curve length (and thus addressing point density) inside the maximal 2D addressing range depends on the gcd as well : a greater gcd means a faster, but shorter curve.

The investigation of the differences in the mirrors resonance frequencies led to an interesting point : for a high enough scanning frequency to gcd ratio, the cuve crosses itself along its path, with the crossing points organised in a grid-like pattern. This is particularly interesting for our desired application : if a target grid was aligned with the curve's crossing point, the effective addressing frequency for one point would be double that of the Lissajous scan. An example of such a curve is shown on Fig.B.1, for $f_1 = 336$ kHz and $f_2 = 342$ kHz.

In order to take advantage of this pattern, we need to determine the position of the crossing points depending on the scanner frequencies. Assuming zero starting phase between the actuators initially, this can be done analytically by solving the following problem :

For two distinct, strictly positive integers f_1 and f_2, find the loci of the crossing points

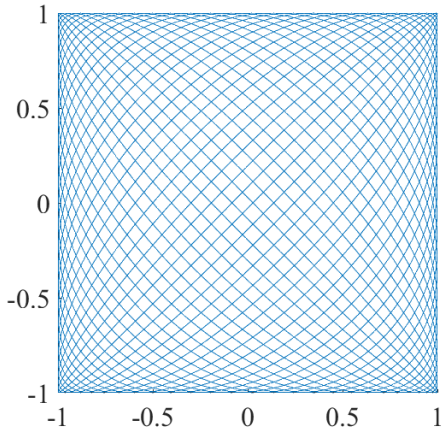

Figure B.1: Example of a Lissajous pattern with $f_1 = 336,\ f_2 = 342,\ \phi = 0$.

of the parametric curve defined as

$$\begin{cases} x(t) &= \cos(2\pi f_1 t) \\ y(t) &= \sin(2\pi f_2 t) \end{cases} \quad \text{for } t \in \mathbb{R}_+ \tag{B.1}$$

This is immediately equivalent to finding the real solutions of the coupled equation system

$$\begin{cases} \cos(2\pi f_1 t) &= \cos(2\pi f_1 t') \\ \sin(2\pi f_2 t) &= \sin(2\pi f_2 t') \end{cases} \quad \text{for } t, t' \in \left[0, \frac{1}{f_1 \wedge f_2}\right[\text{ and } t \neq t' \tag{B.2}$$

where $f_1 \wedge f_2$ is the gcd of f_1 and f_2. It follows

$$\begin{cases} 2\pi f_1 t &= \pm 2\pi f_1 t' + 2k_1\pi \\ 2\pi f_2 t &= 2\pi f_2 t' + 2k_2\pi \text{ or } \pi - 2\pi f_2 t' + 2k_2\pi \end{cases} \tag{B.3}$$

$$\text{with } t, t' \in \left[0, \tfrac{1}{f_1 \wedge f_2}\right[\,, t \neq t',\ k_1, k_2 \in \mathbb{Z}^*$$

which gives four distinct cases. Let us examine them independently

Case 1.

$$\begin{cases} 2\pi f_1 t &= 2\pi f_1 t' + 2k_1\pi \\ 2\pi f_2 t &= 2\pi f_2 t' + 2k_2\pi \end{cases} \quad k_1, k_2 \in \mathbb{Z}^* \tag{B.4}$$

dividing by 2π and rearranging gives

$$\left\{\begin{array}{rcl} f_1(t-t') & = & k_1 \\ f_2(t-t') & = & k_2 \end{array}\right. \Leftrightarrow \left\{\begin{array}{rcl} t-t' & = & \frac{k_1}{f_1} \\ f_2k_1 - k_2f_1 & = & 0 \end{array}\right. \tag{B.5}$$

Rearranging the second line, we get

$$\frac{f_2}{f_1} = \frac{k_2}{k_1} \Leftrightarrow \exists\, a \in \mathbb{Z}^*,\ k_2 = \frac{a}{f_1 \wedge f_2} f_2 \ \&\ k_1 = \frac{a}{f_1 \wedge f_2} f_1 \tag{B.6}$$

Substituting the value of k_1, the first line of B.5 gives

$$t - t' = \frac{a}{f_1 \wedge f_2}, \quad a \in \mathbb{Z} \tag{B.7}$$

and since $t \neq t'$, we have $a \neq 0$. However :

$$0 \leq t < \frac{1}{f_1 \wedge f_2} \quad \text{and} \quad -\frac{1}{f_1 \wedge f_2} < -t' \leq 0 \tag{B.8}$$

It follows

$$-\frac{1}{f_1 \wedge f_2} < t - t' < \frac{1}{f_1 \wedge f_2} \tag{B.9}$$

and thus $-1 < a < 1$. Since $a \in \mathbb{Z}^*$, no solutions exist for case 1.

Case 2.

$$\left\{\begin{array}{rcl} 2\pi f_1 t & = & -2\pi f_1 t' + 2k_1\pi \\ 2\pi f_2 t & = & 2\pi f_2 t' + 2k_2\pi \end{array}\right. \quad k_1, k_2 \in \mathbb{Z} \tag{B.10}$$

Rearranging as previously :

$$\left\{\begin{array}{rcl} f_1(t+t') & = & k_1 \\ f_2(t-t') & = & k_2 \end{array}\right. \tag{B.11}$$

adding the first line multiplied by f_2/f_1 to the second line gives

$$\left\{\begin{array}{rcl} f_1(t+t') & = & k_1 \\ 2f_2 t & = & \frac{f_2}{f_1}k_1 + k_2 \end{array}\right. \tag{B.12}$$

$$\begin{cases} f_1(t+t') &= k_1 \\ 2t &= \frac{k_1}{f_1} + \frac{k_2}{f_2} \end{cases} \tag{B.13}$$

and finally

$$\begin{cases} t &= \frac{1}{2}(\frac{k_1}{f_1} + \frac{k_2}{f_2}) \\ t' &= \frac{1}{2}(\frac{k_1}{f_1} - \frac{k_2}{f_2}) \end{cases} \tag{B.14}$$

t and t' must also satisfy $t, t' \in \left[0, \frac{1}{f_1 \wedge f_2}\right[$, which imposes additional constraints on the choice of k_1 and k_2 :

$$\frac{k_1}{f_1} = t + t' \Leftrightarrow 0 \leq k_1 < 2\frac{f_1}{f_1 \wedge f_2} \tag{B.15}$$

$$\frac{k_2}{f_2} = t - t' \Leftrightarrow -\frac{f_2}{f_1 \wedge f_2} < k_2 < \frac{f_2}{f_1 \wedge f_2} \tag{B.16}$$

$$\text{and } 0 \leq \frac{k_1}{f_1} \pm \frac{k_2}{f_2} < \frac{2}{f_1 \wedge f_2} \tag{B.17}$$

Case 3.

$$\begin{cases} 2\pi f_1 t &= 2\pi f_1 t' + 2k_1\pi \\ 2\pi f_2 t &= \pi - 2\pi f_2 t' + 2k_2\pi \end{cases} \qquad k_1, k_2 \in \mathbb{Z} \tag{B.18}$$

Rearranging similarly to case 2 gives

$$\begin{cases} t - t' &= \frac{k_1}{f_1} \\ t + t' &= \frac{k_2}{f_2} + \frac{1}{2f_2} \end{cases} \tag{B.19}$$

and then

$$\begin{cases} t &= \frac{1}{2}(\frac{k_1}{f_1} + \frac{k_2}{f_2}) + \frac{1}{4f_2} \\ t' &= \frac{1}{2}(-\frac{k_1}{f_1} + \frac{k_2}{f_2}) + \frac{1}{4f_2} \end{cases} \tag{B.20}$$

with the time boundary conditions

$$-\frac{f_1}{f_1 \wedge f_2} < k_1 < \frac{f_2}{f_1 \wedge f_2} \tag{B.21}$$

$$-\frac{1}{2} \leq k_2 < \frac{2f_2}{f_1 \wedge f_2} - \frac{1}{2} \tag{B.22}$$

$$\text{and } -\frac{1}{2f_2} \leq \pm\frac{k_1}{f_1} + \frac{k_2}{f_2} < \frac{2}{f_1 \wedge f_2} - \frac{1}{2f_2} \tag{B.23}$$

Case 4.

$$\begin{cases} 2\pi f_1 t &= -2\pi f_1 t' + 2k_1\pi \\ 2\pi f_2 t &= \pi - 2\pi f_2 t' + 2k_2\pi \end{cases} \qquad k_1, k_2 \in \mathbb{Z} \tag{B.24}$$

Rearranging gives

$$\begin{cases} f_1(t+t') &= k_1 \\ f_2(t+t') &= \frac{1}{2} + k_2 \end{cases} \tag{B.25}$$

This implies

$$\frac{k_1}{f_1} = \frac{1}{2f_2} + \frac{k_2}{f_2} \Leftrightarrow k_1 f_2 - k_2 f_1 = \frac{f_1}{2} \tag{B.26}$$

$$\Leftrightarrow \frac{k_1 f_2}{f_1 \wedge f_2} - \frac{k_2 f_1}{f_1 \wedge f_2} = \frac{1}{2} \times \frac{f_1}{f_1 \wedge f_2} \tag{B.27}$$

Since the left member of eq. B.27 is an integer, it follows

$$\frac{1}{2} \times \frac{f_1}{f_1 \wedge f_2} \in \mathbb{Z} \Rightarrow \exists a \in \mathbb{N}^*, f_1 = 2a \times f_1 \wedge f_2 \tag{B.28}$$

The final assertion of eq. B.28 is thus a necessary condition for solutions to case 4 to exist.

Eq. B.26 also gives

$$k_1 = \frac{f_1}{2f_2} + \frac{f_1}{f_2} k_2 = \frac{f_1 + 2f_1 k_2}{2f_2} \in \mathbb{Z}^* \tag{B.29}$$

Which is equivalent to

$$\exists b \in \mathbb{Z}^*, \quad f_1 + 2f_1 k_2 = 2bf_2 \tag{B.30}$$

$$\Leftrightarrow \exists b \in \mathbb{Z}^*, \quad a(f_1 \wedge f_2)(1 + 2k_2) = bf_2 \tag{B.31}$$

using eq. B.28. Consequently

$$k_2 = \frac{1}{2}\frac{b}{a}\frac{f_2}{f_1 \wedge f_2} - \frac{1}{2} \qquad a, b \in \mathbb{Z} \tag{B.32}$$

then

$$k_2 \in \mathbb{Z} \Leftrightarrow \frac{b}{a}\frac{f_2}{f_1 \wedge f_2} \text{ is an odd integer.} \tag{B.33}$$

Since 2 and a are dividers of $f_1/(f_1 \wedge f_2)$, both must be prime with $f_2/(f_1 \wedge f_2)$. As a consequence, $f_2/(f_1 \wedge f_2)$ is odd, and a must divide b so that the right member of assertion B.33 is an integer. Thus

$$\exists c \in \mathbb{Z}, k_2 = \frac{2c+1}{2}\frac{f_2}{f_1 \wedge f_2} - \frac{1}{2} \tag{B.34}$$

The second line of eq. B.25 gives

$$k_2 = f_2(t + t') - \frac{1}{2} \tag{B.35}$$

And since $t, t' \in \left[0, \frac{1}{f_1 \wedge f_2}\right[$:

$$0 \leq f_2(t + t') - \frac{1}{2} < \frac{2f_2}{f_1 \wedge f_2} - \frac{1}{2} \tag{B.36}$$

$$0 \leq \frac{2c+1}{2}\frac{f_2}{f_1 \wedge f_2} - \frac{1}{2} < \frac{2f_2}{f_1 \wedge f_2} - \frac{1}{2} \tag{B.37}$$

$$0 \leq 2c + 1 < 4 \tag{B.38}$$

Since $c \in \mathbb{Z}$, it follows $c = 0$ or $c = 1$. Finally

$$k_2 = \frac{1}{2}\frac{f_2}{f_1 \wedge f_2} - \frac{1}{2} \quad \text{or} \quad k_2 = \frac{3}{2}\frac{f_2}{f_1 \wedge f_2} - \frac{1}{2} \tag{B.39}$$

Furthermore, we get from eq. B.26

$$k_1 = \frac{f_1}{2f_2} + \frac{f_1}{f_2}k_2 \tag{B.40}$$

$$= \frac{f_1}{2f_2} + \frac{1}{2}\frac{f_1}{f_1 \wedge f_2} - \frac{f_1}{2f_2} \quad \text{or} \quad \frac{f_1}{2f_2} + \frac{3}{2}\frac{f_1}{f_1 \wedge f_2} - \frac{f_1}{2f_2} \tag{B.41}$$

$$= \frac{1}{2}\frac{f_1}{f_1 \wedge f_2} \quad \text{or} \quad \frac{3}{2}\frac{f_1}{f_1 \wedge f_2} \tag{B.42}$$

And since $t' = \frac{k_1}{f_1} - t$ (eq. B.25) :

$$t' = \frac{1}{2}\frac{1}{f_1 \wedge f_2} - t \quad \text{or} \quad \frac{3}{2}\frac{1}{f_1 \wedge f_2} - t \tag{B.43}$$

Remembering $t, t' \in \left[0, \frac{1}{f_1 \wedge f_2}\right[$:

$$\frac{1}{2}\frac{1}{f_1 \wedge f_2} \geq \frac{1}{2}\frac{1}{f_1 \wedge f_2} - t \geq 0 \qquad \text{for } t \in \left[0, \frac{1}{2}\frac{f_1}{f_1 \wedge f_2}\right] \tag{B.44}$$

$$\frac{1}{f_1 \wedge f_2} > \frac{3}{2}\frac{1}{f_1 \wedge f_2} - t > \frac{1}{2}\frac{1}{f_1 \wedge f_2} \qquad \text{for } t \in \left]\frac{1}{2}\frac{f_1}{f_1 \wedge f_2}, \frac{f_1}{f_1 \wedge f_2}\right[\tag{B.45}$$

this imposes $c = 0$ or $c = 1$ depending on the value of t and finally

$$t' = \frac{1}{2}\frac{1}{f_1 \wedge f_2} - t \qquad \text{for } t \in \left[0, \frac{1}{2}\frac{f_1}{f_1 \wedge f_2}\right] \tag{B.46}$$

$$t' = \frac{3}{2}\frac{1}{f_1 \wedge f_2} - t \qquad \text{for } t \in \left]\frac{1}{2}\frac{f_1}{f_1 \wedge f_2}, \frac{f_1}{f_1 \wedge f_2}\right[\tag{B.47}$$

It is then trivial to verify that those values of t', with the above condition on f_1 and the values found for k_1 and k_2, satisfy eq. B.24 for any value of t in the interval, completing the synthesis of solutions. In that case, the curve covers the same path twice upon a single period and every crossing point is visited four times.

Conclusion For any values of f_1 and f_2 in $\mathbb{N}^*$, the loci of the crossing points are at all the values of t in $\left[0, \frac{1}{f_1 \wedge f_2}\right[$ of the form :

- $t = \frac{1}{2}(\frac{k_1}{f_1} + \frac{k_2}{f_2})$, for any values of $k_1, k_2 \in \mathbb{Z}^*$ such that $t' = t - \frac{k_2}{f_2}$ is also in the period interval;
- $t = \frac{1}{2}(\frac{k_1}{f_1} + \frac{k_2}{f_2}) + \frac{1}{4f_2}$, for any values of $k_1, k_2 \in \mathbb{Z}^*$ such that $t' = t - \frac{k_1}{f_1}$ is also in the period interval;
- additionally, if and only if f_1 satisfies $\exists a \in \mathbb{N}^*, f_1 = 2a \times f_1 \wedge f_2$, the curve wraps over itself and every point of the curve is visited twice in a period. Any point visited at t in the period interval will be visited again at $t' = \frac{1}{2}\frac{1}{f_1 \wedge f_2} - t$ if $t \in \left[0, \frac{1}{2}\frac{f_1}{f_1 \wedge f_2}\right]$, or $t' = \frac{3}{2}\frac{1}{f_1 \wedge f_2} - t$ if $t \in \left]\frac{1}{2}\frac{f_1}{f_1 \wedge f_2}, \frac{f_1}{f_1 \wedge f_2}\right[$.

This last point is highly valuable for implementing an addressing scheme : it shows that with a simple condition over f_1, if there is zero initial phase between the vertical and horizontal displacements – as we initially assumed – the effective frequency of the curve cycle is double the Lissajous frequency. This means that the "actual" crossing points, that is to say the solutions from cases 2 and 3, are visited 4 times during one Lissajous period, with an average addressing frequency of four times the Lissajous frequency. The example previously shown on Fig. B.1 satisfies the frequency condition ($f_1 \wedge f_2 = 6$ kHz and $f_1 = 336 = 56 \times 6$ kHz), so the average addressing frequency of each crossing point is in fact 24 kHz. The term "average frequency" is appropriate here as the crossing points are not necessarily visited in the same order through a Lissajous cycle ; the time interval between two visits of a given point changes in a deterministic way during the cycle. It is worth noting that given the frequency stability of the actuation systems used, the zero-phase condition can easily be implemented by calibrating the actuation sources once when starting operation.

Appendix C

Zernike decomposition for surface profile and mode shape characterisation

While the optical profiler software provided basic analysis tools, such as plane tilt correction and curvature analysis for a linear cut of a 1D profile, a more thorough analysis was necessary to properly classify the observed resonant modes.

A commonly used method for characterising optical surfaces, and in particular quantify aberrations, is Zernike polynomial decomposition [222, 223]. Zernike polynomials are a set of elementary functions over a unit disk, whose expressions correspond to commonly encountered optical aberration. Fig. C.1 shows the first polynomials of the series.

It can be shown [225] that a smooth function over a surface can be decomposed into a linear combination of Zernike polynomials. This decomposition is called the Zernike transform, by analogy with the Fourier transform, and provides useful information on the function's characteristics, by examining the contribution of each polynomial. Similarly to the discrete Fourier transform, a discrete Zernike transform can be implemented [226] as an equivalent for 2D arrays, which in our case represent a discretized continuous surface profile.

The following quickly examines the mathematical bases of Zernike decomposition

Appendix C. Zernike decomposition for surface profile and mode shape characterisation

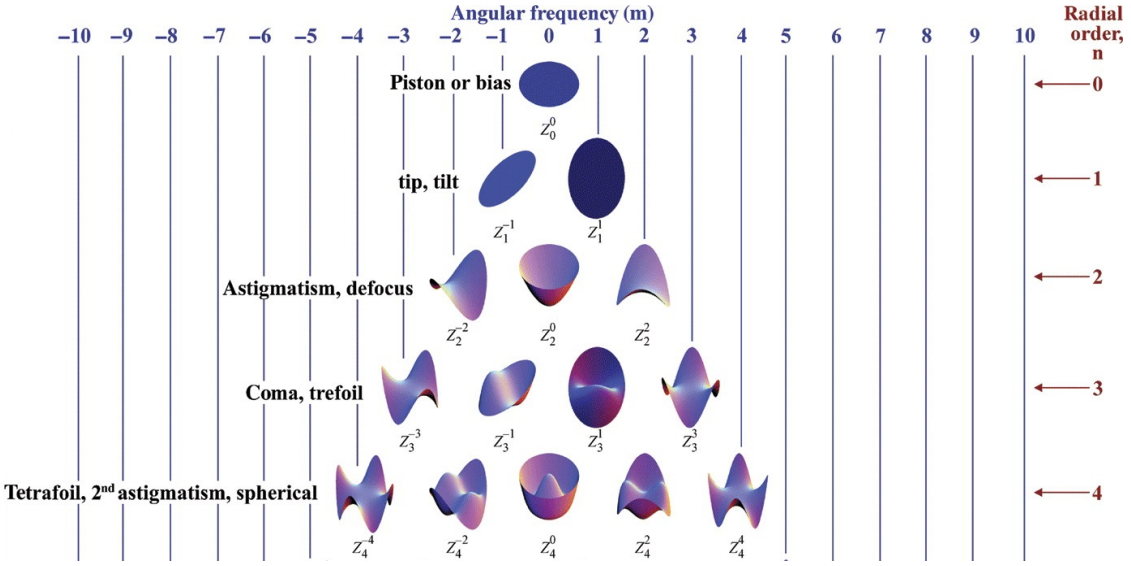

Figure C.1: Illustration of the first five radial orders of the Zernike polynomials. Adapted from [224] with permission.

and describes its algorithmic implementation for processing interferometry data. A more complete demonstration of Zernike polynomials and decomposition can be found in [225].

Zernike polynomials are formally defined as the set of polynomials

$$Z_n^m(\rho,\theta) = R_n^m(\rho)\cos(m\theta) \tag{C.1}$$

$$Z_n^{-m}(\rho,\theta) = R_n^m(\rho)\sin(m\theta) \tag{C.2}$$

for $m, n \in \mathbb{N}$, $m \leq n$, with the radial polynomials

$$R_n^m(\rho) = \sum_{k=0}^{\frac{n-m}{2}} (-1)^k \binom{n-k}{k} \binom{n-2k}{\frac{n-m}{2}-k} \rho^{n-2k} \tag{C.3}$$

for $n-m$ even and 0 for $n-m$ odd (so m must be even if n is even, and odd if n is odd). These polynomials are defined over the unit circle in polar coordinates, for radius $\rho \in [0,1]$.

The Zernike polynomials satisfy a number of properties, in particular :

- they are normalized to $[-1,1]$, i.e. $|Z_n^m(\rho,\theta)| \leq 1$;

- they are orthogonal with each other $\int_0^{2\pi}\int_0^1 Z_n^m Z_{n'}^{m'}\rho d\rho d\theta = 0$ for $(n,m) \neq (n',m')$

with these properties, it can be shown that the Zernike polynomials form an orthonormal basis of the space of real and continuous functions on the unit circle, further justifying the analogy with Fourier decomposition.

When considering discrete Zernike decomposition, however, it must be noted that discretized (i.e. sampled) Zernike polynomials do *not* form a basis of a unit disk with identical sampling ; the existence of a decompositon for discrete functions is thus not guaranteed. However, an approximate decomposition can be achieved by using a number of Zernike coefficients smaller than the number of samples [226]. Consider the linear system

$$s = \mathbf{Z}c \tag{C.4}$$

where s and c are the vectors of samples and coefficients respectively, and $\mathbf{Z}$ is the matrix whose columns are the sampled Zernike polynomials. If $\mathbf{Z}$ has more rows than columns, this system has a solution, or at least an approximated solution (in the least-square sense) through the Moore-Penrose pseudoinverse. Consequently, we can always construct an approximation of the discrete Zernike transform for a low enough coefficient number, with minimized error. Furthermore, it is a reasonable assumption that the approximation of the discrete Zernike transform is also a valid approximation of the continuous transform of the physical surface studied. The basis for this assumption was not examined in detail within the framework of this research, but the performance of Zernike decomposition for surface reconstruction has been studied previously [227] and was found to be comparable to that of other reconstruction methods, with the advantage that it allows characterisation of the surface in terms of optical aberrations. We use the common aberration nomenclature associated with the Zernike polynomials (as found, for example, in [224]) to describe the studied profiles ; it is shown in table C.1.

Algorithmic implementation Automated profile data processing was implemented using MATLAB. In addition to Zernike decomposition, some additional pre-processing

Zernike polynomial index	Aberration
0	Piston
1, 2	Tilt
3, 5	Astigmatism
4	Defocus
6, 9	Trefoil
7, 8	Coma
10, 14	Tetrafoil
11, 13	Secondary astigmatism
12	Spherical

Table C.1: Nomenclature used for Zernike terms, with the Zernike polynomials ordered using the standard OSA indices [228].

was necessary to format the WYKO Vision profile data into an adequate data array. The complete processing sequence was the following :

- use the matlab function `readopd` provided with the Vision software to read the profile data into a 2D array, with the array containing the point height values for the profile ;
- crop the data, keeping only the central part representing the mirror plate and eliminating the surrounding structure. This was done by fitting a maximum radius disk within the valid points of the data, starting from the center of the profile (since the mirror was placed in the center of the field of view during data acquisition) ;
- perform Zernike decomposition using the `zernfun` function as shown in [229]. Decomposition was usually performed up to polynomials of degree 7 (38 coefficients). The coefficient calculation uses matlab `mldivide` operation (the '\' operator) to produce a least-square approximation of the solution to the linear system. This operator uses QR decomposition [230] to obtain the approximation ;
- reconstruct the profile using the coefficients for comparison with the original data, and in particular calculation of residuals.

In general, the reconstructed profiles were found to filter most of the data noise, as well as surface roughness. Fig. C.2 shows an example of such profiles, and Fig. C.3 the corresponding coefficients. Indeed, the use of low-degree polynomials, which have

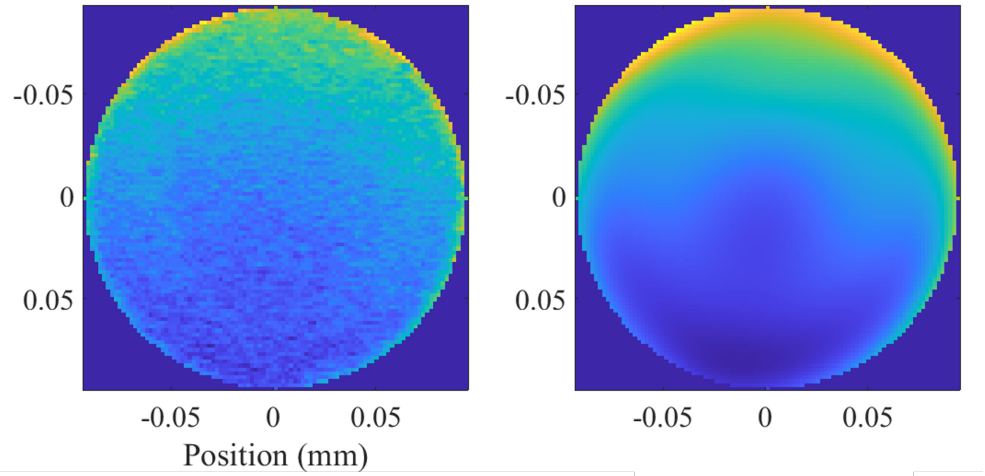

Figure C.2: Left : interferometry profile of a 200 µm diameter mirror plate. Right : reconstructed profile from the Zernike decomposition calculated up to the 7th radial degree (36 Zernike polynomials).

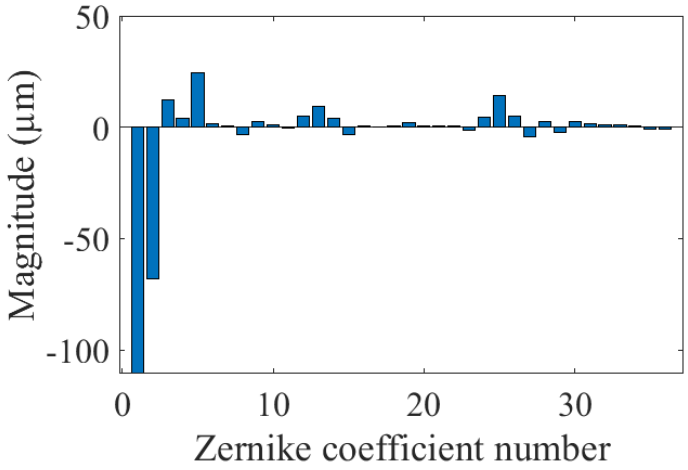

Figure C.3: Coefficients of the Zernike decomposition of the profile shown on Fig. C.2, with the first coefficient corresponding to the degree zero Zernike polynomial. Note the magnitude of coefficients 1 (piston), 2 (horizontal tilt) and 5 (defocus).

low spatial frequency components, is roughly equivalent to applying a low-pass filter to the profile data. This can be considered a drawback of the decomposition process, as roughness can be an important metric to evaluate surface quality. It can however be evaluated by other approaches – e.g. statistical and spatial Fourier analysis.